NASA Conference Publication 2429

Spacelab 3 Mission Science Review

(NASA-CP-2429) SPACELAB 3 MISSION SCIENCE N87-22103
REVIEW (NASA) 98 p Avail: NTIS HC --THRU--
A05/MF A01 CSCL 22A N87-22113
Unclas
G3/34 0065591

Proceedings of a symposium held at
NASA George C. Marshall Space Flight Center
Marshall Space Flight Center, Alabama
December 4, 1985

NASA

NASA Conference Publication 2429

Spacelab 3 Mission Science Review

Edited by
George H. Fichtl
George C. Marshall Space Flight Center
Marshall Space Flight Center, Alabama

John S. Theon
National Aeronautics and Space Administration
Washington, D.C.

Charles K. Hill and Otha H. Vaughan
George C. Marshall Space Flight Center
Marshall Space Flight Center, Alabama

Proceedings of a symposium held at
NASA George C. Marshall Space Flight Center
Marshall Space Flight Center, Alabama
December 4, 1985

NASA
National Aeronautics
and Space Administration

Scientific and Technical
Information Branch

1987

TABLE OF CONTENTS

Page

1. Spacelab 3: Research in Microgravity. 1
2. Spacelab 3 Vapor Crystal Growth Experiment 12
3. Growth of Triglycine Sulfate (TGS) Crystals Aboard Spacelab-3 18
4. Dynamics of Rotating and Oscillating Drops. 27
5. A Laboratory Model of Planetary and Stellar Convection. 31
6. High Resolution Infrared Spectroscopy from Space: A Preliminary Report on the Results of the Atmospheric Trace Molecule Spectroscopy (ATMOS) Experiment on Spacelab 3. 42
7. Auroral Images from Spacelab III 63
8. Ions (Anuradha): Ionization States of Low Energy Cosmic Rays 64
9. Ames Research Center Research Animal Holding Facilities on SL-3. 75
10. Autogenic-Feedback Training: A Preventive Method for Space Adaptation Syndrome 84
11. LS-3 Urine Monitoring Investigation 91

PRECEDING PAGE BLANK NOT FILMED

N87-22104

SPACELAB 3: RESEARCH IN MICROGRAVITY

G. H. Fichtl, J. W. Cremin, C. K. Hill, and O. H. Vaughan
NASA Marshall Space Flight Center
Marshall Space Flight Center, Alabama 35812

J. S. Theon and R. Schmitz
NASA Headquarters
Washington, D.C. 20546

ABSTRACT

The Spacelab 3 mission, which focused on research in microgravity, took place during the period April 29 through May 6, 1985. Spacelab 3 was the second flight of the National Aeronautics and Space Administration's modular Shuttle-borne research facility. An overview of the mission is presented here. Preliminary scientific results from the mission were presented by investigators at a symposium held at Marshall Space Flight Center on December 4, 1985. This special issue is based on reports presented at that symposium.

INTRODUCTION

Spacelab 3, the second flight of the National Aeronautics and Space Administration's (NASA) orbital laboratory, signified a new era of research in space. The primary objective of the mission was to conduct applications, science, and technology experiments requiring the low-gravity environment of Earth orbit and stable vehicle attitude over an extended period (e.g., 6 days) with emphasis on materials processing. The mission was launched on April 29, 1985, aboard the Space Shuttle Challenger which landed a week later on May 6. The multidisciplinary payload included 15 investigations in five scientific fields: materials science, fluid dynamics, life sciences, astrophysics, and atmospheric science.

The basic Spacelab hardware for the mission included a pressurized long module and an Experiment Support Structure (ESS). The pressurized module provided a shirtsleeve environment where the payload crew conducted the experiments. The ESS provided a structure for mounting experiments which required direct exposure to space. Reference 1 provides additional details on the Spacelab 3 mission configuration. The first Spacelab mission in late 1983 verified that the facility provided a suitable environment for research activities in a variety of fields. With this assurance, the Spacelab 3 mission was dedicated solely to scientific experiments, with no further verification testing. (Spacelab 3 was actually the second flight of the laboratory because of delays in the development of a pointing system for the Spacelab 2 mission.)

The NASA Office of Space Science and Applications (OSSA) has overall responsibility for all NASA Spacelab and attached payload missions. The Spacelab 3 mission development and operation was managed and performed for OSSA by the NASA Marshall Space Flight Center (MSFC). Spacelab 3 investigations were selected by a peer review process and were judged on the basis of their intrinsic scientific merit and suitability for flight. Proposals for experiments came through several channels, including NASA Announcements of Opportunity that solicited research ideas from the worldwide scientific communities and agreements with foreign governments. NASA selected 15 investigations for flight, including 12 investigations from the United States, two from France, and one from India. Table 1 provides a list of the experiments and investigators by scientific discipline along with each investigations' acronym which will be used to refer to the instrument throughout this report.

Soon after selection, experimenters convened in an Investigators Working Group (IWG) that met periodically to guide the scientific planning for the mission. The IWG included the principal investigator for each experiment chosen for flight and was chaired by the mission scientist, Dr. G. Fichtl, from MSFC. The IWG was responsible for allocating resources to different experiments, organizing inflight science operations, and nominating and selecting payload specialists. Over the years, the IWG served as a valiable forum for resolving conflicting scientific interests.

The Spacelab 3 mission was designed and operated to provide the best low-gravity environment that could be achieved within the capabilities of Space Shuttle and Spacelab systems. The high quality microgravity environment was conducive to materials processing and fluid dynamics research and at the same time maximized the scientific return for the total payload. Five experiments – three in crystal growth and two in fluid mechanics – were extremely sensitive to gravity, vehicle accelerations, and maneuvers. Mission management gave careful consideration to the elements influencing the Spacelab environment. Maneuvers for an astronomical experiment were scheduled during the first 18 hours of the mission. For the remainder of the mission, the orbiter was maintained in a "gravity gradient" attitude with the tail pointed toward Earth, the wings oriented in the orbit plane, and the payload bay open to the Southern Hemisphere. Maintenance of this stable attitude required the least number of vernier control system thruster firings and, thus, reduced disturbance of the delicate experiments. The attitude was also suitable for the atmospheric and cosmic ray astronomical observations made by three other Spacelab 3 instruments. The particular flight attitude was also selected for a subtle reason which will be referenced later in a discussion of the fluid dynamics experiments. The materials science and fluid physics experiments were clustered around the center of mass of the vehicle, a location least affected by forces proportional to the distance from the center of mass.

The Spacelab 3 mission operations were managed by a MSFC ground control team working in the Payload Operations Control Center (POCC) at the Johnson Space Center (JSC). Science teams for each of the experiments worked in user rooms adjacent to the POCC and interacted with the payload science crew through the POCC communications system. Spacelab 3 demonstrated the value of direct communication between the science crew in space and the research teams on the ground. The mission set a record for downlinked video with over 3 million recorded images. The mission clearly demonstrated that Spacelab represents the merger of science and manned spaceflight. Scientists in space collaborated with their colleagues on the ground, solving problems and modifying experiments to enhance scientific yield.

Payload specialists (PS's) conducted the onboard scientific investigations. They were selected and trained by the Spacelab 3 principal investigators (PI's) and instrument facility developers. The flight payload specialists were Dr. Taylor Wang of the Jet Propulsion Laboratory in Pasadena, California, and Dr. Lodewijk van den Berg of the EG&G Corporation in Santa Barbara, California. The alternate PS's were Dr. Eugene Trinh of the Jet Propulsion Laboratory and Dr. Mary Helen Johnston of the Marshall Center. The alternate PS's supported the mission operations in the POCC. Dr. Wang was the principal investigator for the Drop Dynamics Module experiment (see below), and Dr. Trinh was a co-investigator for that experiment. Dr. van den Berg was a co-investigator for the Vapor Crystal Growth System experiment (see below).

These four scientists were selected for their specialized backgrounds and experience in materials sciences and fluid mechanics. Drs. van den Berg and Johnston are materials scientists with expertise in crystal growth, and Drs. Wang and Trinh are fluid dynamics experts. The flight payload crew consisted of the PS's and the mission specialists (MS's). The designated MS's included Drs. Don Lind, William Thornton, and Norman Thaggard. The flight crew was charged with operation of the Shuttle and was staffed by commander Col. Robert Overmyer and pilot Lt. Col. Frederick Gregory. The MS's were responsible for conducting the interface operations between the Spacelab payload and the Shuttle orbiter and for operating selected science instruments. Mission specialist Lind was a co-investigator on the auroral observations experiment (see below).

Development of an around-the-clock schedule of events for the flight was a major task. Time is a critical resource on a week-long mission. All crew activities, experiment requirements, Spacelab resources, and Shuttle maneuvers were merged into an efficient daily 24-hour operating plan. The master schedule was designed to be revised in response to unexpected difficulties or opportunities, but the guiding philosophy was to adhere as closely as possible to the preflight timeline. As the mission neared, segments of the timeline were rehearsed using the integrated Spacelab hardware and simulators. These simulations prepared the crew, the scientists, and the management cadre for the mission.

The evolutionary nature of the approaching mission was illustrated as the payload was integrated from pieces into a complete scientific research laboratory. Individual instruments arrived at the Kennedy Space Center and were tested. Then they were placed in racks, floor-to-ceiling enclosures which fit inside the cylindrical Spacelab module. Five of the instruments were "minilabs," large instrument facilities that fill an entire rack and can remain assembled for easy reflight. Next, all 12 Spacelab racks installed in the floor were inserted into a habitable module which previously served as a shirtsleeve workshop for the first Spacelab mission. Two instruments were mounted outside the module on the multipurpose Experiment Support Structure (ESS), a lightweight payload carrier that bridged the width of the payload bay. Integrated payload tests were conducted on the ground in which instruments were operated by the crew and investigators. Kennedy Space Center technicians integrated the Spacelab 3 payload with Challenger, and the orbiter was moved to the launch pad.

MATERIALS SCIENCES EXPERIMENTS

The Spacelab 3 mission materials processing experiments were aimed at growing more homogeneous crystals by crystal seed growth research involving vapor transport (VCGS, MICG) and solution growth processes (FES) (see Table 1 for definition of acronyms). The motivation for performing these experiments on the Spacelab 3 mission was to reduce gravity-driven convection and eliminate or reduce imperfections resulting from gravitationally-induced strain fields and dislocations (VCGS) produced by the weight of the crystal when it is relatively weak during the growth process.

Solution Growth of Crystal in Zero Gravity (FES)

Two triglycine sulfate (TGS) crystals were grown by a low-temperature solution growth technique for growth times of 58 and 32.2 hours. The objectives were to (1) develop a technique (cooled sting) for solution crystal growth in a low-gravity environment, (2) characterize the growth environment provided by an orbiting spacecraft and assess the influence of the environment on the growth behavior, and (3) determine how growth in a low-gravity environment influences the properties of the resulting TGS crystal. For the first time in any spaceflight experiment, the growth was monitored onboard as well as on the ground by a specially developed video schlieren technique. Hundreds of holographic photographs were taken during the mission; image projection of the hologram has allowed investigators to observe solution/crystal interaction during the growth process. Preliminary results indicate that the optical system worked very well and the quality of the reconstructed holograms is satisfactory. The hardware performed as expected. The total growth for both crystals was less than predicted from theoretical calculations, but the quality of crystals appears to be quite good. Electrical measurements and fabrication of infrared detectors is in progress. Barnes Engineering Company in Stamford, Connecticut, is working as a guest industrial invesitgator by fabricating the infrared detectors from the flight crystals. TGS has practical applications as a pyroelectric infrared detector. The crystals are the basis of advanced sensor systems for applications which include Earth resources surveying, pollution monitoring, thermal imaging for medical diagnostics, fire location detection, and infrared astronomy. Improved crystals (i.e., crystals with few imperfections) potentially resulting from spaceflight could result in improved detector capability.

Mercuric Iodide (HgI_2) Growth for Nuclear Detectors (VCGS)

The purpose of this investigation was to grow more perfect mercuric iodide crystals in a low-gravity environment by taking advantage of diffusion-controlled growth conditions and by avoiding the problem of strain dislocations produced by the crystal's weight. A single crystal was grown in this facility for approximately 120 hours. This experiment required extensive crew participation. The payload and mission specialists initiated the crystal growth process, monitored the growth phase through a microscope, and responded to crystal growth behavior by making changes in the hardware parameter settings.

After returning to Earth, the crystal grown in space was subjected to gamma-ray rocking curve diffraction measurements. The results obtained to date indicate that the space-grown crystal is of higher quality and more homogeneous than any mercuric iodide crystal grown thus far on the ground. Additional experiments will be made to determine the electronic properties of the space crystal and to evaluate the effect of reduced gravity on the vapor transport process. This crystal substance has considerable practical importance as a sensitive gamma-ray detector and energy spectrometer that can operate at room temperature. Presently, cumbersome cryogenic systems are used to cool available detectors to near liquid nitrogen temperatures. However, the performance of mercuric iodide crystals only rarely approaches the expected performance, presumably because some of the free electrical charges produced within the crystal are not collected at the electrodes but instead remain trapped or immobilized as crystal defects. An efficient high atomic number semiconductor detector that is capable of operating at room temperature utilizing single mercuric iodide crystals offers potential beyond existing detector technology.

Mercuric Iodide Crystal Growth (MICG)

The objective of this experiment was to study crystal seed and growth processes with the vapor crystal growth technique in two and three zone furnaces. The crystal material, mercuric iodide, is the same as that grown in the VCGS, and once again vapor growth process was used. In this experiment, the focus is on the location and number of nucleation sites as a function of temperature distribution and partial pressure of an inert host gas (argon). Six ampoules, approximately 20 cm long and 1.5 cm in diameter, were flown on Spacelab 3. A distribution in temperature is maintained between the ends of the ampoule with and without material sinks at the cold end. A Stefen flow of mercuric iodide occurs from the hot to the cold ends of the ampoule. Nucleation occurs on the walls in the cold zone (1/3 of ampoule). The number and location of these sites, as well as the crystal seeds, are the quantities of interest. The effect of argon gas is to increase the number of nucleation sites and reduce the growth rate. Two experiments were performed, each in sets of three ampoules. The facility was operated over the entire mission. This experiment builds upon knowledge gained from similar experiments performed with the same facility on the Spacelab 1 mission wherein the goal was to grow single large crystals. This furnace was automated and required with minimal crew interaction.

FLUID DYNAMICS EXPERIMENTS

The Spacelab 3 fluid dynamics experiments are aimed at the study of fundamental fluid dynamic processes associated with rotating and oscillating drops and convection in spherical geometry.

Geophysical Fluid Flow Cell Experiment (GFFC)

The primary objectives of the geophysical fluid flow experiments are to simulate large-scale baroclinic (density-stratified) flows which occur naturally in the atmospheres of rotating planets and stars and to gain insights concerning the large-scale nonlinear mechanics of global-scale geophysical flows in spherical geometry. In particular, the investigators hope to identify those external conditions related to fluid viscosity, rotation, gravity, etc., which allow qualitatively different modes of instability or waves in the model.

The experiments were accomplished with a rotating hemispherical shell of fluid wherein radial gravitational forces are simulated with electrical polarization forces created in a dielectric fluid by applying a radially directed voltage drop across the fluid. The GFFC provides a simulated gravitational field of approximately 0.1 g or less. Spaceflight is required to insure the spherical symmetry of the total "gravitational field" in the experiment; in a terrestrial laboratory, gravity will destroy the spherical symmetry of the "gravitational field" in the GFFC. Total experiment time was 103 hours. The observations of temperature fluctuations in the fluid indicate that strongly rotating bodies exhibit global-scale convective patterns that tend to align themselves in "Taylor columns" oriented parallel to the rotation axis. However, as the degree of thermal instability is increased, strong buoyancy-driven turbulence sets in at high latitudes. At very large heating rates (or high Rayleigh numbers), this polar convection spreads toward the equator and eradicates the Taylor columns. When the imposed radially unstable temperature gradient includes a latitudinal component, new spiral instabilities are observed. At high heating and high rotation, the Taylor columns reappear but interact strongly with mid-latitude motions. The experiments are in agreement with linear theory and numerical simulations that can be carried out at the least extreme thermal conditions (lower Rayleigh numbers) of the laboratory model [4].

It is interesting to note that a vehicle attitude in which the angular velocity vectors of the vehicle and the experiment convection cell are parallel is preferred to minimize precessionally-driven fluid motions from occurring in GFFC. The Spacelab 3 vehicle attitude satisfied this requirement.

Dynamics of Rotating and Oscillating Free Drops (DDM)

The experiments performed in the DDM provided the first experimental data on free rotating and oscillating drops. The DDM is a three-axis acoustic facility wherein liquid drops can be formed and excited to execute rotational and oscillatory motion. Spaceflight is required because very strong acoustic forces would be required in terrestrial-based experiments which in turn would introduce physical phenomena that would overwhelm the physics under investigation.

The DDM research conducted on Spacelab 3 has yielded the first concrete experimental evidence on the manipulation of liquid drops using acoustic radiation pressure forces in microgravity. Drops of water and water and glycerin mixtures were successfully deployed and captured by the acoustic potential well without introducing any significant static distortion on the samples. Rotation around a fixed axis of the drops was also induced through acoustic torque and has allowed a study of the equilibrium drop shape dependence on the rotation rate. Results of some shape oscillation sequences have also confirmed the feasibility of surface tension and viscosity measurement schemes.

The axisymmetric regime of a freely suspended rotating drop has been studied in detail using volumes ranging from 0.5 to 10 cc, with viscosities between 1 and 100 cSt, liquid density around 1.16 g/cc, and surface tension centered at 65 dynes/cm. Very repeatable results have been obtained for the spin-up rate, the critical rotation speed for bifurcation between axisymmetric and two-lobed shapes, the axial deformation dependence on the rotation rate, and finally for the critical velocity at fission. No experimental evidence for any transition to higher multi-lobed shapes have been obtained in this first set of experiments.

The experiments are of fundamental interest because they are the first controlled experiments to be performed on essentially free drops and thus provide the first experimental data for testing theoretical predictions. They also provide guidance for development of theoretical models. The experiments are also of practical interest because acoustic manipulation of liquids is a prime candidate for containerless processing applications in space.

LIFE SCIENCES EXPERIMENTS

The Spacelab 3 mission life sciences experiments were aimed at (1) verification of design and biocompatibility assessment of research animal holding facilities, (2) calibration and verification of a urine monitoring system, and (3) test and application of autogenic feedback processes as a countermeasure to space adaptation syndrome.

Ames Research Center Life Science Payload

In response to a recognized need for an in-flight animal housing facility to support Spacelab life sciences investigations, a Research Animal Holding Facility (RAHF) was developed. The Spacelab 3 mission provided an opportunity to perform an in-flight Verification Test (VT) of the RAHF. Lessons learned from the RAHF-VT and baseline performance data will be invaluable in preparation for subsequent dedicated life sciences missions.

The RAHF is designed to support animals ranging in size from rodents to small primates. It is anticipated that such a system will satisfy the experimental requirements of a great majority of prospective investigators working with commonly-used laboratory animals.

On Spacelab 3, one RAHF was dedicated to supporting two monkeys in separate cages while the other supported 24 rats. The primate RAHF has the capability to house four monkeys; however, because of a decision to fly monkeys free of herpes virus Samuri only two monkeys were flown on this checkout mission. Over the 7-day flight, food and water were dispensed automatically. A photocell method was used to record animal activity. Four of the rats were monitored by a biotelemetry system (BTS) which recorded deep body temperature, heart rate, and waveform. Four rats were intermittently photographed during the mission by a movie camera programmed at given frame rates; the film was used to assess behavioral response to launch/recovery conditions and to weightlessness. The environment was automatically monitored and controlled for factors such as temperature, humidity, and airflow. During ascent and entry a dynamic environment measuring system (DEMS) was used to measure noise, vibration, and acceleration forces in the vicinity of the RAHF.

The RAHF worked very well, with some exceptions involving particulate release. The rats and monkeys were recovered unstressed, in excellent condition, and microbiologically clean. This information allows us to state that the RAHF maintains animals in a manner analogous to vivarium animals in laboratories and permits support of animal research in space in a realistic manner.

While the data is only partially reduced at this point, much information has already been obtained on the animals. One monkey demonstrated symptoms of space adaptation syndrome while the other did not. The rats returned to Earth with the following changes: they were flaccid, showing a marked decrease of muscle tone; marked loss of muscle and fiber diameter; reduced activity of the Krebs cycle in the muscle; hemorrhaging in one muscle; marked decrease in bone mass and a decrease in elasticity and breaking strength; a decrease in prolactin producing cells and an increase in growth hormone producing cells (however, little growth hormone was released postflight); and an increase in the hematopoietic system sensitivity in epythropoietin. As data analyses are completed, it is expected that this mission will yield the greatest amount of information ever obtained from a biological payload in space and may well be the most significant contribution on biological systems in space ever gained from a single mission.

Urine Monitoring Investigation (UMS)

This investigation was designed to evaluate the UMS and to monitor the urine biochemistry of the crew. The primary objectives of the Urine Monitoring Investigation were (1) to verify the operation of the Urine Monitoring System (UMS) in the collection and sampling of urine, (2) to perform in-flight calibration of the UMS, (3) to estimate the crew members' ratio of fluid intake to urine output, and (4) to measure the effects of microgravity on a number of biochemical constituents of urine. Subsequent dedicated life sciences missions are anticipated to incorporate the UMS in support of a number of experiments which will be directed at studying fluid/electrolyte disturbances and related effects resulting from low-gravity exposure. Because of insufficient air flow through the UMS, only a few urine samples were collected for postflight analysis, and the limited number of samples precluded the physiological study of the sample. The calibration and testing objectives of the investigation were completed.

Autogenic Feedback Training

The objective of this experiment was to test the effectiveness of the combined use of autogenic and biofeedback training as a countermeasure to space adaptation syndrome (SAS) and to gain basic physiological data associated with SAS. Autogenic feedback training is a procedure that enables human subjects to gain voluntary control of several physiological responses simultaneously. Autogenic and biofeedback training, when used separately, do not appear to be effective countermeasures to motion sickness. However, it appears that a combination of these two techniques for control of bodily responses yields a powerful countermeasure to SAS which can be learned in a relatively short period of time. The principal investigator at the NASA Ames Research Center has obtained excellent results in ground-based rotating chair experiments for subjects with a wide-range of susceptibility to motion sickness. The Spacelab 3 mission AFT experiments involved the flight payload specialists as subjects and two of the mission specialists as controls. The subjects were given exercises to practice in the event of discomfort.

During their awake periods, both subjects and controls were instrumented with sensors to measure and record heart rate, body temperature, galvanic skin response, air volume, and breathing rate. These data were presented to the subjects on a wrist readout and used during AFT exercises by the subjects in response to discomfort associated with space adaptation as well as during routinely scheduled exercises to prevent SAS. Analysis of the Spacelab 3 AFT results is now underway.

ATMOSPHERIC OBSERVATIONS

The Spacelab 3 mission environmental observation experiments are aimed at the (1) measurement of atmospheric minor and trace species and (2) observation of southern aurora from a Spacelab orbit vantage point.

Atmospheric Trace Molecule Spectroscopy (ATMOS)

This investigation was designed to obtain fundamental information related to the chemistry and physics of Earth's upper atmosphere using the techniques of infrared absorption spectroscopy. There are two principal objectives. The first is the determination, on a global scale, of the compositional structure of the upper atmosphere and its spatial variability. The establishment of this variability represents the first step toward determining the characteristic residence times for upper atmosphere constituents, the magnitudes of their sources and sinks, and, ultimately, an understanding of their effects on the stability of the stratosphere. The second objective is to provide the necessary high-resolution, calibrated spectral information required for detailed design of advanced instrumentation for global minitoring of specific species.

The experimental approach for acquiring the data from Spacelab was to view the Sun with the ATMOS instrument during the periods just prior to entry into, and shortly after emerging from, a solar occultation. Specifically, the viewing periods were timed to occur when the ATMOS instrument's view of the Sun was occulted by the upper atmosphere. During these periods, the instrument made a set of interferometric measurements of the solar radiation incident as a function of optical path difference within the instrument. Subsequent Fourier transformation of these measurements produced spectra of the solar continuum between 2 and 16 m with a resolution of 0.02 cm^{-1}. The characteristic absorption features are associated with stratospheric layers approximately 2 km thickness.

The instrument operated superbly. A total of 20 occultations were taken encompassing altitudes from approximately 5 to 120 km.

Preliminary analysis of the data has revealed the presence of more than 30 different molecular species whose concentrations can be measured over altitude ranges that vary, depending on the particular constituent, from the upper troposphere through the stratosphere and mesosphere to the lower thermosphere (approximately 130 km). Several of the trace constituents (for example N_2O_5 and $ClONO_2$) have not previously been detected with certainty. The stratospheric spectra provide simultaneous measurements of most of the species of importance in the nitrogen, chlorine, and hydrogen families of molecules involved in the ozone photochemistry of this region; the observations of the mesosphere and thermosphere, which include measurements of CH_4, CO_2, CO, H_2O, and O_3, provide new insights into the photochemistry and dynamics of the region of the atmosphere characterized by dissociation of the minor gases and by the effects of the breakdown of local thermodynamic equilibrium [5].

In addition to the teluric spectra, the Spacelab 3 ATMOS flight returned a sufficient number of high resolution solar spectra to produce a very high signal-to-noise ratio solar atlas of the near and mid-infrared wavelength region. When published, this atlas will show features of the Sun's photosphere and chromosphere that have not been previously observed. NASA plans to fly the ATMOS instrument at approximately yearly intervals for the next 10 to 15 years to provide an archive of the composition of the upper atmosphere and its variability. The data will provide a valuable record to aid in the assessment of long-term changes in the properties of the atmosphere.

Auroral Observations

The Spacelab 3 mission provided a unique opportunity to make detailed observations of Southern Hemisphere aurora from space. Observations of aurora are available from the ground and from space looking downward from satellites (Dynamics Explorer, Defense Meteorological Satellite Program, for example). However, systematic observations of aurora from a lateral vantage point like that provided by the Spacelab 3 mission orbit with 57 deg inclination and sufficiently large angle (angle between the Sun-Earth line and vehicle orbit plane) to penetrate the average auroral oval in darkness were not available previously. The typical aurora altitude is approximately 110 to 160 km and range in vertical extent from approximately 15 to 50 km. Thus, with a 350 km orbit altitude and range to the aurora target from Spacelab of 0 to 800 km, the viewing perspective varies from a downward looking one to a sideward looking one approximately 20 deg above the aurora. The orbiter's video imager was used to acquire five hours of data. The crew also took 274 color photographs. By using the orbital motion to provide the paralax, color photographs and the video recordings have been viewed stereoscopically.

The data provide the first views from outside the atmosphere of thin horizontal layers of "enhanced aurora." The layers, once thought to be rare, were recorded on two out of three passes. This first observation of enhanced aurora from space eliminates concerns that the ground-based observations might have been an optical illusion caused by atmospheric refraction. Also, for the first time, vertically thin layers were observed in diffuse aurora. This is a measurement that is possible only from space, ideally in near-Earth orbit.

ASTROPHYSICAL OBSERVATIONS

The Spacelab 3 mission astrophysics experiments were aimed at the (1) study of ionization states of solar and galactic cosmic ray heavy nuclei and (2) study of galactic and faint extragalactic sources and peculiar ultraviolet objects.

Cosmic Ray Experiment (IONS)

The Indian experiment, IONS (also called ANURADHA by the science team, ANURADHA is the Sanskrit name of the star Delta in Scorpius constellation), designed to measure the ionization states of low-energy galactic cosmic ray heavy nuclei, was highly successful on Spacelab 3. The flight period was characterized by (1) absence of solar flares and by (2) low-level of solar activity close to that of solar minimum. Therefore, the Spacelab 3 Mission was most favorable for the present studies of low-energy galactic cosmic ray heavy nuclei. The Anuradha experiment measures, in near Earth space, the flux, energy spectrum, arrival time, and direction of all heavy ions of all major elements, from helium to iron, of low energy cosmic rays, known as Anomalous Cosmic Rays (ACR) in the energy range of about 5 to 100 MeV/amu. From the arrival direction of heavy ions in space, the threshold magnetic rigidities (i.e., momentum/charge) of ions are determined using the computations of cosmic ray trajectories in geomagnetic field. By combining the data of magnetic rigidities with momentum of ions measured in the main detector, the ionization states of heavy ions are determined. The measurements of the ionization states, together with the abundances and energy spectra, will provide new clues to the origin of the ACR which is unknown at present.

From the initial studies of track density of cosmic ray events, it is calculated that the main detector has recorded high-quality events of about 10,000 particles and similar number of C, N, O and heavier ions of ACR. Analysis of the main detector stack is in progress.

Ultraviolet Astronomy Experiments (VWFC)

The proposed experiment was designed to study (1) large scale distribution of ultraviolet radiation in the Milky Way, (2) geometric extension of stellar clouds and spectral distribution, (3) diffusion of galactic light above the galactic plane (extension of galactic material), (4) sky background relative to discrimination between galactic and extragalactic light and Sun light scattered by interplanetary dust (zodical light), and (5) spectral distribution of extended sources (as noted above) and nebular spectrography. Measurements were to be taken with a Schmidt camera which uses a 4 cm square photocathode proximity (diode) light intensifier to sense the incoming UV (1550-2300 angstroms) radiation. Three interference filters at wavelengths of 1550, 1900, and 2500 angstroms with a slit provided spectrograph capability. The instrument field of view if 54 deg with angular resolution of 3 arc minutes. The instrument was designed to operate out of the scientific air lock after sunset. Six targets were planned for this mission. This instrument flew on the Spacelab 1 mission and acquired data on the lower half of the celestial sphere. The Spacelab 3 mission targets were primarily located in the northern half of the celestial sphere [3].

Because of a malfunction of the Spacelab scientific air lock, it was not possible to carry out this investigation.

SUMMARY

The Spacelab 3 mission, by any measure, was an outstanding success. We have learned how to utilize the Shuttle/Spacelab system to provide the best low-gravity environment achievable from this system. This knowledge is being used in the development of Space Station and low-gravity facilities. The Spacelab 3 mission is a model for designing and operating future low-gravity Spacelab missions. Much of the research begun on Spacelab 3 will continue on future Spacelab missions and will help set the stage for research aboard Space Station.

REFERENCES

1. Hill, C. K., NASA TM-82502, 50 pp., November 1982.

2. G. Courtes, M. Viton, J. P. Sivan, R. Decher, and A. Gary: Science, Vol. 225, 1984, p. 179.

3. S. Biswas, et al., ibid, p. 64.

4. J. E. Hart, et al., ibid, p. 27.

5. C. G. Farmer and O. F. Raper, ibid, p. 42.

TABLE 1. SPACELAB MISSION 3 PAYLOAD

Discipline	Title	Acronym	Principal Investigator	Institution
Materials Science	Fluid Experiment System	FES	Dr. R. Lal	Alabama A&M University
	Vapor Crystal Growth System	VCGS	Mr. W. Schnepple	EG&G, Goleta, California
	Mercury Iodide Crystal Growth (Reimbursable)	MICG	Dr. R. Cadoret	Laboratoire Physique des Milieux Condense's, France
Fluid Dynamics	Drop Dynamics Module	DDM	Dr. T. Wang	Jet Propulsion Laboratory
	Geophysical Fluid Flow Cell	GFFC	Dr. J. Hart	University of Colorado
Life Sciences	Ames Research Center Life Sciences Single Rack		Dr. C. Schatte	NASA Ames Research Center
	- Primate Research Animal Holding Facility (RAHF) Verification Test	RAHF		
	Double Rack			
	- Rodent Research Animal Holding Facility (RAHF) Verification Test	RAHF		
	- Biotelemetry System	BTS		
	- Dynamic Environment Measurement System	DEMS		
	Autogenic Feedback Training Experiment	AFT	Dr. P. Cowings	NASA Ames Research Center
	Urine Monitoring Investigation	UMI	Dr. C. Leach-Huntoon	NASA Johnson Space Center
Atmospheric Science	Atmospheric Trace Molecules Spectroscopy	ATMOS	Dr. C. Farmer	Jet Propulsion Laboratory
	Auroral Observations	Aurora	Dr. T. Hallinan	Geophysical Institute Fairbanks, Alaska
Astrophysics	Ionization States of Solar and Galactic Cosmic Ray Heavy Nuclei	IONS	Dr. S. Biswas	Tata Institute of Fundamental Research, India
	Very Wide Field Camera	VWFC	Dr. G. Courtes	Laboratorie D'Astronomie Spatiale, France

N87-22105

SPACELAB 3 VAPOR CRYSTAL GROWTH EXPERIMENT

W. Schnepple, L. van den Berg, N. Skinner, and C. Ortale
EG&G Energy Measurements, Inc.
Santa Barbara, California 93117

ABSTRACT

The Space Shuttle Challenger, with Spacelab 3 as its payload, was launched into orbit April 29, 1985. The mission, number 51-B, emphasized materials processing in space, although a wide variety of experiments in other disciplines were also carried onboard. This report describes one of the materials processing experiments on this flight, specifically the growth of single crystals of mercuric iodide by physical vapor transport.

DISCUSSION

Mercuric iodide was chosen as the subject material for the space experiment for several reasons. In the form of a single crystal, it has high technological interest as a detector of X- and gamma radiation. Also, because of the relatively low growth temperatures used, the flight furnace could be built to operate with modest electrical power demands on the Spacelab resources. Finally, very few vapor crystal growth experiments have been done, to date, under microgravity conditions.

Single crystals of mercuric iodide can be used to detect nuclear radiation. This ability was first recognized in the early 1970's [1]. Since then, efforts at a number of different laboratories have succeeded in improving the overall quality of these detectors [2].

Two basic properties of the mercuric iodide make it attractive as a radiation detector material: First, the compound has relatively high atomic numbers (80, 53) for its constituents, which results in a large photoelectric cross-section for X- and gamma radiation. Thus, high absorption and good detector efficiency can be achieved in a relatively thin section of the material. The second feature of this semiconductor is its relatively large bandgap (2.1 eV). As a consequence, mercuric iodide detectors can be operated at room temperature, in contrast to the cryogenic temperatures which are required of other semiconductor nuclear radiation detectors.

While a steady and significant improvement in detector device characteristics has occurred over the past 10 years, it still remains that mercuric iodide has not yet achieved its full potential. As is generally true with all devices made from semiconductor single crystals, improved performance comes with advances in three key areas: purification and better control over the quality of the starting material, better understanding and control of the growth of the single crystals, and development of optimal processing techniques to fabricate the devices.

The space experiment focused on crystal growth, although parallel efforts were made in improving the other key areas. Two specific aspects of the crystal growth motivated the interest in growing crystals in microgravity.

First, on Earth in 1 g, convection occurs in the conventional growth furnaces that are used for growing mercuric iodide crystals. Early ground based research indicated that this occurred both outside and inside of the closed ampoule containing the polycrystalline mercuric iodide source material and the growing crystal. The occurrence of convection in crystal growing is not, in all cases, undesirable. There is, however, a risk that convective instabilities will occur, which would lead to growth irregularities, and these are highly undesirable. In our system, irregularities in the vapor transport and/or the temperature fields could occur. Such irregularities are known to produce crystal defects (vacancies, etc.).

A second aspect involved the extremely fragile nature of these crystals. Previous laboratory experience showed that they were very soft and easily damaged in handling, sometimes even "cold flowing," just by their own weight, over wires used for electrical leads. Testing indicated that at room temperature the critically resolved shear stress on well-grown crystals was indeed very low and decreased with increasing temperature. It seemed quite possible that the weight stresses in the crystal at growth temperatures might be sufficient to cause plastic deformation.

Regardless of the cause, flaws in a crystal's structure seem generally to result in degraded electronic properties for all semiconductor crystals. Growth in microgravity should help to alleviate both of these problems, thereby leading to a higher quality crystal. Gravity driven convection would be virtually removed, taking with it the problem of irregularities in the transport rate of the mercuric iodide vapor. Also, the crystal would be under no weight stress during its growth, and could be cooled down and optimally stored before the shuttle made its deorbit and landing.

Although a microgravity experiment was the eventual goal of this program, a large part of the total effort was done on the ground. Starting from apparatus and procedures developed for 1 g vapor crystal growth, studies were made on ways to reduce the power, size, weight and complexity of the crystal growth furnaces. As a result, several modified, "protoflight" furnaces were built and tested.

Attempts were also made to simulate the effect microgravity would have in changing the 1 g temperature fields in these furnaces (the absence of convection was simulated by testing the furnace under reduced pressure, in a bell jar). This testing led to several other furnace modifications that were used to "tailor" the simulated microgravity temperature profile. A schematic of a protoflight furnace is shown in Figure 1. The real flight furnace was very similar physically, and was functionally equivalent, to the protoflight unit.

The ground research phase also provided an opportunity to grow a number of 1 g control crystals and to develop new characterization methods for the crystals. In particular, methods were developed to measure mechanical properties of the crystals (critical resolved shear stress) and to examine the structural perfection, both on the surface and in the bulk of the crystal (X- and gamma ray diffraction "rocking" curves).

The mission timeline was developed to allow the crystal growth experiments to be activated as early as possible in order to maximize growth. For the Vapor Crystal Growth (VCG) experiment, its timeline was divided into three phases: heatup, crystal growth, and cooldown. The durations were approximately 4, 118, and 8 hours, respectively, with the initial turn-on occurring about 10 hours after orbit was achieved.

Two members of the payload crew were responsible for the VCG on alternating 12 hour shifts, with duties that included stowing and unstowing of the crystal growth ampoule, setting up and conducting the experiment, and holding periodic two-way dialogs with the science team at Johnson Space Center. Members of the science team at the JSC Payload Operations Control Center had available to them several data displays, including all of the key furnace temperatures and, at times, a TV image of the growing crystal.

The experiment made use of an ampoule containing a small seed (approximately 3 mm on a side) which had been grown on Earth. During the initial heatup phase, some thermal etching of the seed occurred, as planned, in order to remove any stray particles of mercuric iodide "dust" that might have come onto the seed's surfaces.

After landing at Edwards Air Force Base, the crystal, protected within its growth ampoule, was taken from the Spacelab and transported to the Marshall Space Flight Center, where a series of photographs were made of it. The size of the crystal was approximately 1.2 cm x 1.2 cm x 0.8 cm, and its weight was about 7.2 grams. During the experiment, the linear growth rate of the crystal varied, reaching a maximum of about 3 mm/day. This compares with growth rates on earth that range from about 0.5 to 2 mm/day, with an average of about 1 mm/day. (On Earth it is difficult to achieve a rate of 3 mm/day without the rapid occurrence of undesired spurious nucleation).

The ampoule containing the crystal was next carried to the University of Missouri for gamma ray rocking curve testing. In this testing, a collimated, 1 mm diameter monoenergetic beam of gamma rays impinges on the crystal. Much of the highly penetrating beam simply goes straight on through the sample; however, a fraction is Bragg-diffracted at a small angle and, after passing through and exiting the sample, it is then detected. An advantage to using gamma rays is their ability to penetrate materials. This allowed testing the crystal while it was still enclosed in its glass ampoule. In addition, the measurement of the sample in transmission gave a good indication of its bulk quality.

By orienting the crystal at its appropriate Bragg angle relative to the incident beam, the signal from the diffracted beam will yield information about the crystal's structural quality. For a perfect structure, when the crystal is rotated, or rocked, through the neighborhood of its Bragg angle, the intensity of the diffracted beam will go through a sharp maximum. If defects occur, however, the Bragg diffraction peak can be broadened, or even split into multiple peaks. For example, a crystal containing two subgrains, one slightly misoriented from the other, can produce two separate Bragg diffraction peaks that are slightly displaced in angle, as the crystal is "rocked," or rotated, in the beam.

The gamma ray rocking curve tests showed the space crystal to be of high quality. The results were approximately equal to the very best obtained from samples grown on Earth, and noticeably superior to the average. Figures 2 and 3 show rocking curves for space and Earth crystals. The space crystal, with a single peak, shows the region to be free of these defects. The multiple peaks in Figure 3, which are a usual occurrence for Earth-grown crystals, are an indication that nearby regions of the crystal are slightly misoriented to one another (subgrains).

Rocking curve testing of a similar nature, but using less penetrating X-rays, was performed at the University of California at Los Angeles. Again, the results showed the space material to be of high quality, and with a quality gradient, confirming the gamma ray results. Because of the lower energy, the X-ray beam penetration was only a few micrometers into the sample, in contrast to the gamma ray measurements. Because it was essentially a surface measurement, this test did provide a sensitive means of monitoring damage due to handling and detector processing. Such damage was expected, and found, although attempts were made to minimize it.

Damage did occur to the first slice that was cut from the crystal. About 2 mm thick, the slice was sawed from the crystal, then temporarily mounted with silicone rubber for additional X-ray rocking curve testing. In demounting the slice from the rubber, damage occurred. After fabrication into a detector, the unit was tested for its performance as a gamma ray spectrometer using Americium 241 and Cesium 137 isotope sources. Only average results were obtained.

Another slice was then cut and used for detector fabrication, however the steps of silicone rubber mounting and X-ray rocking curve testing were omitted. In this case, the performance of the detector proved to be much better than that of the first slice. If similar data from a population of several thousand detectors made from Earth-grown crystals is compared with it, only about the top 6 percent of the Earth detectors would perform as well.

REFERENCES

1. W. R. Willig, S. Roth, Proc. Internat. Symposium on CdTe, Siffert & Coche, Eds., Strasbourg (France), June 1971.

2. H. A. Lamonds, Nuclear Instr. & Methods 213, 5-12, 1983.

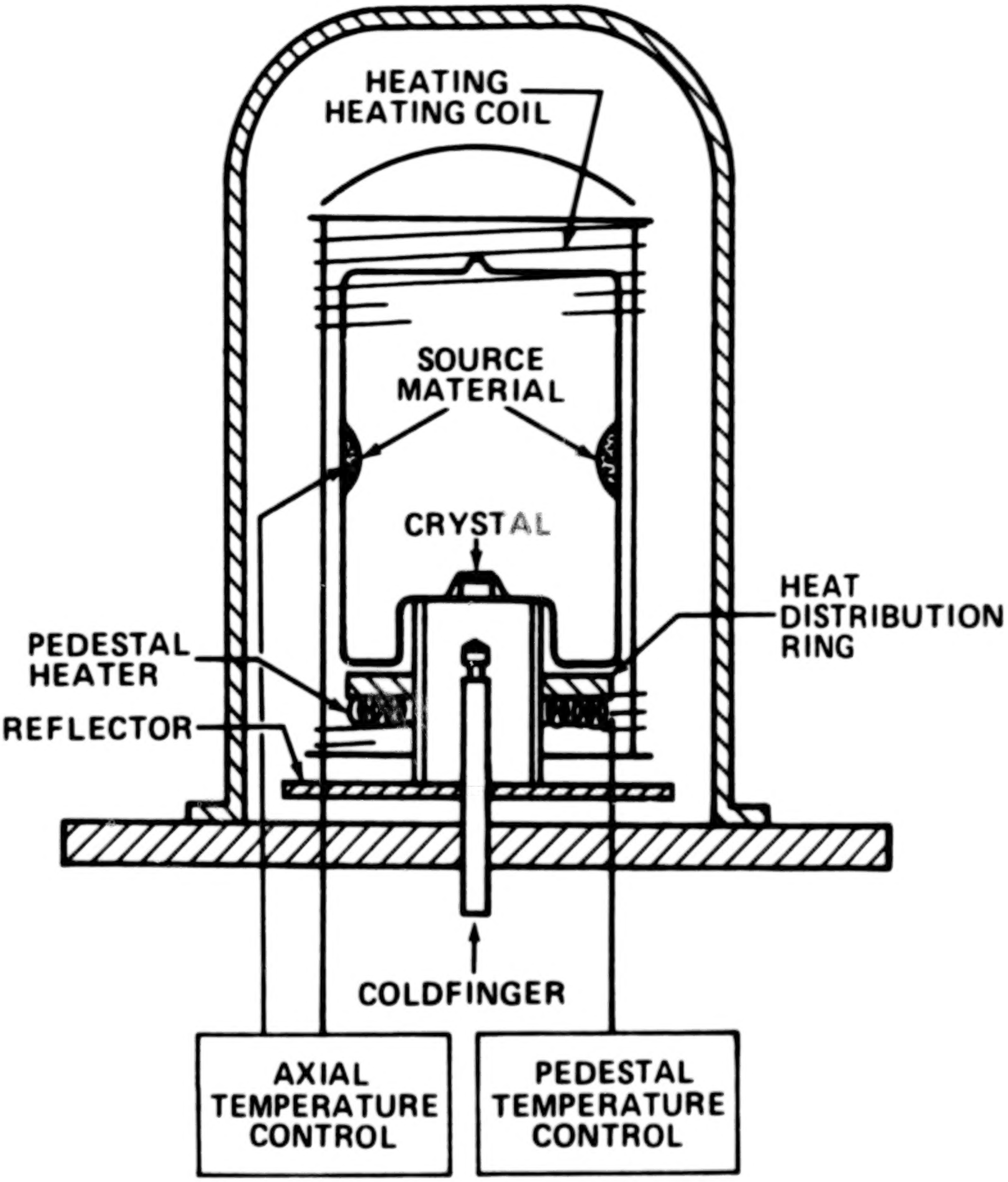
HEATING
HEATING COIL
SOURCE MATERIAL
CRYSTAL
HEAT DISTRIBUTION RING
PEDESTAL HEATER
REFLECTOR
COLDFINGER
AXIAL TEMPERATURE CONTROL
PEDESTAL TEMPERATURE CONTROL

FIG. 1

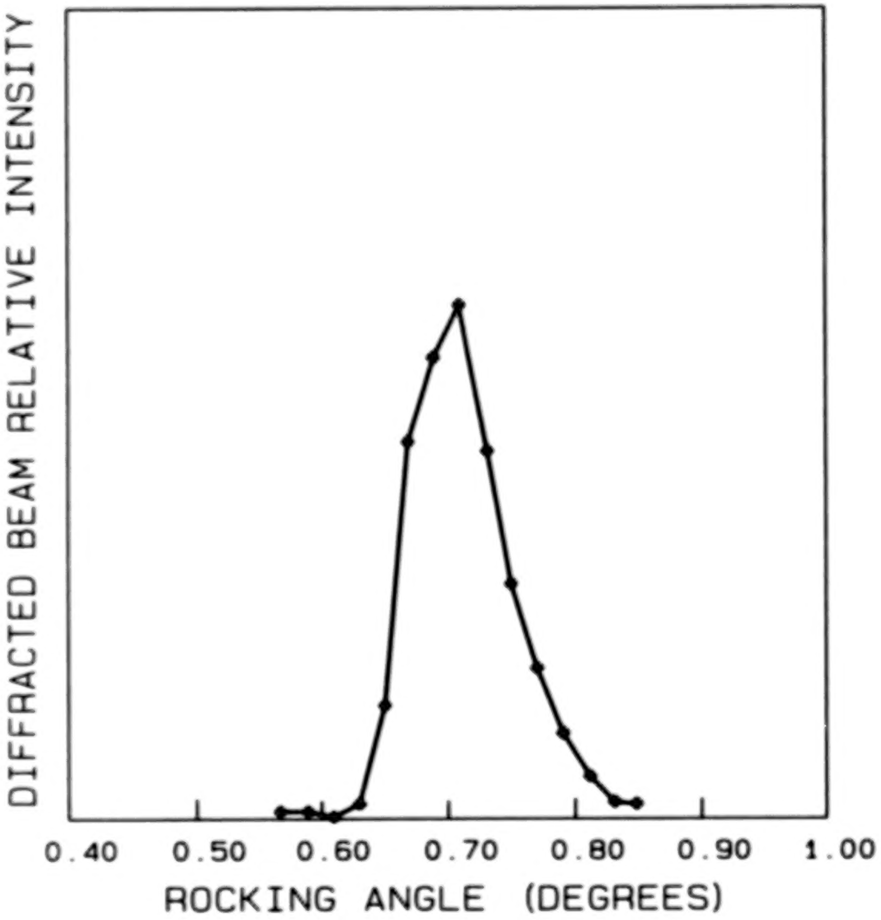

GAMMA DIFFRACTION ROCKING CURVE
FOR THE SL-3 CRYSTAL

FIGURE 2

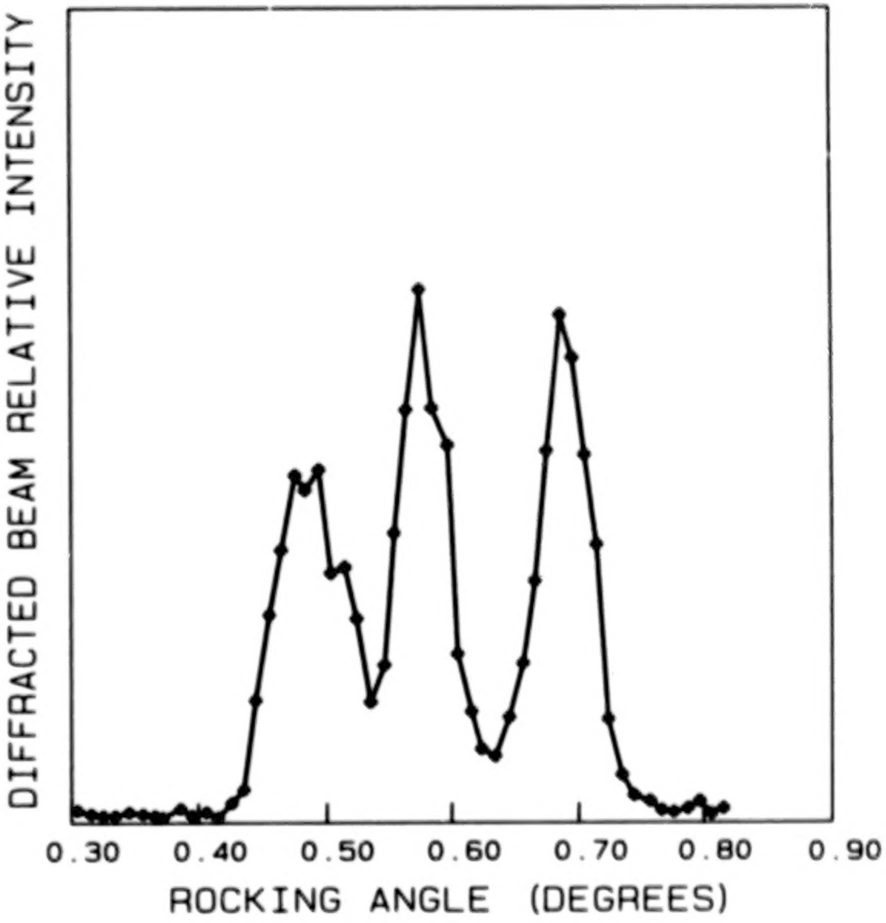

GAMMA DIFFRACTION ROCKING CURVE
FOR AN EARTH GROWN CRYSTAL

FIGURE 3

N87-22106

GROWTH OF TRIGLYCINE SULFATE (TGS) CRYSTALS ABOARD SPACELAB-3

R. B. Lal, M. D. Aggarwal, and A. K. Batra
Department of Physics, Alabama A&M University
Huntsville, AL 35762

R. L. Kroes
Space Science Laboratory
NASA/Marshall Space Flight Center, AL 35812

William R. Wilcox
Clarkson University
Potsdam, New York

James R. Trolinger
Spectron Development Laboratories, Inc.,
Costa Mesa, CA

Philip Cirino
Barnes Engineering Company
Stamford, CT

ABSTRACT

An experiment to study the growth of single crystals of triglycine sulfate $(NH_2CH_2COOH)_3$ H_2SO_4 (TGS) was successfully carried out on the Spacelab-3 mission during April 29-May 6, 1985. Two crystals of TGS were grown during the flight, using a specially developed cooled sting technique [1] of solution crystal growth. For the first time in any flight experiment the growth was monitored on-board as well as on ground by video-schlieren technique. Hundreds of holograms were taken for the solution/crystal interaction during the growth process. Preliminary results indicate that the optical system worked very well and the quality of reconstructed holograms is satisfactory. The cooled sting technique was successfully demonstrated. Holographic interferograms indicate convection free, diffusion limited growth. Some of the preliminary results of crystal quality are also presented.

DISCUSSION

An experiment to study the growth of single crystals of TGS was carried out on the Shuttle mission 51-B of Spacelab-3 during April 29-May 6, 1985. The objectives of the experiment were: (a) to develop a technique for solution crystal growth in a low-g environment, (b) to characterize the growth environment and determine its influence on the growth behavior, and (c) to determine how the low-g environment influences the properties of the resulting TGS crystals.

TGS crystals were selected as a candidate growth material because they can be grown at comparatively low temperature (30°C-45°C); TGS solution is a transparent system so that holographic techniques could be employed to study fluid properties in order to characterize the growth environment; TGS has high technological importance for infrared detectors (8 to 14 μ) operating at room temperature; present devices have detectivities about an order of magnitude below the theoretically predicted values.

These crystals were grown utilizing a specially designed Fluid Experiment System (FES), which is a general purpose facility, built by TRW, Redondo Beach, California, for studying the behavior of fluids in space [2]. The FES uses holography as its main data gathering system [3]. The experiment was performed during the mission by Dr. Lodewijk Van den Berg (Payload Specialist) and Dr. Don L. Lind (Mission Specialist).

Figure 1 shows a detailed diagram of the crystal growth flight cell. The temperature of the cell and sting/crystal are controlled to an accuracy of ±0.1°C and ±0.01°C, respectively. The cell and sting temperatures are controlled and programmed by a microprocessor. The seed crystal is cemented to sting tip and is protected from the growth solution, prior to actual growth, by a cap assembly. Initially the cap is in position to cover the seed crystal and is retracted at the proper temperature according to the time-line.

In the absence of convection, over a long period, the solute concentration around the crystal will drop, tending to lower the growth rate to a very low level if isothermal conditions are maintained. To maintain a constant and as far as possible maximum growth rate, without formation of inclusions, the temperature of the crystal surface must be lowered in a controlled fashion. This can be done by programming down the temperature of the wall of the growth cell. However, in the absence of convection, a change of temperature of the wall requires a long time to reach the crystal. On the other hand, controlling the temperature of the sting/crystal should allow the growth rate to be held constant. If only the sting temperature is controlled, then thermal stresses arise in the crystal, so both sting/crystal and wall temperatures were controlled. The temperature decrease for the sting/crystal and walls was predetermined [4]. The flight temperature profile for the two growth runs is given in Figures 2 and 3.

Two crystal growth runs were successfully performed during the mission. In both experiment runs the starting seed crystal was TGS crystal discs with (001) orientation, 3.42 mm thickness, and 15.07 mm and 9.98 mm diameter, respectively. The first experiment run in which (010) oriented seed was planned to be used could not be completed due to some hardware problems. The second experiment run was performed for 58 hr where both sting/crystal and walls were cooled at a programmed rate, where $T_{sting} < T_{sol} < T_{sat}$. The third run was accomplished in 32.2 hr, where $T_{sting} = T_{sol} < T_{sat}$. The total average growth for both crystals were ~0.4 mm. The growth, however, was not quite uniform across the exposed face due to some apparent damage to seed prior to growth. There was less growth in the center of the seed (Fig. 4). The crystals were cleaved perpendicular to (001) face to test the quality of (010) face as a detector and for other pyroelectric properties.

The preliminary results to date indicate:

1) No apparent visible interface between the seed and the space grown crystal, indicating a diffusion controlled growth (Fig. 5).

2) A typical interferogram reconstructed (Fig. 6) for experiment run three from the flight hologram shows an axially symmetric concentration field around the growing crystal, thereby indicating diffusion controlled growth. These interferograms will be later digitized to determine concentration and temperature fields around the growing crystals. This will then be compared with the theoretically computed data using a finite difference technique [5].

3) The normalized detectivity D* (1000°K, 15 Hz, 1 Hz) for space grown crystal No. 204 for 3 mil thickness (1.0×10^8 W^{-1} cm $Hz^{1/2}$) is somewhat less than the best Earth grown crystal detectors for sample thickness of 0.7 mil thickness (1.0×10^9 W^{-1} cm $Hz^{1/2}$). Further work is in progress.

4) The higher pyroelectric coefficient (~43 nC/cm^2°C), and the shape of the hysteresis loop indicates a good crystal quality.

5) The observed growth rate during the flight agrees with the theoretically predicted growth rate with a diffusion coefficient of 2×10^{-5} cm^2/sec [5].

6) The cooled sting technique of solution crystal growth was successfully tested.

7) A quasi-steady state acceleration environment of 4×10^{-7} g has been measured for drifting crystallites in the growth cell as seen from optical holograms [6]. Also a vibratory environment of 10^{-3} g's at frequencies of 10 Hz and above have been measured using accelerometers attached to FES.

Further studies on crystal characteristics and analysis of optical holograms are in progress and will be reported elsewhere.

ACKNOWLEDGMENTS

The authors are grateful to the entire crew of the Spacelab-3 mission and in particular to Don Lind and Lodewijk Van den Berg, for successfully performing the experiment. The authors would like to thank NASA for the support of this program through contract NAS8-32945. Thanks are also due to Rudy Ruff, William Witherow, Don Reiss and many other NASA personnel for the help during the flight and during the preparation of the experiment. Thanks are due to Hak Do Yoo for help in the theoretical computations.

REFERENCES

1. Lal, R. B., Aggarwal, M. D., Kroes, R. L., and Wilcox, W. R.: Phys. Stat. Sol. (a), Vol. 80, 1983, p. 547.

2. Materials Processing in Spacelab-3, Applications Payload Projects, NASA/MSFC, Code JA63, Huntsville, Alabama 35812.

3. Owen, R. B. and Kroes, R. L.: Optics News, Vol. 11, No. 7, July 1985.

4. Liu, L. C., Wilcox, W. R., Kroes, R., and Lal, R. B.: Materials Processing in Reduced Gravity Environment of Space. North Holland Publishing Co., Inc., New York, 1982.

5. Yoo, Hak Do., Ph.D. Thesis, Department of Chemical Engineering, Clarkson University, Potsdam, New York, 1986.

6. R. J. Naumann (Private Communication).

ORIGINAL PAGE IS
OF POOR QUALITY

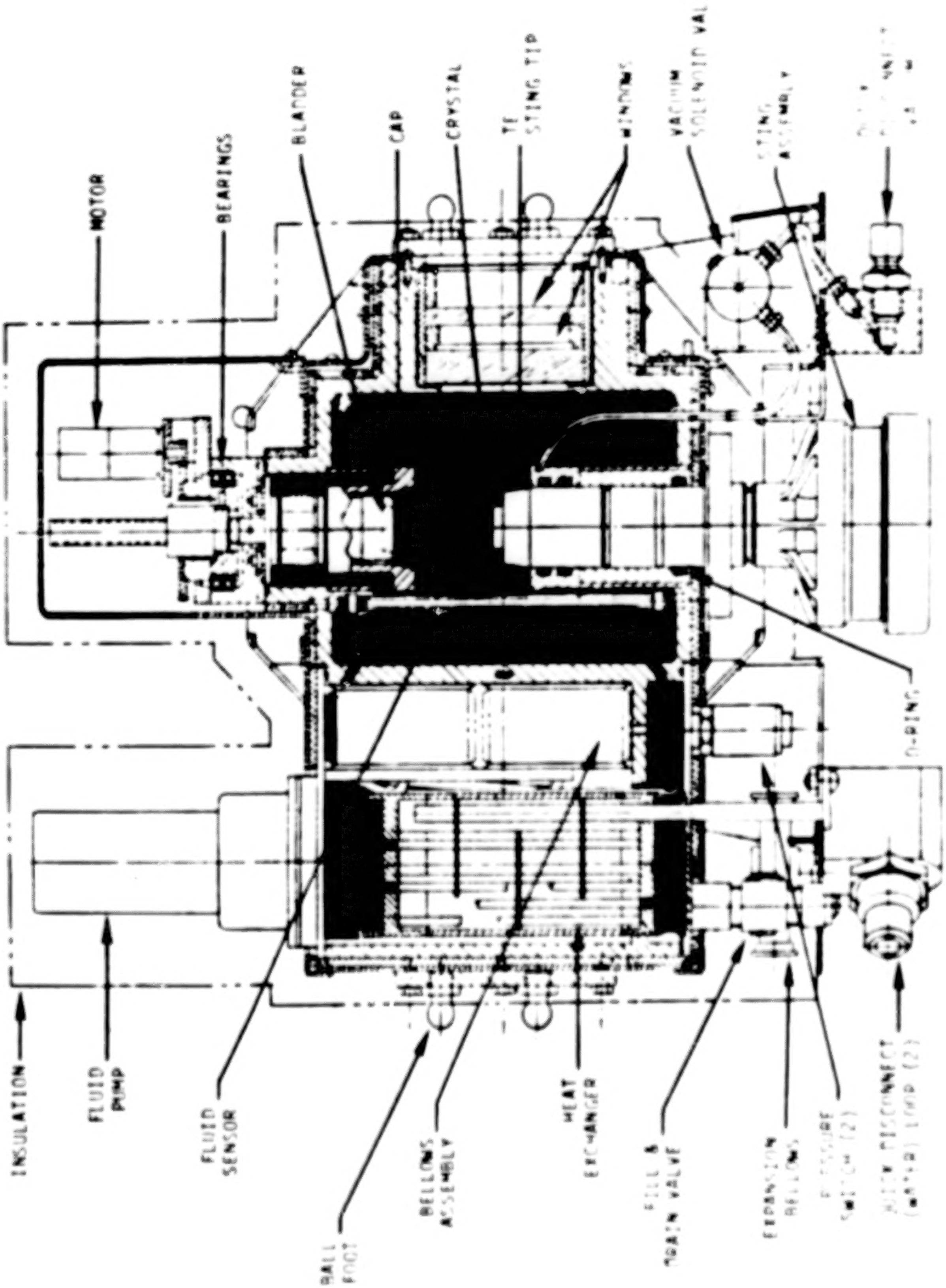

Figure 1. FES crystal growth flight cell.

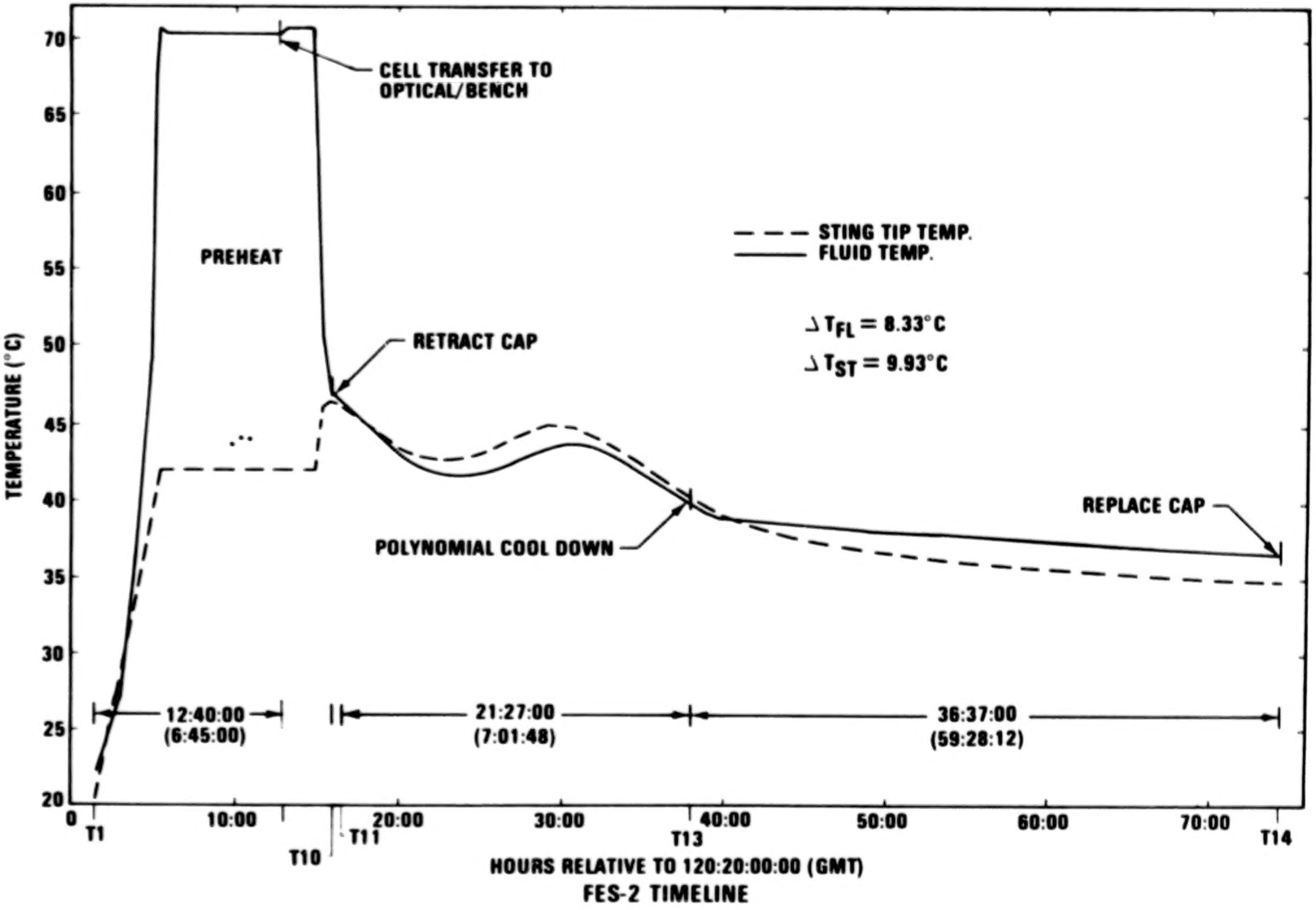

Figure 2. Flight time-line for second experiment run.

ORIGINAL PAGE IS
OF POOR QUALITY

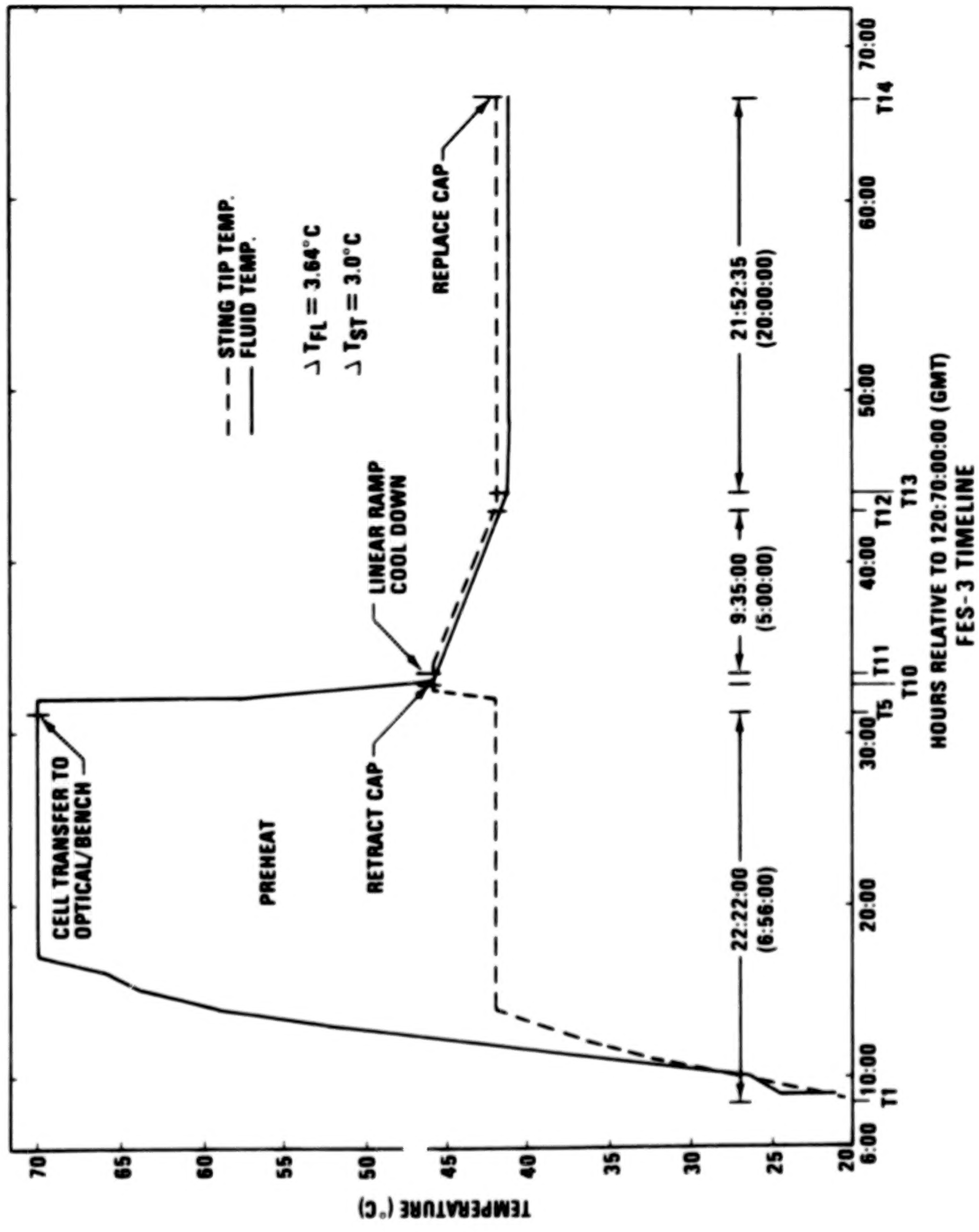

Figure 3. Flight time-line for third experiment run.

ORIGINAL PAGE IS
OF POOR QUALITY

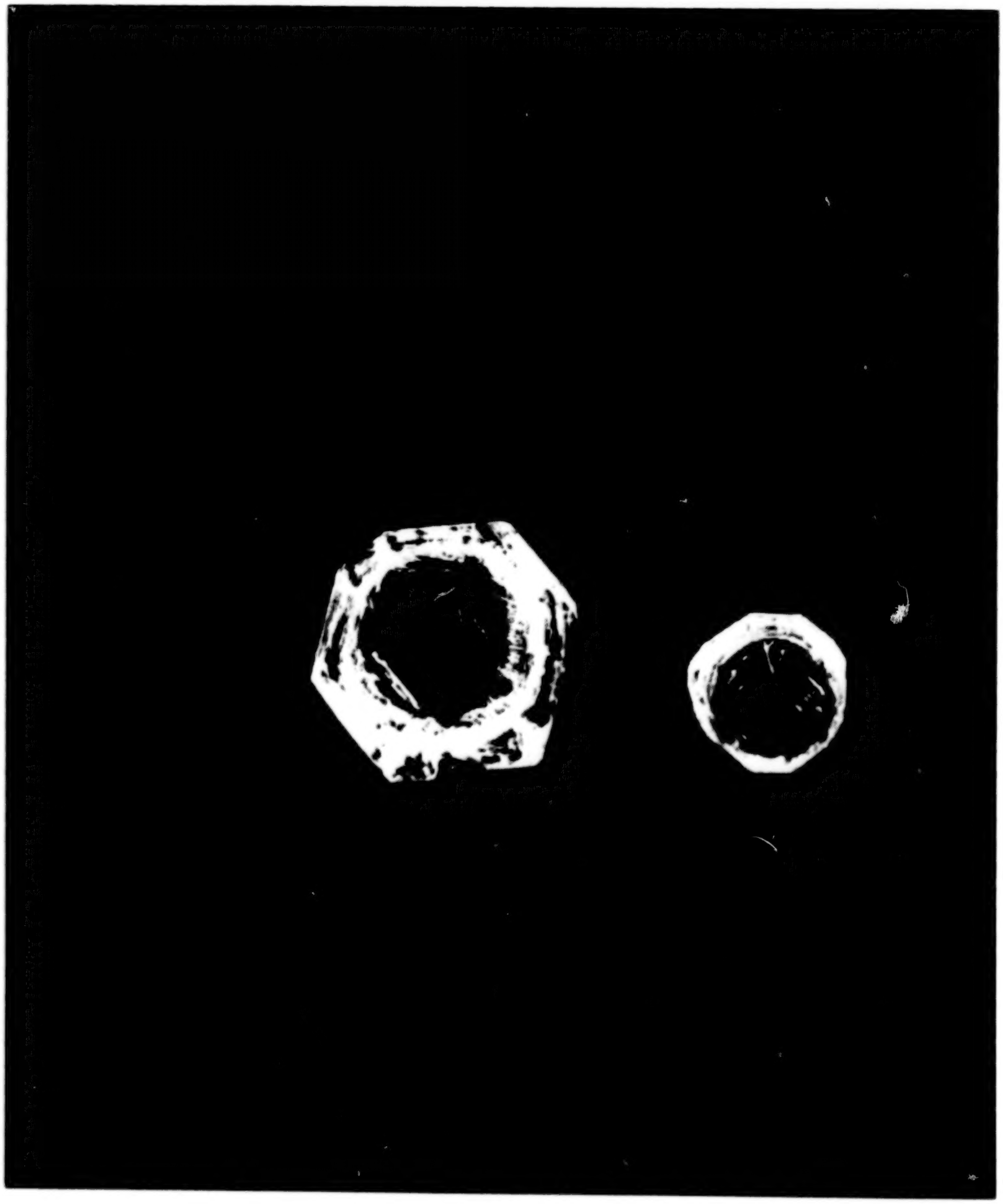

Figure 4. TGS crystals grown during SL-3 mission. The larger crystal was grown during second run and the smaller during third run.

ORIGINAL PAGE IS
OF POOR QUALITY

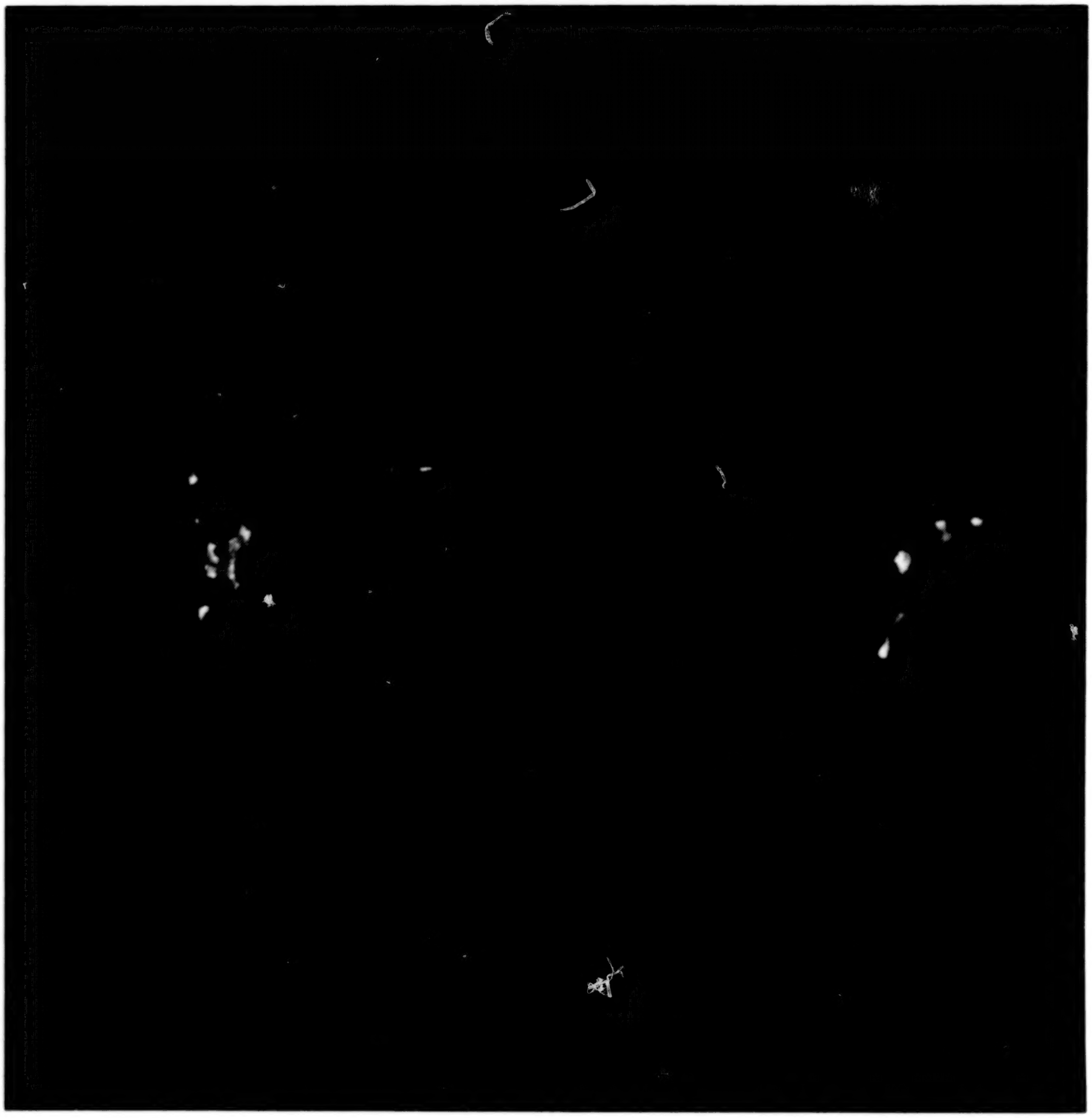

Figure 5. (010) Slice, lapped and polished from crystal No. 204 (third run).

ORIGINAL PAGE IS
OF POOR QUALITY

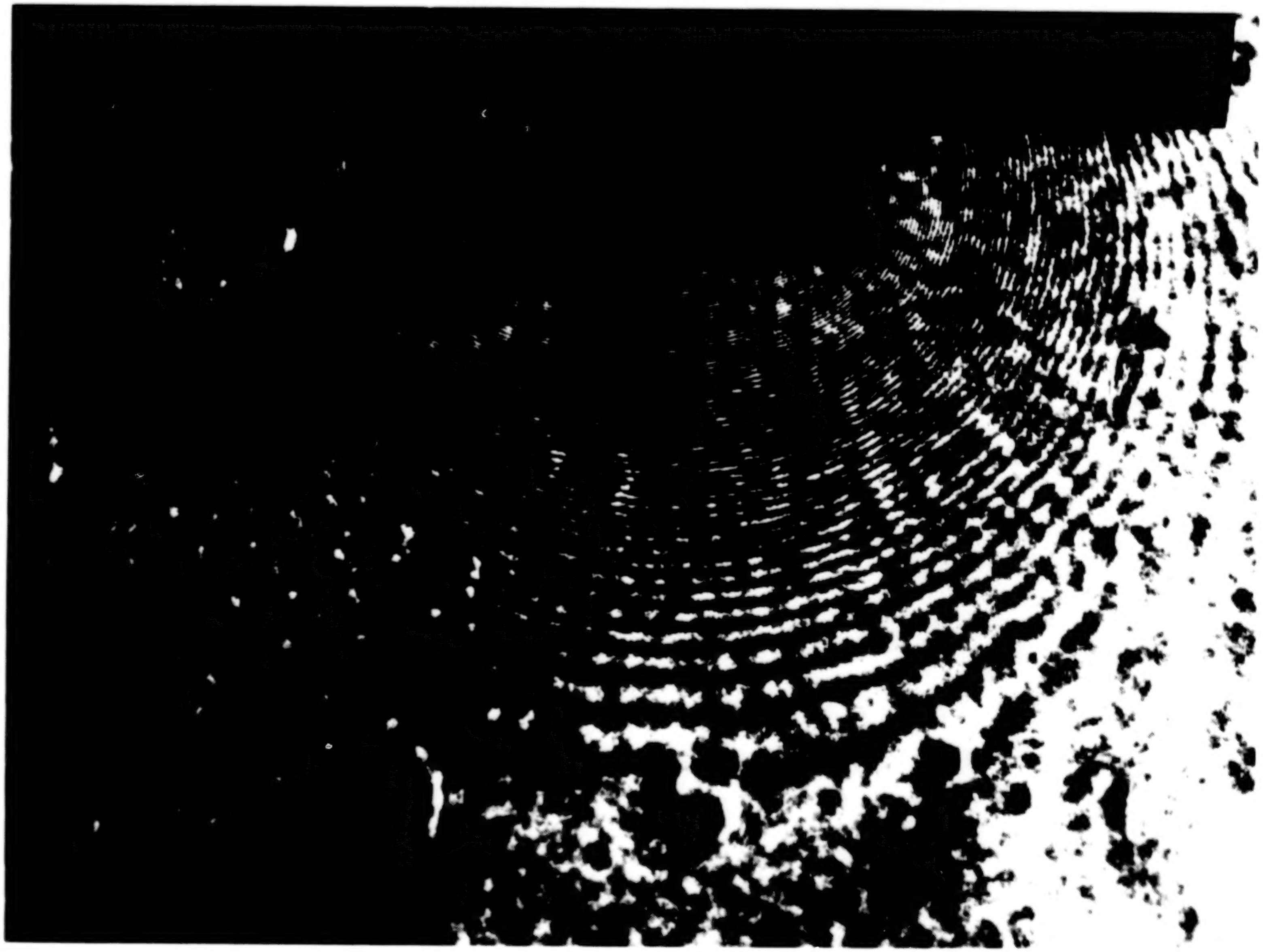

Figure 6. Reconstructed interferogram during grow-mode for third experiment run.

N87-22107

DYNAMICS OF ROTATING AND OSCILLATING DROPS

T. G. Wang, E. H. Trinh, A. P. Croonquist, and D. D. Elleman
Jet Propulsion Laboratory
California Institute of Technology
Pasadena, CA 91109

INTRODUCTION

This experiment was the first investigation into the dynamics of rotation and oscillation of a freely suspended liquid drop under the influence of surface tension and positioned inside an experimental apparatus by acoustic forces in the low acceleration environment of Spacelab 3. After a drop was observed to be spherical and stably located at the center of the chamber it was set into rotation or oscillation by acoustic torque or modulated radiation pressure force.

EQUILIBRIUM SHAPES OF A ROTATING DROP

When a liquid drop spins slowly, it assumes an axisymmetric shape with respect to the rotation axis. As the rotation rate increases, the axisymmetric shape loses its stability and develops into non-axisymmetric shapes having 2, 3, or 4 lobes. These transitions, or bifurcation points, have been predicted by analytical and numerical techniques [1,2]. Experimental evidence of these equilibrium shapes and bifurcation points has been observed in the laboratory using immiscible liquids in neutral buoyancy tanks [3]. However, these results cannot be correlated with theoretical predictions because of the viscous stresses and inertial drag exerted by the host fluid.

Mixtures of glycerin and water were used to form drops with various viscosities for this experiment. Typically, several spin-up and spin-down sequences were performed for a given experimental run with the drop shapes recorded on cinefilm. Figure 1 shows experimental data for a 100 cSt liquid drop, 3 cc in volume, with a rotational acceleration of about 0.01 rev/sec^2. The data yields very good agreement with theoretical predictions in the axisymmetric region, but an obvious difference occurs in the location of the bifurcation point: experimentally ω(II) was 0.47, and theory gives 0.56. This difference suggests that the axisymmetric shapes are less stable than predicted by the theory in the region near the bifurcation point [4]. In Figure 1, the rotation rate has been normalized to the frequency of the first mode of shape oscillations, and one-half of the maximum equatorial discussion of the deformed drop (RMAX) has been divided by the radius of the initially spherical drop (RO).

SHAPE OSCILLATION OF A DROP

The oscillation experiment on this flight was curtailed due to lack of operation time and sub-nominal performance of the instrument. Nevertheless, the available data suggest to a hard non-linearity in the resonance frequencies for shape oscillations as the amplitude grows larger (shown in Figure 2). This is contrary to ground-based experiments which suggest a soft non-linearity [5]. The results of Figure 2 have been obtained by observing the free decay of an initially deformed drop. The resulting shape oscillations are of the oblate-prolate type.

CONCLUSION

In conclusion, the availability of low gravity environment of the Spacelab flight has provided the first opportunity to perform drop dynamics experiments for the rigorous testing of existing theories.

ACKNOWLEDGMENT

This research carried out in this paper was carried out at the Jet Propulsion Laboratory, California Institute of Technology under contract with NASA.

REFERENCES

1. Chandrasekdhar, S.: Proc. of Roy. Soc. London, Vol. A 286, 1965, p. 1.

2. Brown, R. A. and Scriven, L. E.: Proc. Roy. Soc. London, Vol. A 371, 1980, p. 331.

3. Tagg, R., Cammack, R. L., Croonquist, A., and Wang, T. G.: JPL Report 900-954, Pasadena, CA, 1979.

4. Wang, T. G., Trinh, E., Croonquist, A., and Elleman, D. D.: Phys. Rev. Lett., 1986.

5. Trinh, E. and Wang, T. G.: J. F. Mech., Vol. 122, 1982, p. 315.

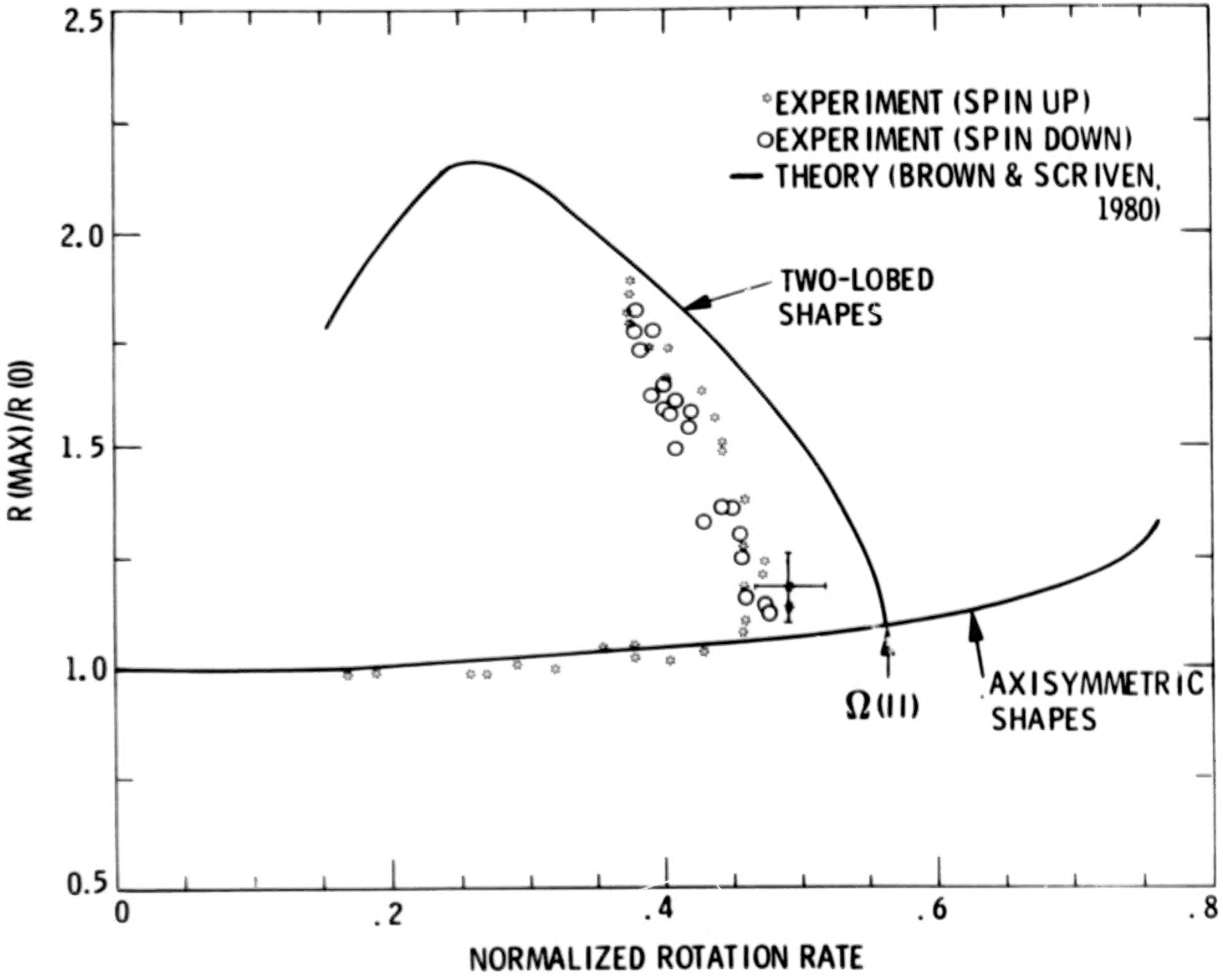

EXPERIMENT (SPIN UP)
EXPERIMENT (SPIN DOWN)
THEORY (BROWN & SCRIVEN, 1980)
TWO-LOBED SHAPES
AXISYMMETRIC SHAPES
$\Omega(11)$
R (MAX)/R (0)
NORMALIZED ROTATION RATE
2.5
2.0
1.5
1.0
0.5
0
.2
.4
.6
.8

Figure 1.

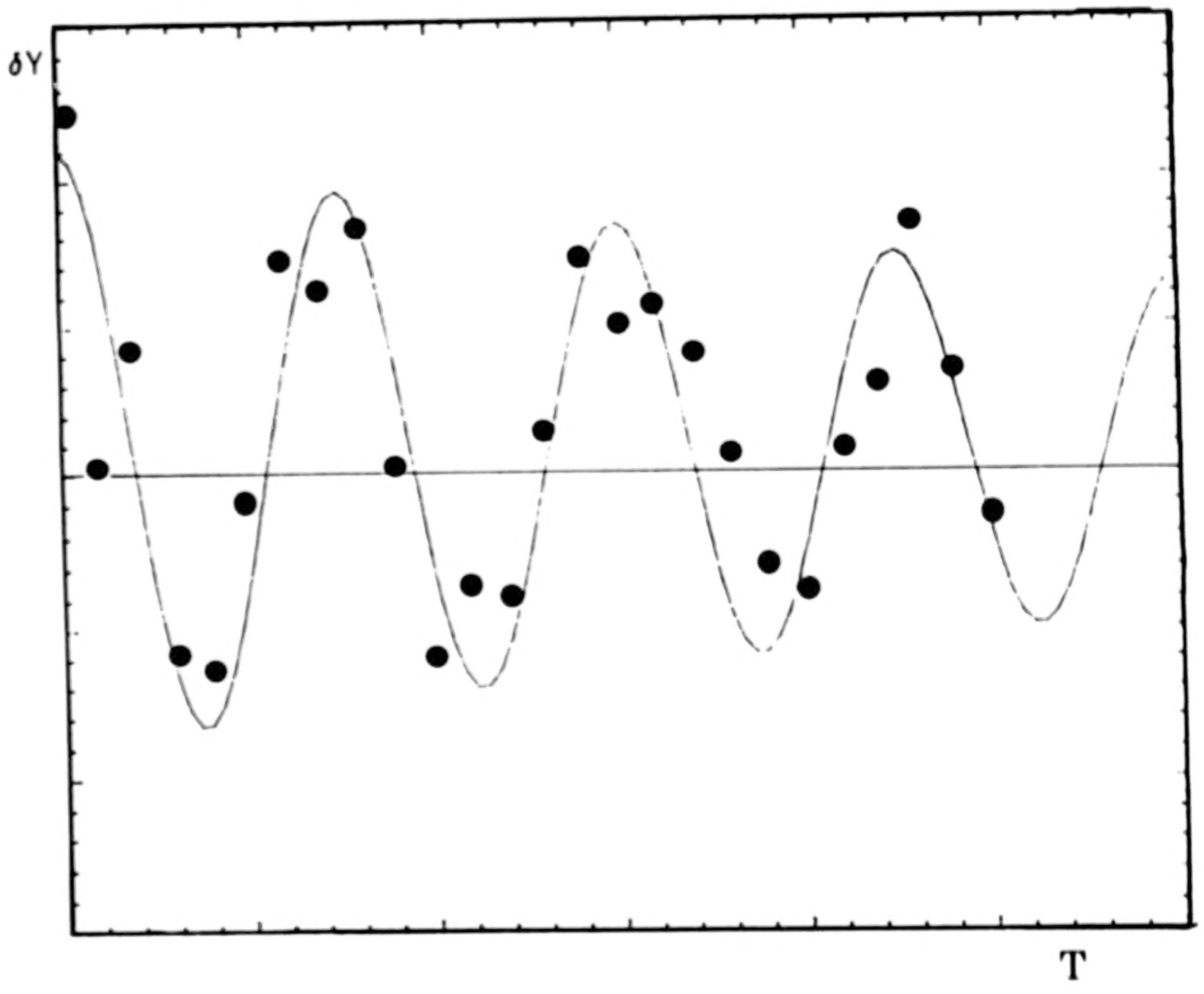

Figure 2. Free decay of an initially deformed drop versus time.

N87-22108

A LABORATORY MODEL OF PLANETARY AND STELLAR CONVECTION

J. E. Hart, J. Toomre, A. E. Deane, and N. E. Hurlburt
Department of Astrophysical, Planetary and Atmospheric Sciences
and Joint Institute for Laboratory Astrophysics
University of Colorado, Boulder, Colorado 80309

G. A. Glatzmaier
Los Alamos National Laboratory, Los Alamos, New Mexico 87545

G. H. Fichtl, F. Leslie, and W. W. Fowlis
NASA Marshall Space Flight Center, Huntsville, Alabama 35812

P. A. Gilman
High Altitude Observatory
National Center for Atmospheric Research, Boulder, Colorado 80307

ABSTRACT

Experiments on thermal convection in a rotating, differentially-heated spherical shell with a radial buoyancy force were conducted in an orbiting microgravity laboratory. A variety of convective structures, or planforms, were observed, depending on the magnitude of the rotation and the nature of the imposed heating distribution. The results are in agreement with numerical simulations that can be conducted at modest parameter values, and suggest possible regimes of motion in rotating planets and stars.

DISCUSSION

Large-scale atmospheric motions on rotating planets and stars are influenced by both buoyancy and Coriolis forces. On a spherical surface the Coriolis force varies with latitude, and this variation is thought to be a fundamental influence in a wide range of phenomena of interest to geophysicists and astrophysicists. These phenomena include cloud-band orientation in planetary atmospheres, differential rotation in the solar atmosphere, the formation of jet-streams, and magnetic dynamo action. Except for flows that are homogeneous, so that buoyancy-driven motions are absent, it has been impossible to properly model even the simplest global motions in the terrestrial laboratory. When the rotation vector Ω is inclined to Earth's gravity g an oscillatory body force results that has no geophysical analog. Therefore, previous laboratory experiments on global circulations have been confined either to: (a) studies of convection near the poles where Ω and g are nearly parallel and the geometry is effectively flat [1], or to (b) studies of motions close to the equator where Ω and g are nearly perpendicular, with the effects of gravity being simulated by centrifugal buoyancy forces associated with very rapid rotation [2,3]. Our laboratory model, which consistently simulates global convective motions in a spherical shell of incompressible fluid, is based on the existence of density-dependent electrostatic forces in a dielectric medium. Because these forces are relatively weak, it is necessary to operate the experiment in an environment where g is small. This report describes our instrument, the "Geophysical Fluid Flow Cell," and outlines results from experiments carried out during its flight aboard the Spacelab 3 microgravity laboratory.

The motion of an incompressible fluid is entirely governed by the vorticity equation, obtained by taking the curl of the momentum equations. In a dielectric liquid subject to imposed electric field gradients, there will be polarization forces present in addition to normal buoyancy. The non-conservative part of these forces contribute to vorticity generation. As shown in Reference 4 this generation is proportional to

$$\text{curl (body force)} = \alpha \nabla T \times \nabla \Phi + \frac{\epsilon\gamma}{2} \nabla T \times \nabla E^2 \quad , \qquad (1)$$

where α is the thermal expansivity, T is the temperature, Φ is the geopotential, E is the electric field, ϵ is the average dielectric constant of the liquid, and γ is the relative change of dielectric constant with temperature. In a self-gravitating fluid Φ is an inverse function of radius r. We would like the first and second terms on the right hand side of equation (1) to be isomorphic functions. A simulation of thermal buoyancy in a radial geopotential may be attained when an electric field $E \cong r^{-2}$ r is generated in the liquid by applying a uniform electric potential across two concentric spherical surfaces. The resulting electrostatic "gravity," which is proportional to ∇E^2, varies like r^{-5} instead of r^{-2}, as might be desired, but it has been shown theoretically that the unstable eigenfunctions and other properties of thermal convection in a non-rotating spherical shell containing a Boussinesq liquid are essentially unaffected by this difference [5]. The magnitude of the electrostatic "gravity" is limited by the breakdown field strength of existing low-viscosity, low-loss dielectrics to about 0.1 g's (or 1 ms^{-2}) in an apparatus of reasonable size. Thus the use of electrodynamic forces to study convection in spherical shells is only practical in the microgravity environment of the Shuttle orbiter.

A diagram of the cell used in our experiment is shown in Figure 1. A dielectric silicone oil of 0.65 centistoke viscosity is contained between two hemispherical shells that form part of a spherical capacitor. We study fluid motions in a single hemisphere because non-radial electric fields occur in the vicinity of the inner sphere's mechanical support which spans the annular gap near the south pole. The inner shell at radius R_i is made of polished nickel, and the outer at radius R_o is a transparent sapphire dome about 1 cm thick. Temperatures are maintained along both these surfaces by a system of heater coils and thermistor sensors installed in a computer-controlled servo loop. The thermal boundary conditions are axisymmetric, but allow for variations of both inner (T_i) and outer (T_o) surface temperature with latitude θ. Although uniform differential heating, with $T_i > T_o$ and independent of θ, is the simplest and most relevant case for modelling objects with spherically symmetric forcing, several experiments were run with a hotter pole. Such statically unstable non-uniform heating is thought to occur in rapidly rotating stars, giving rise to a meridional circulation [6-8] with little-known non-axisymmetric instability properties. Theoretical studies have shown that the spatial patterns or planforms selected by global convective modes are strongly influenced by latitudinal gradients, and that this selection may possibly be related to the structure of Jovian cloudbands [9,10]. To generate the electrostatic gravity, a 300 Hz alternating potential V_o is applied to a transparent conducting coating on the inner wall of the outer hemisphere. The inner sphere is grounded. The field reverses in a period short compared to the charge relaxation time for the fluid. This ensures an absence of electric currents and associated non-geophysical instabilities. In addition the oil has such a low dielectric loss that internal dissipative heating, even with potentials as high as 10 kV, is entirely negligible. The cell assembly including the high-voltage supply and the thermal-control circuitry is mounted on a rotating turntable that maintains a constant but adjustable rotation rate Ω.

Flows are visualized by Schlieren and shadowgraph photography. A non-rotating optical train focuses light from a grating onto the inner sphere. Thermally induced refractive index variations in the fluid cause individual rays to bend. When the incident rays are compared with the reflected rays, various measures of the radially-averaged temperature field in the fluid are obtained. Because of space and weight limitations the optical system does not image the whole hemisphere; rather, a circular view extending from equator to pole and covering a quadrant in longitude reaching ±63 deg at 45 deg north is obtained (Fig. 2).

There are several non-dimensional numbers that serve to define the convective flow regimes. The fixed parameters are the Prandtl number P_r = (viscosity ν)/(thermal diffusivity κ) = 8.4 and the aspect ratio R_i/R_o = 2.402 cm/3.300 cm = 0.73. The measure of rotation is taken to be the Taylor number

$$T_a = \frac{4\Omega^2(R_o - R_i)^4}{\nu^2} \tag{2}$$

The Rayleigh number indicates the degree of thermal forcing with respect to dissipation. It is defined by

$$R_a = g_o \frac{\alpha\Delta T_r(R_o - R_i)^3}{\nu\kappa} \tag{3}$$

where g_o is the equivalent electrostatic gravity at $r = R_o$ and $\Delta T_r \equiv T_i - T_o$ is the radial temperature difference across the fluid at the equator. Finally, $H \equiv \Delta T_\theta/\Delta T_r$ compares the imposed pole-to-equator temperature difference at the boundaries to the radial temperature difference (with H vanishing for uniform heating).

A sequence of Schlieren images for cases with uniform imposed temperature on each hemisphere (H = 0) is shown in Figure 3. In Figure 3A the Taylor number is relatively small and rotational effects are weak. At a Rayleigh number above about 2×10^3, convective instabilities form and break the spherical symmetry of the conductive thermal balance that exists at smaller R_a. The tessellated pattern shows little influence of rotation, and evolves slowly with time. The patterns are suggestive of those predicted by a theory [11] for planform selection in a non-rotating shell without the rigid equatorial boundary. The observed convection has narrow updrafts along the edges of the cells and broad sinking regions in cell centers. One possible explanation is that this is a result of radial asymmetry in the "gravity" which is concentrated near the inner sphere. For example, it has been shown [12] that planar convection in a layer with unstable thermal gradients concentrated near the lower wall is dominated by hexagons with downflow in the center and upflow at the edges. Another explanation, suggested by similar results from our numerical simulations of flows with either r^{-2} or r^{-5} gravity, is that the narrow updrafts are a result of strong nonlinear interactions in the spherical geometry.

As the Taylor number is increased, the influence of rotation becomes larger (Fig. 3B). The weakly supercritical convective modes begin to feel the Taylor-Proudman constaint [13] that the motion should be invariant in the direction of Ω. In agreement with earlier analytical and numerical calculations [14,15] the boundaries of the convection cells are aligned in the north-south direction. The convection dies out somewhat north of the critical latitude on the outer boundary, here 43 deg, where a tangent cylinder drawn parallel to Ω just intersects the inner sphere at the equator. These low-latitude "banana cells" have a prograde propagation which is revealed in extended sequences of shadowgraph images. The banana cells dominate the weakly unstable flows (i.e., modest R_a) at all T_a greater than about 10^4. However, as R_a is increased, mid-latitude and polar modes become unstable as well. In Figure 3C, interactions with retrograde-propagating mid-latitude convection modes occur at the tips of the banana cells.

This causes a wavering and, at higher R_a, a nearly complete erosion of the banana cells. In Figure 3D, vestiges of the Taylor-Proudman constraint are found only within 20 deg of the equator. The remaining convection is highly turbulent, more horizontally isotropic, and contains most of the rms temperature variance.

A series of experiments with H = 1 is illustrated in Figure 4. Because the pole is hotter than the equator on each boundary, there is no purely conductive motionless state. A meridional circulation always exists, and with even a small amount of rotation substantial zonal flows will be generated. The interaction of this axisymmetric motion with incipient non-axisymmetric convective instabilities leads to the spiral pattern of convection at low T_a (Fig. 4A). The cells tip west (to the right) as one follows an updraft equatorward. The updrafts are narrow and the downdrafts are broad. If R_a is increased at this T_a (Fig. 4B), the thermal fronts along the spiral wave boundaries sharpen and a secondary instability occurs. The resulting defects lead to an irregular pattern that evolves chaotically in time. At larger T_a banana cells reappear at low latitudes. However, irregular spiral waves persist at high latitudes, becoming more axisymmetric (Fig. 4C). At high T_a and high R_a (Fig. 4D) a very complicated turbulent flow is observed. Imbedded in the circulation are fairly stable, mid-latitude, triangularly-shaped waves that appear to be coupled to the low-latitude banana cells. None of the experiments with H = 0 to 2, $R_a = 10^3$ to $\cong 10^5$, $T_a = 10^3$ to $\cong 10^6$ produced any axisymmetric tropical convection resembling, say, Jovian cloud band structure or orientation.

Numerical solution of the governing Boussinesq hydrodynamic equations is practical with supercomputers for some of the lower R_a cases studied experimentally. We have solved the nonlinear three-dimensional problem in spherical geometry using a spectral transform method [16]. The velocity and thermodynamic functions are expanded in spherical harmonics in longitude and latitude, and Chebyshev polynomials in radius. All the conditions of the laboratory experiment are modelled except for the no-slip velocity constraint at the equatorial barrier, which is replaced by a stress-free condition. Computations using a slower finite-difference model, in which the proper equatorial condition can be implemented, indicate that it exerts only a minor quantitative effect on the solutions, although the equatorial barrier may affect the direction of the relatively weak phase propagation at modest T_a. Figure 5A shows the mid-depth radial velocity pattern, which is essentially the same as the radially-averaged thermal pattern, for the conditions of Figure 3B. Although there is some wavering of the banana cells, the mid-latitude modes are weak. The thermal spectrum peaks near wavenumber m = 15 (Fig. 6A); the pattern translates westward (retrograde) at a low rate of ≅0.45 deg per rotation. The experiment is dominated by wavenumber 15, in good agreement with the calculation. The differential rotation produced in the numerical model is retrograde at the equator and contributes about 1 percent to the total kinetic energy. The experiment confirms previous predictions [17, 18] that both rigid boundary conditions and the relatively high Prandtl number tend to suppress differential rotation, when compared to the large zonally-averaged flows predicted in models of solar convection with stress-free boundaries and a Prandtl number of unity [19]. A numerical simulation of a rapidly rotating and more unstable case is shown in Figure 5B for the same conditions as Figure 3C. The calculated flow now includes a substantial contribution from polar and mid-latitude modes that are observed to interact with the tips of the banana cells exactly as seen in the experiment. The thermal spectrum (Fig. 6B) is broad with a wave maximum at longitudinal wavenumber 17 which compares favorably with the experimental value of 18. In this case the computed differential rotation is concentrated near the poles with a structure that depends on the meridional circulation there. Typically there is downward flow at the pole with prograde differential rotation in the upper part of the fluid shell and retrograde differential rotation in the lower part. Details of the maintenance of the differential rotation and other aspects of the computed solutions will be reported separately [20]. Further calculations aimed at understanding the spiral waves which occur at $H \simeq 1$, and their interactions with the banana cells, are underway.

The experiments have supplied new data on pattern selection and low and mid-latitude interactions in rotating thermally unstable flows. Physical interpretation of these results, and future experiments planned on secondary instability and the transition to turbulence, should provide new insights into nonlinear processes important in the dynamics of planetary and stellar convection.

REFERENCES AND NOTES

1. Rossby, H. T.: J. Fluid Mech., Vol. 36, 1969, p. 309.

2. Busse, F. H. and Carrigan, C. R.: Science, Vol. 191, 1976, p. 81.

3. Carrigan, C. R. and Busse, F. H.: J. Fluid Mech., Vol. 126, 1983, p. 287.

4. Hart, J. E.: NASA Report CR-2753, 1976, 66 pp. A general discussion of electrohydrodynamics is provided by J. R. Melcher and G. I. Taylor [Annu. Rev. Fluid Mech., Vol. 1, 1969, p. 111]. An implementation of this concept in cylindrical geometry is presented by B. Chandra and D. E. Smylie [Geophys. Fluid Dyn., Vol, 3, 1972, p. 211].

5. Hart, J. E. and Toomre, J.: NASA Report NAS8-31958, 1977, 65 pp. For aspect ratios R_i/R_o smaller than that used in our instrument the differences can become significant.

6. Eddington, A. J.: Observatory, Vol. 48, 1925, p. 73.

7. Sweet, P. A.: Mon. Not. Roy. Astron. Soc., Vol. 110, 1950, p. 548.

8. Tassoul, J. L.: Theory of Rotating Stars, Princeton University Press, 1978.

9. Hathaway, D. H., Gilman, P. A., and Toomre, J.: Geophys. Astrophys. Fluid Dyn., Vol. 13, 1979, p. 287.

10. Hathaway, D. H., Toomre, J., and Gilman, P. A.: Geophys. Astrophys. Fluid Dyn., Vol. 15, 1980, p. 7.

11. Busse, F. H.: J. Fluid Mech., Vol. 72, 1975, p. 67.

12. Krishnamurti, R.: J. Atmos. Sci., Vol. 32, 1975, p. 1353.

13. Greenspan, H. P.: The Theory of Rotating Fluids, Cambridge Univ. Press, 1968.

14. Busse, F. H.: J. Fluid Mech., Vol. 44, 1970, p. 441.

15. Gilman, P. A.: J. Atmos. Sci., Vol. 32, 1975, p. 1331.

16. Glatzmaier, G. A.: J. Computational Phys., Vol. 55, 1984, p. 461.

17. Gilman, P. A.: Geophys. Astrophys. Fluid Dyn., Vol. 11, 1978, p. 181. For the same values of Rayleigh, Taylor, and Prandtl numbers, no-slip boundaries for convection in a spherical shell reduce the induced differential rotation kinetic energy by a factor of about 25, compared to the stress-free boundary case [see (19)].

18. Gilman, P. A.: J. Fluid Mech., Vol. 57, 1973, p. 381. Although this calculation is for a thin annulus in Cartesian geometry rather than a spherical shell, it shows that the induced differential rotation kinetic energy for a Prandtl number of 8 is reduced, relative to the convection kinetic energy that drives it, by about a factor of 8 when compared to the Prandtl number unity case (approximately a linear relationship in this Prandtl number range).

19. Gilman, P. A.: Geophys. Astrophys. Fluid Dyn., Vol. 8, 1977, p. 93.

20. Glatzmaier, G. A, Hart, J. E., and Toomre, J.: in preparation.

21. This research is supported in part by NASA through contract NAS8-31958 to the University of Colorado. The National Center for Atmospheric Research is sponsored by the National Science Foundation. We thank B. Fiedler, E. Graham, D. Hathaway, W. Merryfield and J. Miller for substantial help with analysis and modelling during the development phases of this experiment. The engineering and fabrication of the instrument was guided by R. Kroger of Aerojet Electrosystems Company, and additional technical support was provided by Marshall Space Flight Center.

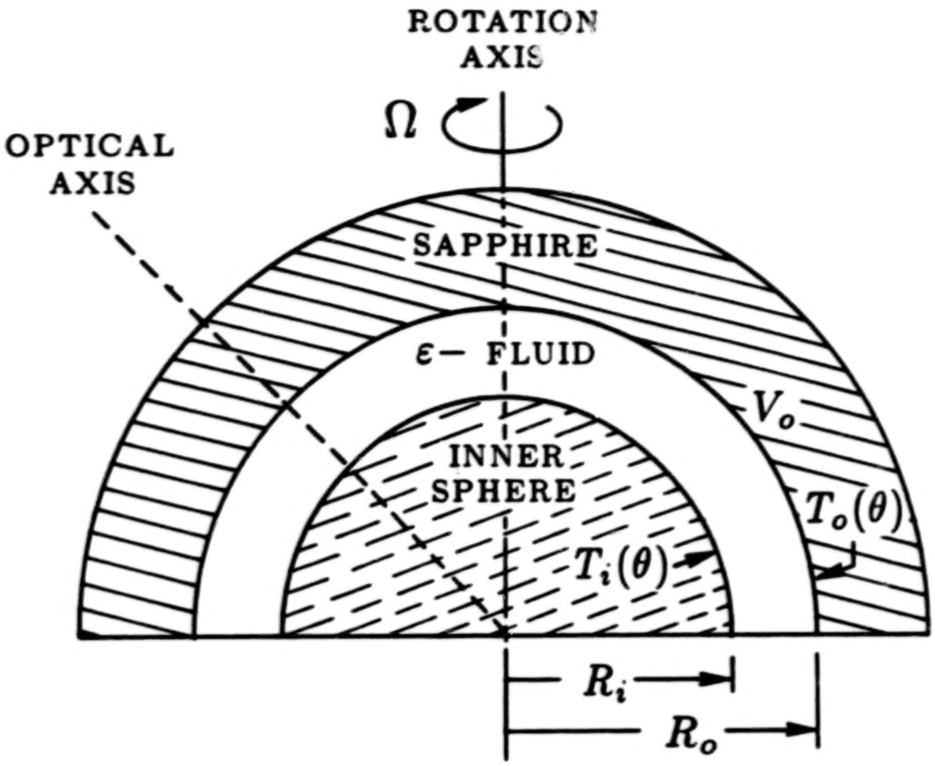

Figure 1. Cross-section of the experimental cell used to study thermal convection under the effects of rotation Ω in a hemispherical shell of fluid in the presence of an electrical analog of a radial gravity field. The inner radius of the shell of fluid is $R_i = 2.4$ cm and the outer radius $R_0 = 3.3$ cm. The electrostatic gravity is achieved by imposing an alternating electrical potential V_0 across the fluid shell. The dielectric silicone working fluid is bounded on the outside by a transparent sapphire dome to allow optical probing of the convective flows and thermal structures that result from differential heating.

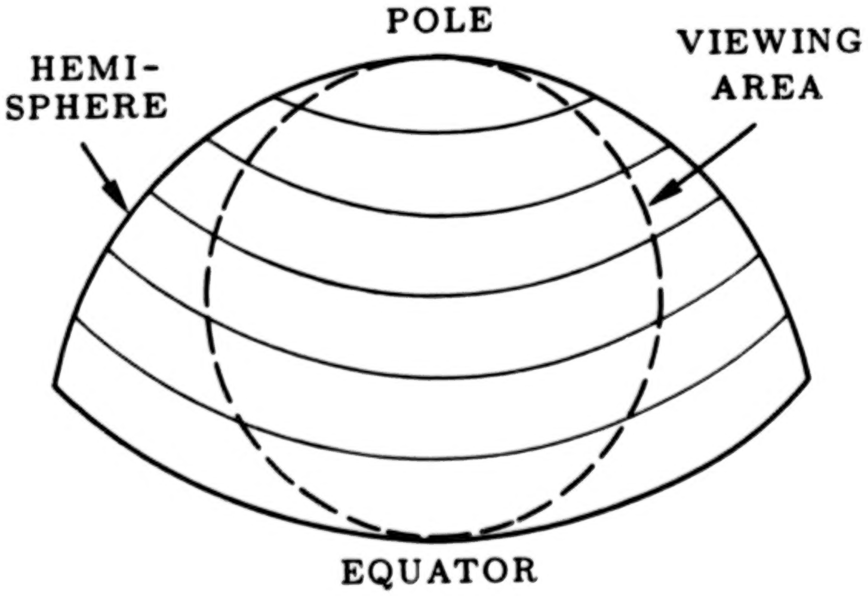

Figure 2. Sketch of the Schlieren viewing configuration with respect to the hemispherical shell.

ORIGINAL PAGE IS
OF POOR QUALITY

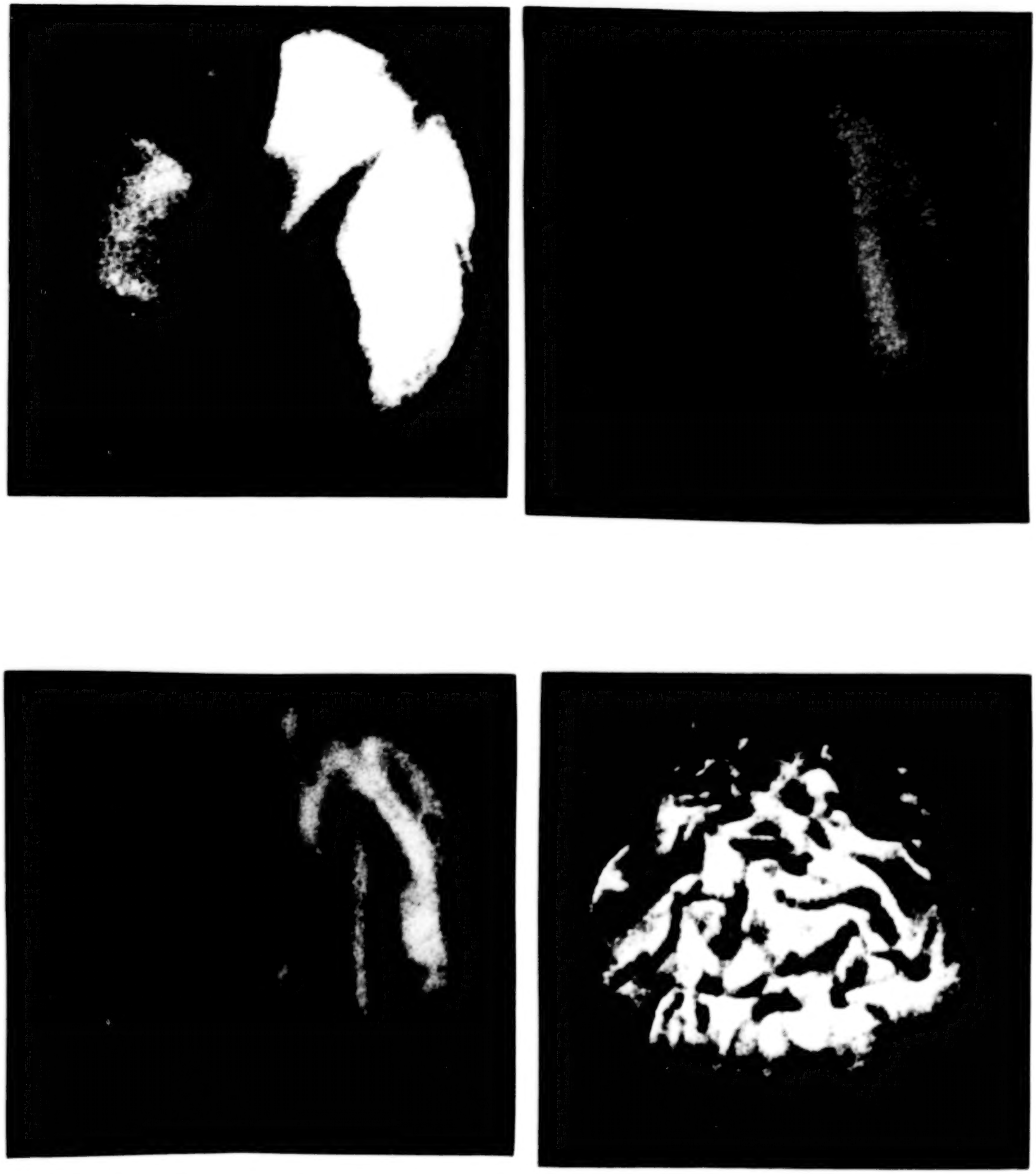

Figure 3. Planforms for the convection as observed with Schlieren photography in experiments with a uniform radial temperature difference imposed between the inner and outer spheres. (H = 0). These circular views of a portion of the hemisphere extend from the pole at the top to the equator at the bottom, as indicated in Figure 2. The basic rotation is from right (west) to left (east).

ORIGINAL PAGE IS
OF POOR QUALITY

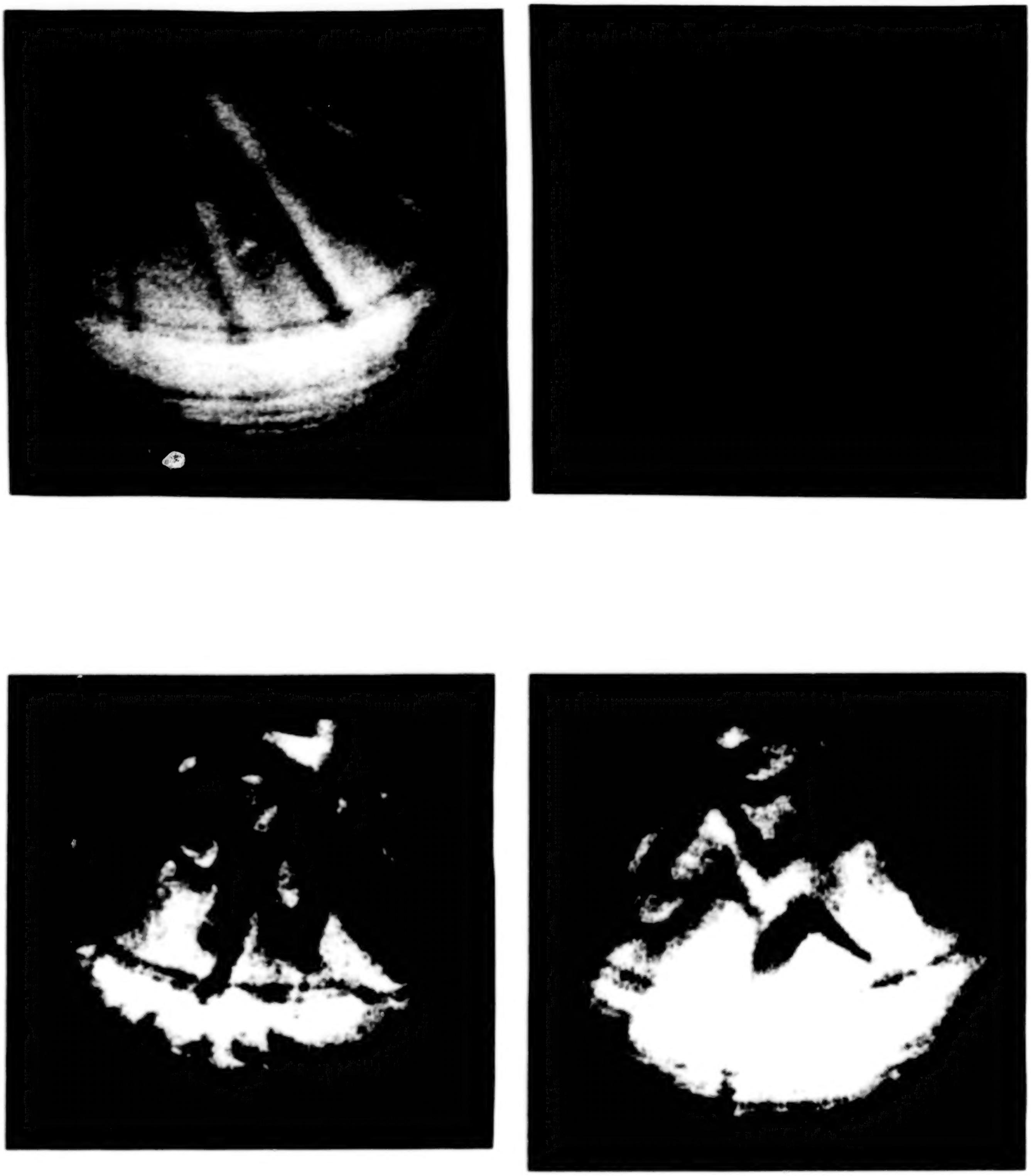

Figure 4. Planforms for the convection observed in experiments with temperature increasing poleward on each spherical boundary in addition to a uniform radial temperature difference between the spheres (H = 1).

ORIGINAL PAGE IS
OF POOR QUALITY

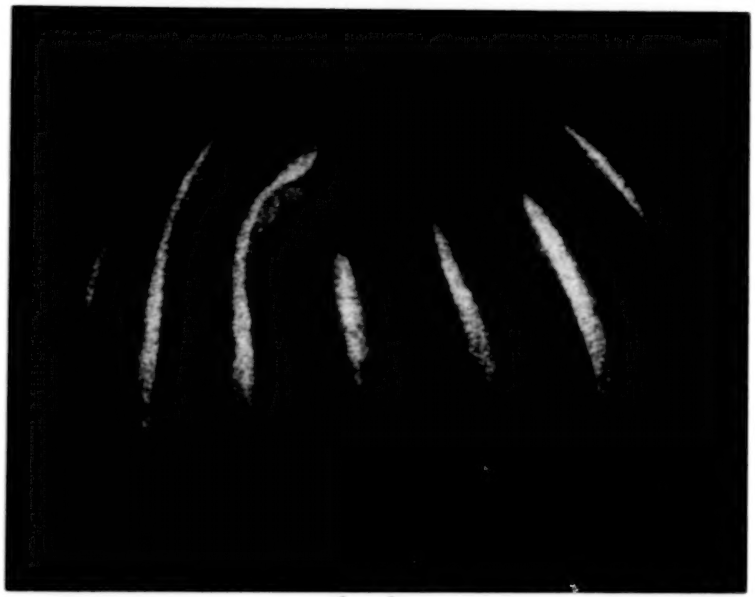

(a)

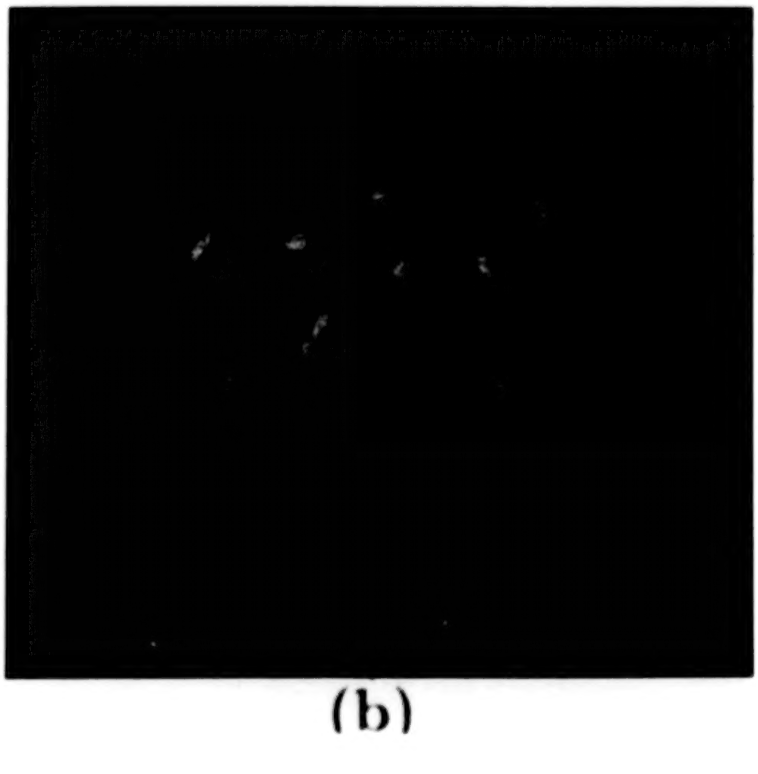

(b)

Figure 5. Surface plots of computed radial velocity at mid-depth in a rotating hemispherical shell as obtained from three-dimensional numerical simulations. (A) For conditions corresponding to those in Figure 3B and (B) to those in Figure 3C.

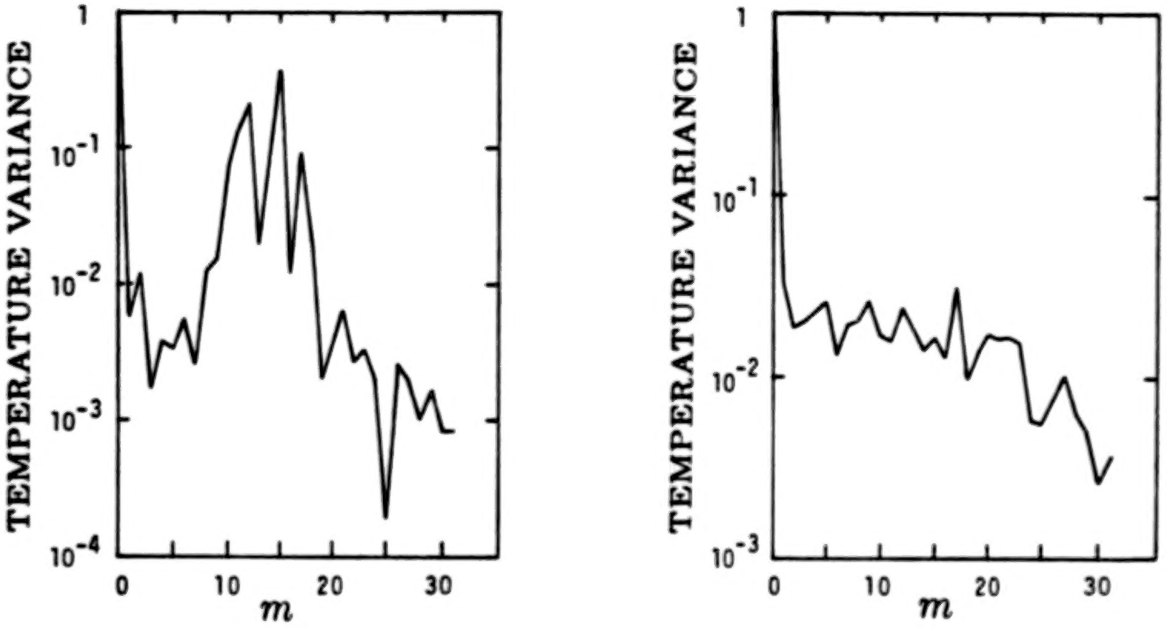

(a) (b)

Figure 6. Latitudinally and radially-averaged rms temperature variance as a function of longitudinal wavenumber m for the numerically computed flows of Figures 5A and 5B.

N87-22109

HIGH RESOLUTION INFRARED SPECTROSCOPY FROM SPACE: A PRELIMINARY REPORT ON THE RESULTS OF THE ATMOSPHERIC TRACE MODULE SPECTROSCOPY (ATMOS) EXPERIMENT ON SPACELAB 3

Crofton B. Farmer and Odell F. Raper
Jet Propulsion Laboratory
California Institute of Technology

ABSTRACT

The ATMOS (Atmospheric Trace Molecule Spectroscopy) experiment has the broad purpose of investigating the physical structure, chemistry, and dynamics of the upper atmosphere through the study of the distributions of the neutral minor and trace constituents and their seasonal and long-term variations. The technique used is high-resolution infrared absorption spectroscopy using the Sun as the radiation source, observing the changes in the transmission of the atmosphere as the line-of-sight from the Sun to the spacecraft penetrates the atmosphere close to the Earth's limb at sunrise and sunset. During these periods, interferograms are generated at the rate of one each second which yield, when transformed, high resolution (0.01 cm^{-1}) spectra covering the 2.2 to 16 micron region of the infrared. Twenty such occultations were recorded during the Spacelab 3 flight, which have produced concentration profiles for a large number of minor and trace upper atmospheric species in both the northern and southern hemispheres. Several of these species have not previously been observed in spectroscopic data. The data reduction and analysis procedures used following the flight are discussed in the present paper; a number of examples of the spectra obtained are shown, and a bar graph of the species detected thus far in the analysis is given which shows the altitude ranges for which concentration profiles have been retrieved.

INTRODUCTION

Infrared absorption spectroscopy, using the Sun as the radiation source, has proven to be one of the most powerful methods for studying the composition and structure of the Earth's atmosphere. Such measurements can provide information on the vertical and spatial distribution of the molecular constituents of the atmosphere, the local temperature and pressure regimes, and the photochemical, thermodynamic, and radiative transfer processes which are occurring there. Studies of this kind were made in the past from the surface and from low-flying aircraft [1] and have progressed more recently to high-flying aircraft and balloons [2]. It has been apparent for some time that the next logical step in the utilization of spectroscopic techniques for atmospheric measurements is to make the observations from space. Such measurements afford the possibility of probing the entire altitude range of the atmosphere, and offer the additional advantage of providing global coverage. The Atmospheric Trace Molecule Spectroscopy (ATMOS) investigation was conceived and implemented to take advantage of the capabilities of the Space Transportation System (STS) which provides the space shuttle as a platform for making such measurements from space and the Tracking Data and Relay Satellite System (TDRSS) for relaying high data rate information to the ground.

THE ATMOS INSTRUMENT

Against the two obvious advantages of probing the upper atmosphere from space there lies the disadvantage of the very rapid rates at which the solar occultations occur while in Earth orbit. This disadvantage is compounded by the fact that there are more than 40 atmospheric molecular species of interest today which absorb at a wide range of frequencies in the near and middle infrared, making broad wavelength coverage at very fast scan rates a necessity. The only technique capable of acquiring spectra under such conditions is fast Fourier Transform (FFT) spectroscopy; this consideration established the requirements for the sensor (a state-of-the-art Michelson interferometer) to be used in the investigation.

The ATMOS instrument, described in Reference 4 and illustrated in Figure 1, was designed and built by Honeywell Electro-Optics Center (HEOC) in Wilmington, Massachusetts; an optical diagram tracing the radiation path through the instrument is shown in Figure 2. The salient characteristics of the instrument, dictated by the demanding task of acquiring broad band, high resolution spectra from space, are listed in Table 1. The one-second scan time shown in the table is based on the need for good vertical resolution in the measurements and the assumption of a worst-case occultation rate of 2.5 km per second. In order to reduce the sampling rate and improve the signal-to-noise characteristics of the spectra, the overall spectral range of interest, from 550 to 4800 cm^{-1}, is divided into four smaller, overlapping wavelength intervals using optical filters whose bandpasses fit within the alias limits created by sampling every two or every three fringes of the He-Ne reference laser. The wavelength intervals covered by these filters, together with those molecules of interest having absorption features which fall within each region, are shown in Table 2. Not shown in the table are two additional filters including a notch filter (No. 5) covering the regions from 600 to 700 cm^{-1} and from 2000 to 2500 cm^{-1} (used for temperature sounding and thermodynamic equilibrium studies), and a broad survey filter (No. 6) which covers the entire spectral region from 600 to 3600 cm^{-1} with reduced signal-to-noise performance.

MISSION PROFILE

The Spacelab 3 mission was flown by the space shuttle Challenger during the period from April 29, 1985, to May 6, 1985. The launch time for the mission was chosen by the ATMOS Science Team such that sunset occultations during the flight would occur in a broad band of northern latitudes encompassing the region from 10° to 40°N, and sunsets in the southern latitude band from 40° to 50°S. Over 50 sunset and sunrise occultations had been allocated to ATMOS to fulfill the primary objective of detecting as many as possible of the minor and trace species present in the upper atmosphere and determining their vertical distributions, and the secondary objectives as well as discerning their latitudinal and longitudinal distributions. The use of the optical filters available in the instrument was planned such that good sampling of the latitudinal and longitudinal distributions of each of the species could be obtained.

Very early in the mission, engineering telemetry data from the instrument indicated a leak in a pressurized housing which contained the He-Ne reference laser. This information forewarned that the housing would eventually reach a pressure low enough to cause arcing in the high voltage power supply for the laser. Prior to the shutdown of the instrument 20 sunset and sunrise occultations were obtained. This number of occultations was completely sufficient to satisfy the primary objectives of the flight; a summary listing of these occultations and their geographical locations is shown in Table 3. In all, the total raw data returned during the abbreviated mission amounted to about 9 gigabytes.

DATA REDUCTION

One of the marked disadvantages of interferometric spectroscopy, at least until recent times, has been the amount of processing required on the raw data contained in the interferograms. Because of the large dynamic range of the data in an interferogram, most interferometers contain both a high and a low gain data channel and these must be merged into one data stream at the beginning of the reduction period. Corrections for phase distortion must be applied to a subset of the interferogram points in the region of the zero path difference fringe, and finally the entire set of interferogram points must be Fourier-transformed from interferometric space to spectral space in order to provide data records suitable for examination. Not until the evolution of modern computers and array processors, with their large throughput capacities and ultra-high operational speeds, did large scale measurements with high resolution Fourier transform spectrometers become a viable technique. In the case of ATMOS, a dedicated facility was constituted at JPL to accomplish the formidable data reduction and analysis tasks. At the core of this facility are a powerful minicomputer and two fast array processors which can – in a matter of seconds – perform the phase correction and Fourier transformation required to convert a 400,000 point, 16 megabit ATMOS interferogram into a spectrum.

During the Spacelab 3 mission, 3 minutes' worth of data were gathered by the instrument at each occultation opportunity. Since the occultation rates on Spacelab 3 were of the order of 2 km/sec, more than half of the spectra in each occultation set were solar, i.e., were acquired above the Earth's atmosphere and contained features of solar origin only. In order to simplify the analysis task on the atmospheric spectra, a number of the solar-only spectra were averaged together for each of the occultations and the resultant spectrum was ratioed against each of the spectra in the set which contained telluric features, effectively removing all of the superimposed solar lines from each spectrum. At a later date, more comprehensive averages of the solar spectra available from the mission will be assembled and the results published as a high signal-to-noise, high resolution solar atlas covering the infrared wavelength region from 2.2 to 16 microns.

DATA ANALYSIS

There are two major phases involved in that part of the analysis of the data leading to profiles of concentration for the minor and trace gases. While initially both may be pursued simultaneously on an iterative basis, the accuracies achieved in the first phase, which involves the extraction of temperature and pressure information from the spectra for each occultation, ultimately establishes the uncertainties associated with the retrieval of the mixing ratio profiles themselves (which constitutes the second phase). In view of this, one of the advantages of the wide spectral coverage and high resolution of the data is the convenient access to spectral features that can be used for determining the vertical profile of pressure and temperature corresponding to each occultation location. Of particular importance in this context are the lines of the 1-0 N_2 quadrupole band that occur between CO_2 $\nu3$ band head and the $\nu1 + 2\nu2$ band of N_2O. A number of these lines can be seen in the lower trace of Figure 3. The S8 and S10 lines of N_2 at 2403.6 and 2418.7 are essentially insensitive to temperature (having lower state energies of 143.2 cm^{-1} and 218.8 cm^{-1}, respectively), and their strengths give lines of convenient intensity at this resolution for quantitative analysis of tangent heights from the tropopause to about 35 km, which is the range over which refraction coupled with increasing atmospheric opacity result in nonuniform spacing of the tangent altitudes of successive scans. They thus provide an ideal means for the determination of the line-of-sight column density corresponding to each scan. Furthermore, since ray paths with tangent altitudes of between 15 and 30 km correspond to air-mass values between 10 and 1, respectively, the N_2 lines can be carefully "calibrated" by reference to spectral scans made by the instrument observing the Sun from the ground. Together with the temperature sensitive (high-J) CO_2 lines, these features provide the basis for inverse methods for the retrieval of temperature-pressure profiles. In the 30 to 40 km range numerous temperature insensitive CO_2 lines can be utilized for the determination of the line-of-sight column density; by comparison of these with the N_2 lines in the same spectra, systematic uncertainties in the molecular spectral parameters of the CO_2 bands can be minimized. In this way the range over which reliable temperature profile retrievals are possible can be extended upwards well into the mesosphere, to altitudes where the effects of photolysis of CO_2 and departure from local thermodynamic equilibrium negate many of the assumptions that can be made at lower altitudes in comparing the observed spectra with the results expected from the application of simple radiative transfer theory. Figure 4 shows an example of two retrievals to determine the pressure-temperature profiles corresponding to two of the ATMOS Spacelab 3 occultations.

At the time of writing, most of the effort in determining the atmospheric temperature, pressure, and density structure at the occultation locations has been concentrated on analyses in the 4 and 2.7 micron regions (i.e., the data obtained with filter 3), mainly for reasons related to the quality of the laboratory spectral data available in these bands. It was anticipated prior to the Spacelab 3 flight that this would be the case, and filter 3 occultations were scheduled with sufficient frequency such that temperature and pressure data derived from them could reasonably be extrapolated to the occultations utilizing other filters recorded in the near (geographical) vicinity.

The approach adopted for deriving the profiles of concentration from the data was to preselect very narrow wavelength regions in the spectra which contain analyzable features of each gas of interest, and to manipulate these "microwindows" rather than the huge spectral sets themselves. To give an indication of the quality of the data and to illustrate the remarkable power of the Fourier transform technique when used in this way, the top trace in Figure 5 shows a segment of about 500 cm^{-1} from one of the Filter 2 observations. The succeeding traces show the same data at successively higher dispersions by factors of ~10 and finally ending with a 1.0 cm^{-1} segment centered at 915 cm^{-1}, which corresponds to one of the selected microwindows for NO. Figure 6 shows the entire set of spectra in this microwindow region for this occultation and the windows depicted in both Figure 5 and Figure 6 are non-ratioed tracings showing the very different growth characteristics between the NO lines and the water vapor lines identified in the figures, and the constant absorption characteristics of solar features. Suitable microwindow regions were selected prior to the Spacelab 3 flight by the ATMOS Science Team members using the best distribution estimates available at the time for each molecule, a standard physical model of the atmosphere, and synthetic spectra generated with the aid of a 150-layer model atmosphere program. To analyze the actual flight spectra, a program was created which automatically extracts from the data the microwindows specified by the user and displays them – three successive spectra at a time – on the computer terminal screen. Starting at the highest altitude desired, the user can then activate automatic features of the program which create and iterate synthetic spectra to fit the spectral features contained in the microwindow and proceed downward (in tangent altitude) in "onion peel" fashion until a concentration profile for the species of interest as a function of altitude is derived. In general, several microwindows are used to derive separate profiles for a given species in each occultation, the individual profiles then being averaged to improve the accuracy of the final result.

Because of the magnitude of the spectral data sets which can be obtained from an instrument of this type, a large body of additional software has been written to facilitate the ATMOS data analysis activities, including programs for displaying and manipulating real and synthetic spectra, the atmospheric physical and chemical models, and the contents of the ATMOS library of molecular spectral parameters (the "ATMOS linelist"). Both on-line and off-line plotting programs and devices are also available for hardcopy graphical presentations of the data. All of the spectral examples shown in this report were reproduced directly from the output of these peripheral devices.

RESULTS

Representative examples of the ATMOS spectra illustrating the quality of the data and a few of the many interesting spectral features observed are shown in Figures 7 through 11. Figure 12 is a diagrammatic summary indicating the vertical range of detection for those species whose profiles have been extracted from the data at this stage of the analysis. Notable among the results are the detection of several trace species that had not been observed previously (namely COF_2, N_2O_5, and HNO_4), the confirmation of the presence of $ClONO_2$ in the stratosphere through the identification of 5 separate vibration-rotation bands, and the first measurement by remote sensing techniques of the principal natural halocarbon, CH_3Cl. As can be seen in Figure 12, the resolution and sensitivity of the ATMOS instrument is sufficient to allow continuous profiles of concentration for some minor gases (and at least one trace gas) to be determined extending from the upper troposphere through the stratosphere and mesosphere and, in the case of CO_2, CO, and NO well into the lower thermosphere (i.e., ~130 km). However, the derivation of the profiles in the mesosphere is complicated by the fact that the onset of photochemical thresholds for dissociation and the potential departure from thermodynamic and equilibrium conditions in these regions rander invalid many of the assumptions which can be made at lower altitudes to help in establishing the temperature and pressure environment for the species being measured. It is the task of the ATMOS Science Team over the next several months to unravel the radiative transfer, thermodynamic, photochemical, and transport processes which are occurring in these regions and improve our understanding of the physical conditions at these hitherto uncharted altitudes in our atmosphere.

FUTURE MISSIONS

While the ATMOS flight on Spacelab 3 was conducted in accordance with a comprehensive set of scientific objectives, it can also be viewed as a "proof of concept" flight which validated the instrument and experimental techniques to be used for the long range objectives of the ATMOS Investigation. ATMOS will be a core part of the Earth Observations Missions (EOM) beginning in August of 1986 and continuing for a period of at least an eleven-year solar cycle with about one flight per year. Short range objectives for these missions are expected to be planned on the basis of the current status of upper atmospheric knowledge and the flight conditions for the individual mission opportunities as they arise. The opportunity will be taken to make flights at different seasons and inclinations in order to provide the required range of observational parameters for discerning latitudinal and seasonal changes in the upper atmospheric inventory of molecular species. The data from Spacelab 3 will provide an archival record against which the results from later flights can be compared to study any long term changes in the composition of the atmosphere.

ACKNOWLEDGMENTS

The authors wish to thank the ATMOS coinvestigators and their colleagues for making available the results of work in progress which have contributed to this preliminary report. We are also grateful to Leslie Lowes, Susan Paradise, and Margaret Dietrich for their help in preparing the manuscript. We are deeply indebted to Joe Cremin, the Spacelab 3 Mission Manager, and the entire Payload Operations Control Center (POCC) cadre team for rising to the occasion when informed of the laser housing problem with ATMOS and rescheduling timelined events to move as many as possible of the ATMOS occultations to earlier times in the mission, thus preserving the primary objectives of the investigation.

The research described in this paper was performed by the Jet Propulsion Laboratory, California Institute of Technology, under contract with NASA.

REFERENCES

1. Farmer, C. B.: Infrared Measurements of Stratospheric Composition. Can. J. Chem., Vol. 52, 1974, pp. 1544-1559.

2. Farmer, C. B., Raper, O. F., and Norton, R. H.: Spectroscopic Detection and Vertical Distribution of HCl in the Troposphere and Stratosphere. Geophys. Res. Lett., Vol. 3, 1976, pp. 13-16.

3. Farmer, C. B., Raper, O. F., Robbins, B. D., Toth, R. A., and Muller, C.: Simultaneous Spectroscopic Measurements of Stratospheric Species: O_3, CH_4, CO, CO_2, N_2O, H_2O, HCl, and HF at Northern and Southern Midlatitudes. J. Geophys. Res., Vol. 85, 1980, pp. 1621-1632.

4. Morse, P. G.: Progress Report on the ATMOS Sensor: Design Description and Development Status. Paper No. 80-1914-CP, AIAA Sensor Systems for the 80's Conference, CP807, 1980.

5. Toon, G. C., Farmer, C. B., and Norton, R. H.: A Detection of Stratospheric N_2O_5 by Infrared Remote Sounding. Nature, in press.

TABLE 1. MAJOR CHARACTERISTICS OF THE ATMOS INSTRUMENT.

SPECTRAL INTERVAL COVERED	550-4800 cm^{-1} (2.1 TO 18 MICRONS)
SPECTRAL RESOLUTION	0.01 cm^{-1} UNAPODIZED (50 cm OPD)
SPECTRAL PRECISION	0.001 cm^{-1} (HE-NE REFERENCE LASER)
SPATIAL RESOLUTION	1 TO 2.5 Km
FIELD OF VIEW	1, 2, OR 4 MRAD, SELECTABLE
APERTURE	75 mm DIAMETER
SCAN TIME	1 SECOND
POINTING ACCURACY	0.1 MRAD (2-AXIS SUNTRACKER)
DETECTOR	HgCdTe (77K)
DATA RATE	15.76 MEGABITS/SECOND
MASS	250 Kgm
VOLUME	~1 STERE (INCL. ELECTRONICS)
AVERAGE POWER	350 WATTS

TABLE 2. BANDPASSES OF THE PRIMARY ATMOS FILTERS WITH THE ATMOSPHERIC SPECIES WHICH ABSORB IN EACH REGION SHOWN. PARENTHESES INDICATE A SECONDARY REGION OF ABSORPTION FOR A GIVEN MOLECULE, WHOSE PRIMARY FEATURES LIE IN THE BANDPASS OF ANOTHER FILTER.

BAND 1 600-1200 cm^{-1}	BAND 2 1100-2000 cm^{-1}	BAND 3 1580-3400 cm^{-1}	BAND 4 3100-4700 cm^{-1}
CO_2	CO_2	CO_2	CO_2
H_2O	CH_4	CO	H_2O
O_3	H_2O	CH_4	
		H_2O	
		O_3	HF
		N_2O	(HCN)
NH_3			
HNO_2	H_2O_2		
(HNO_3)	HO_2		
HNO_4		NO	
	(NO)	(NO_2)	
CCl_3F	NO_2		
CCl_2F_2	N_2O_5	HDO	
CH_3CClF_2	HNO_3	(H_2O_2)	
CH_3Cl		H_2CO	
CCl_4	HOCl		
COF_2	CF_4	HCl	
COClF		(CH_3Cl)	
ClO	SO_2		
$ClONO_2$		OCS	
		HCN	

TABLE 3. SUMMARY OF THE OCCULTATIONS OBTAINED BY ATMOS ON SPACELAB 3 LISTED BY MISSION ELAPSED TIME (MET), GEOGRAPHICAL LOCATION, AND OPTICAL FILTER NUMBER. SR DENOTES A SUNRISE OCCULTATION AND SS A SUNSET.

START TIME (MET)	OCC TYPE	OPT FIL	START LAT	START LON (E)
00/07:13	SR01	3	-50.10	118.25
00/08:08	SS01	1	36.87	277.60
00/18:52	SS02	1	36.18	117.31
00/19:27	SR02	3	-49.12	294.55
00/21:55	SS03	2	34.53	70.68
01/00:55	SS04	4	35.82	25.69
01/01:34	SR03	6	-49.10	203.09
01/02:28	SS05	1	34.80	2.26
01/07:01	SS06	3	32.90	292.66
01/08:33	SS07	2	33.65	270.20
01/10:05	SS08	1	33.73	247.39
01/15:18	SR04	4	-47.28	355.90
01/16:49	SR05	2	-47.80	333.43
01/18:21	SR06	1	-47.15	310.09
01/19:53	SR07	5	-46.97	287.07
02/01:22	SS09	3	29.95	16.84
02/02:53	SS10	4	30.28	354.13
02/04:25	SS11	3	29.00	330.65
02/05:51	SS12	2	28.65	307.61
02/07:27	SS13	3	29.65	285.23

ORIGINAL PAGE IS
OF POOR QUALITY

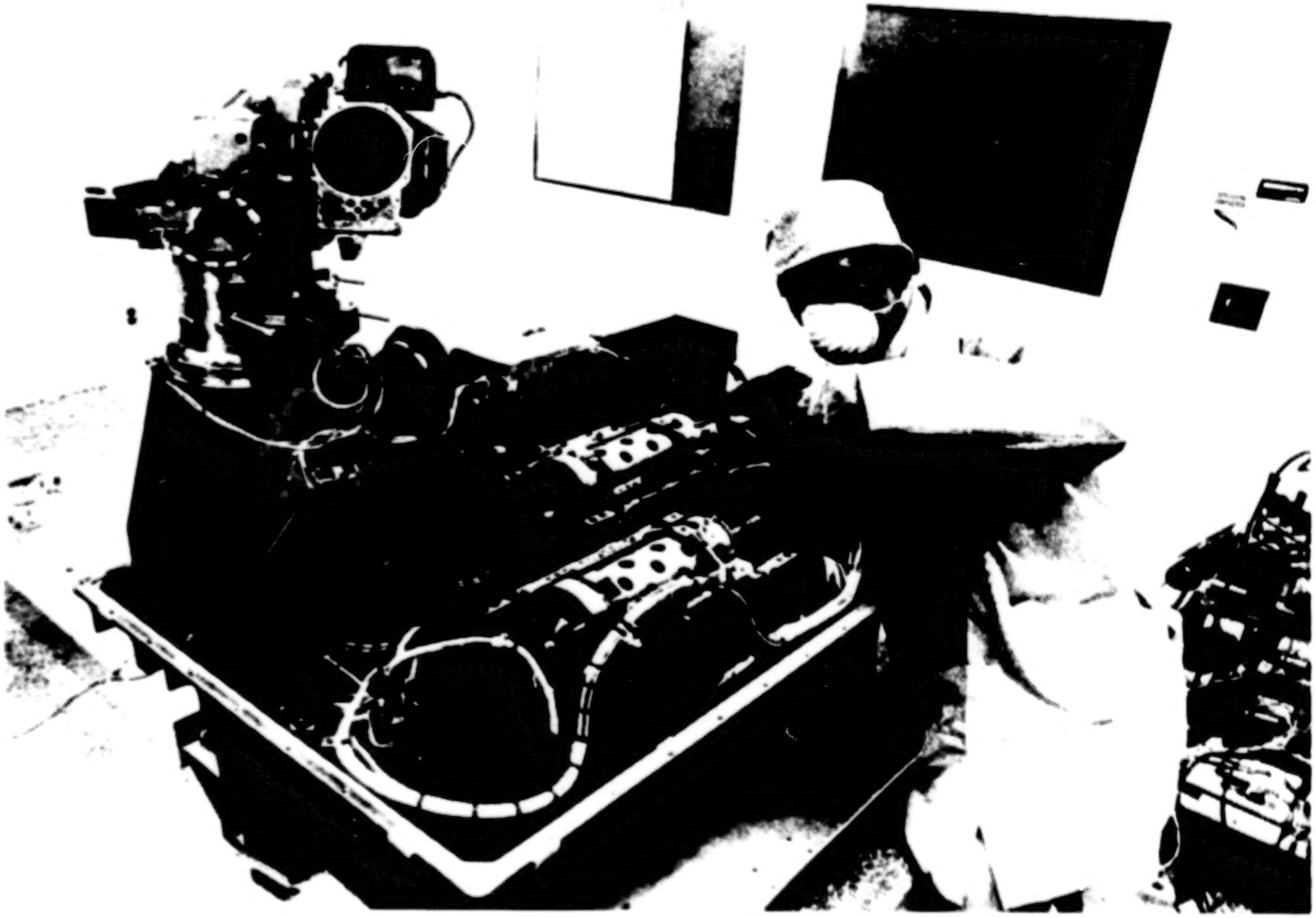

Figure 1. A cover-off photograph of the ATMOS instrument taken during the manufacturing phase at the Honeywell Electro-Optical Center. Prominent features are the two-axis suntracker seen in the upper left corner, the KBr beamsplitter and compensator and the retro mirror in the left center, and the large metal cylinders and drive motors containing the cat's-eyes.

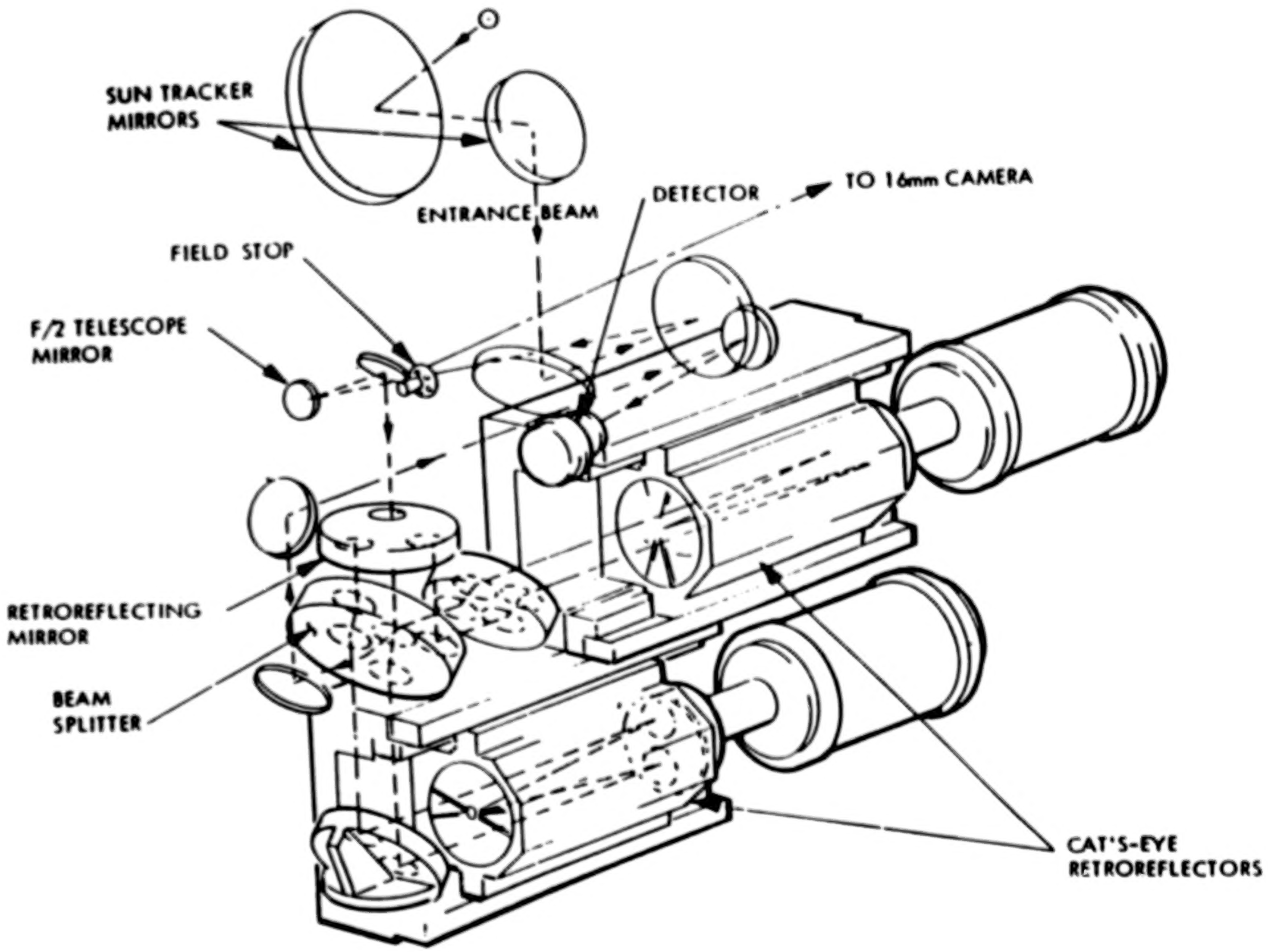

Figure 2. An optical diagram of the ATMOS sensor. Light enters through the two-axis suntracker and is focussed via a telescope on a selectable field stop which defines the instrument's FOV. Light rejected by the field stop is redirected to a frame camera which records an image of the solar disk at the end of each scan. The field stop appears in the image as a black spot superimposed on the solar disk. Once inside the interferometer, the light is divided into two beams at the beamsplitter and transmitted to the two separate cat's-eyes. After each beam traverses its arm of the inteferometer, the two are recombined at the beamsplitter and focussed on the HgCdTe detector.

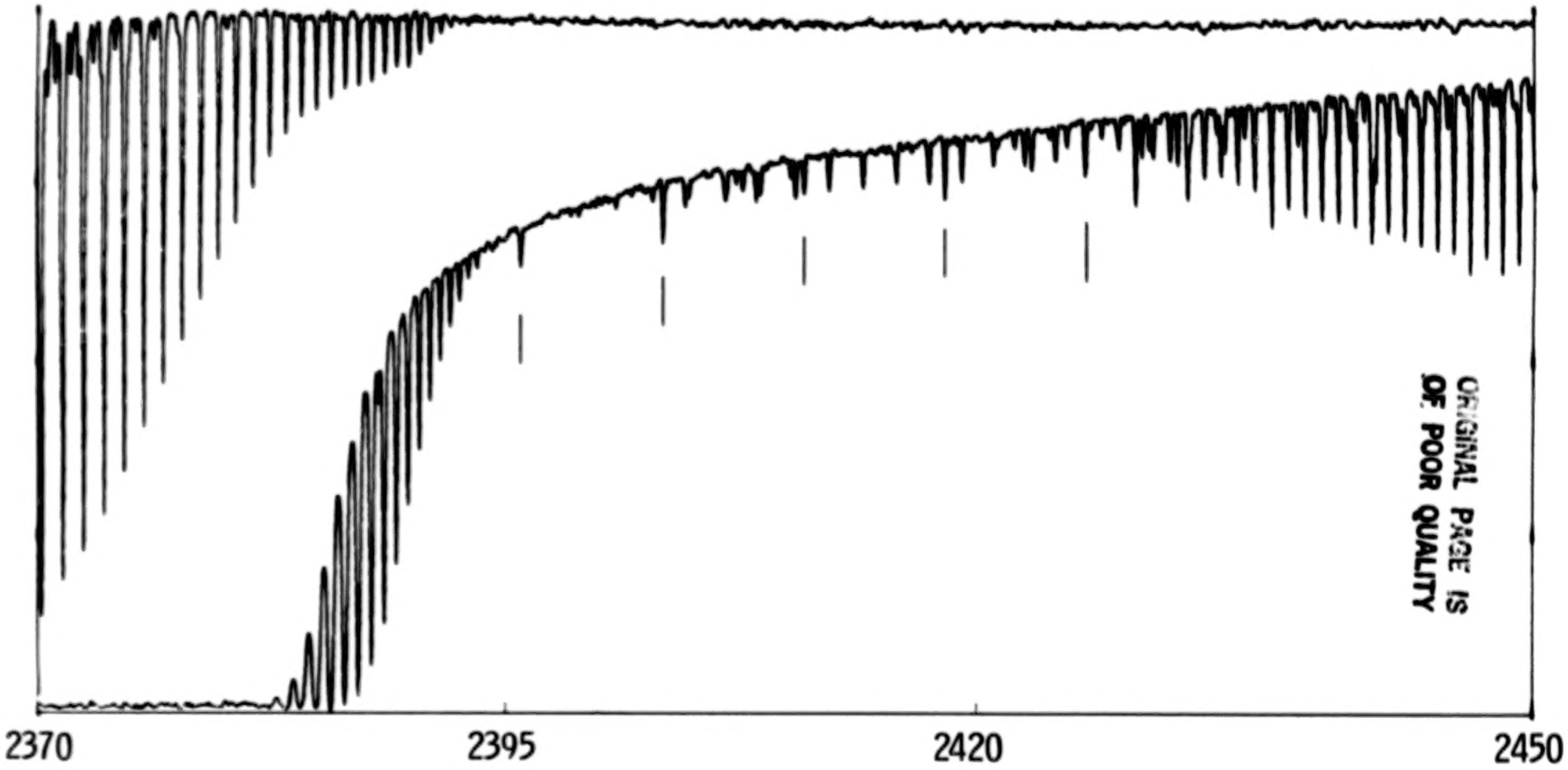

ORIGINAL PAGE IS
OF POOR QUALITY

Figure 3. Two spectral excerpts shown in the temperature-sensitive high-J region of the ν3 band of CO_2 and the pressure-induced absorption region for N_2. The depression of the continuum in the lower trace is due to the diffuse pressure-induced dipole absorption of N_2. The features marked by the vertical lines are the temperature-insensitive N_2 quadrupole lines used for density retrievals (identified from left to right as the S7 through S11 lines). Note that in the upper trace no absorption due to N_2 can be seen, even though N_2 is still the dominant gas in the region. This demonstrates the weak nature of both the dipole and quadrupole absorptions.

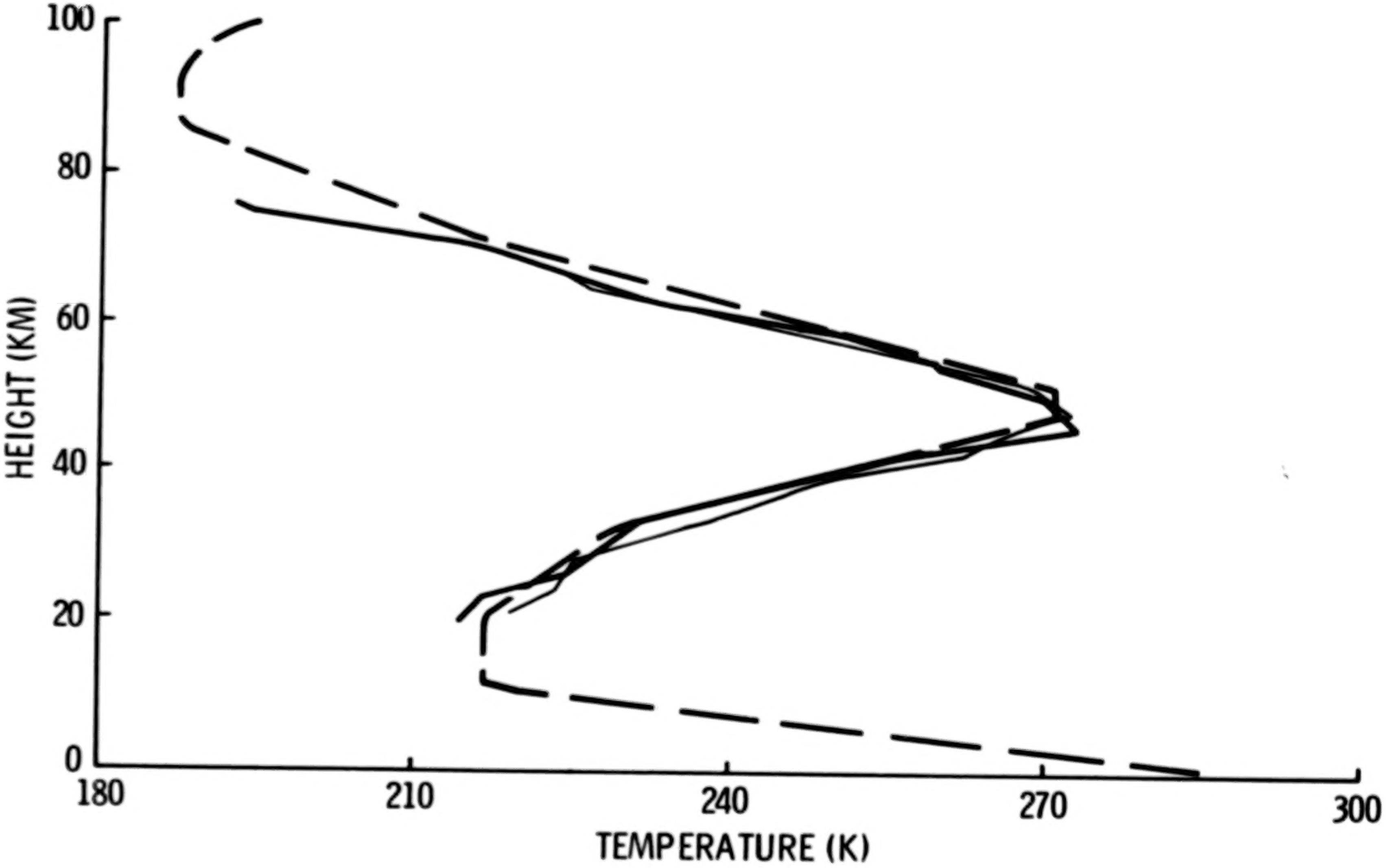

Figure 4. Two representative temperature-pressure profiles of the atmosphere derived from two ATMOS sunset observations by the method described in the text. The derived profiles (solid lines) are compared to the U.S. Standard Atmosphere for reference. Three other groups of ATMOS coinvestigators, using independent retrieval algorithms, have arrived at closely similar results for these occultations.

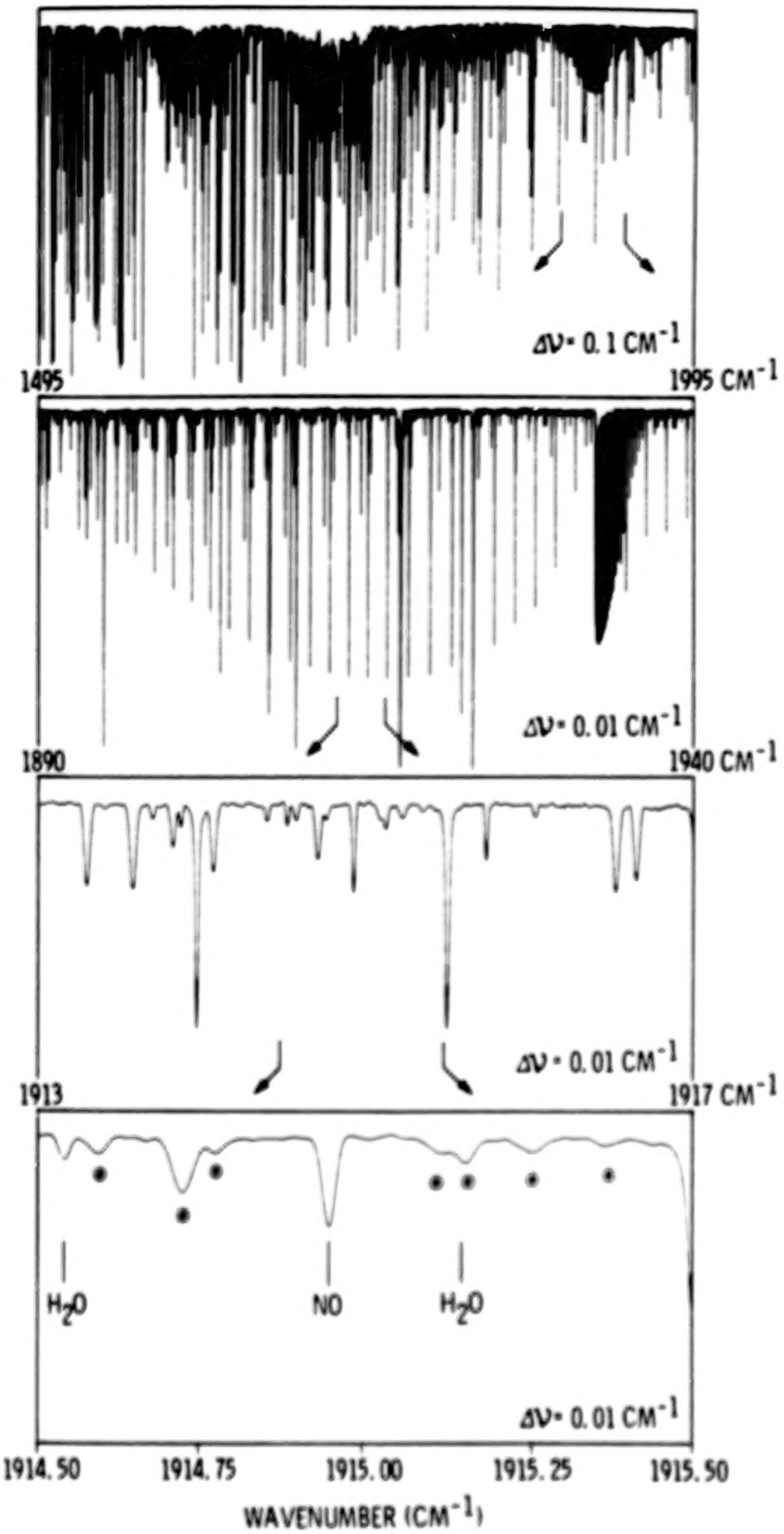

Figure 5. The top trace in this figure shows a 500 cm^{-1} region of spectrum between 1495 and 1995 cm^{-1} recorded with Filter 2. The second trace shows an expanded view of the 1900 to 1950 cm^{-1} region from the first,the third 4 cm^{-1} similar expanded from the second in the 1913 to 1917 cm^{-1} region, and finally 1 cm^{-1} expanded from the third trace centered on 1915 cm^{-1}. This one wavenumber region represents one of the selected microwindows for NO.

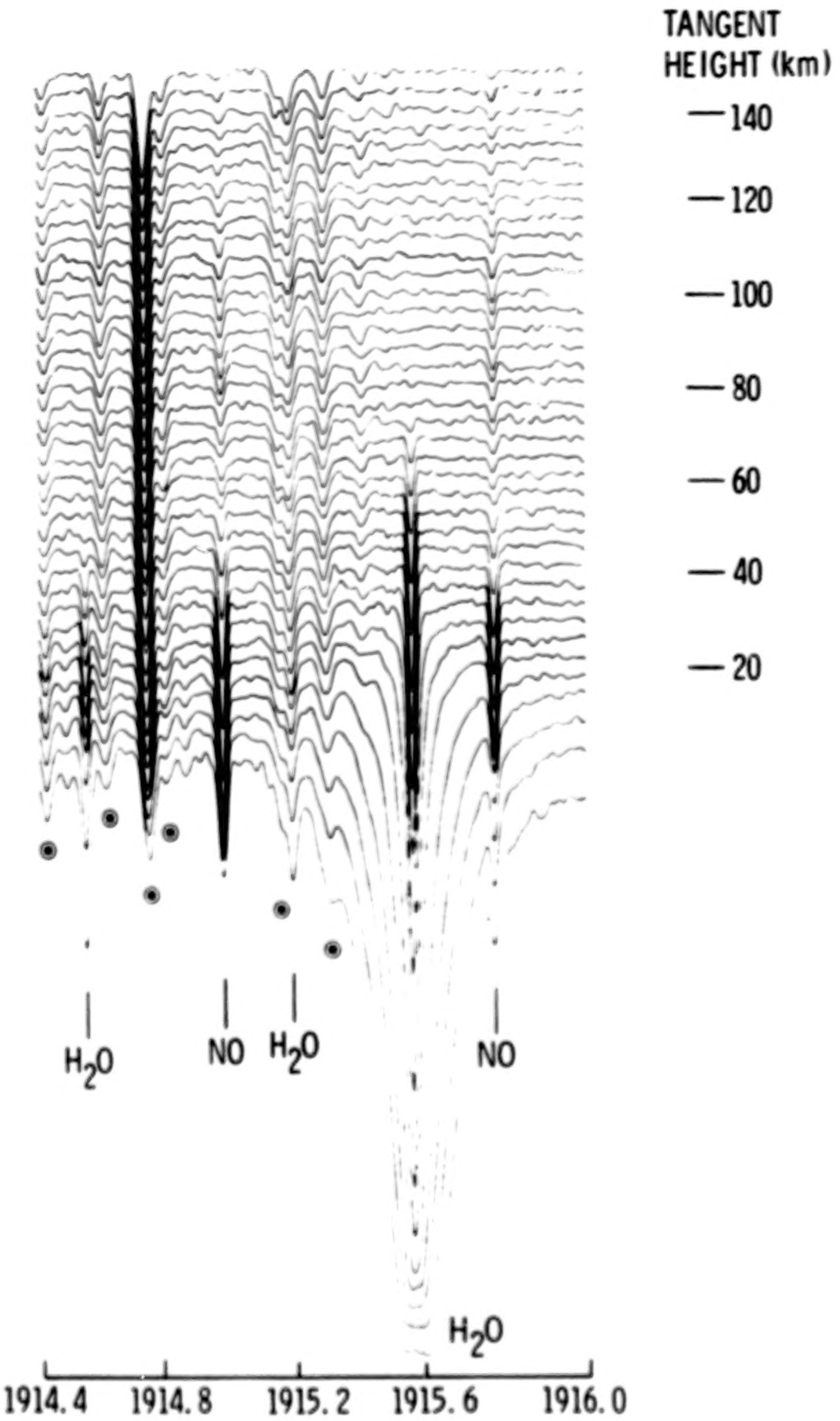

Figure 6. Shown in this figure are an entire set of 1.5 cm^{-1} spectral excerpts approximating the NO microwindow shown in Figure 5. For the purpose of clarity, the spectra have been overlaid as a function of altitude. Several other solar lines and lines of telluric origin are also present in the window, in addition to the two lines for NO at 1914.99 and 1915.77 cm^{-1}.

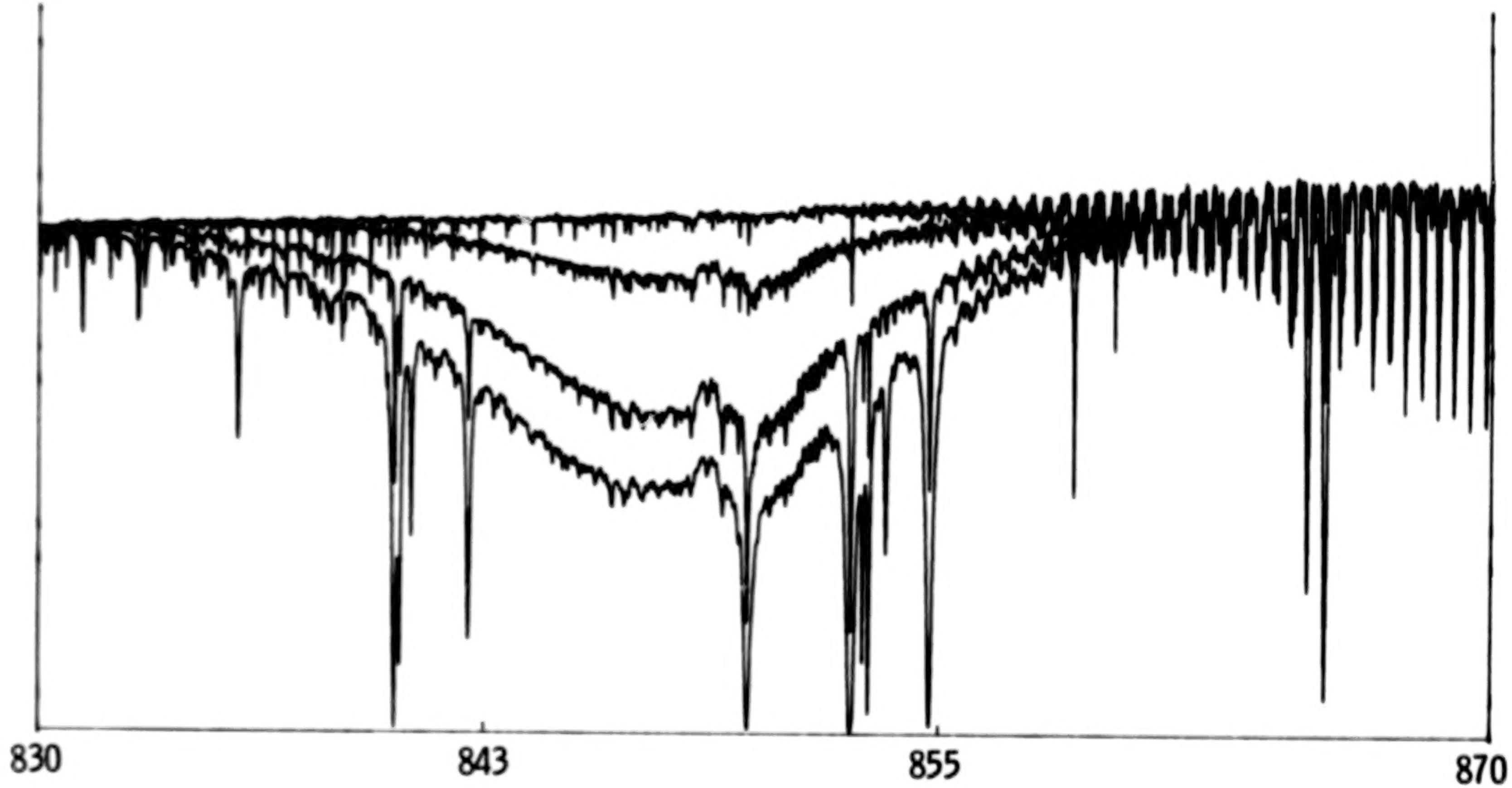

Figure 7. Portions of four spectra in the region of 830 to 870 cm^{-1} showing a large unresolved spectral feature of Freon 11 (F-11) in the lower three traces. The lowermost trace in the figure was made at 5 km altitude, and demonstrates that useful tropospheric information can be acquired using this remote sensing technique when atmospheric conditions are favorable. Such conditions prevailed for many of the ATMOS occultations.

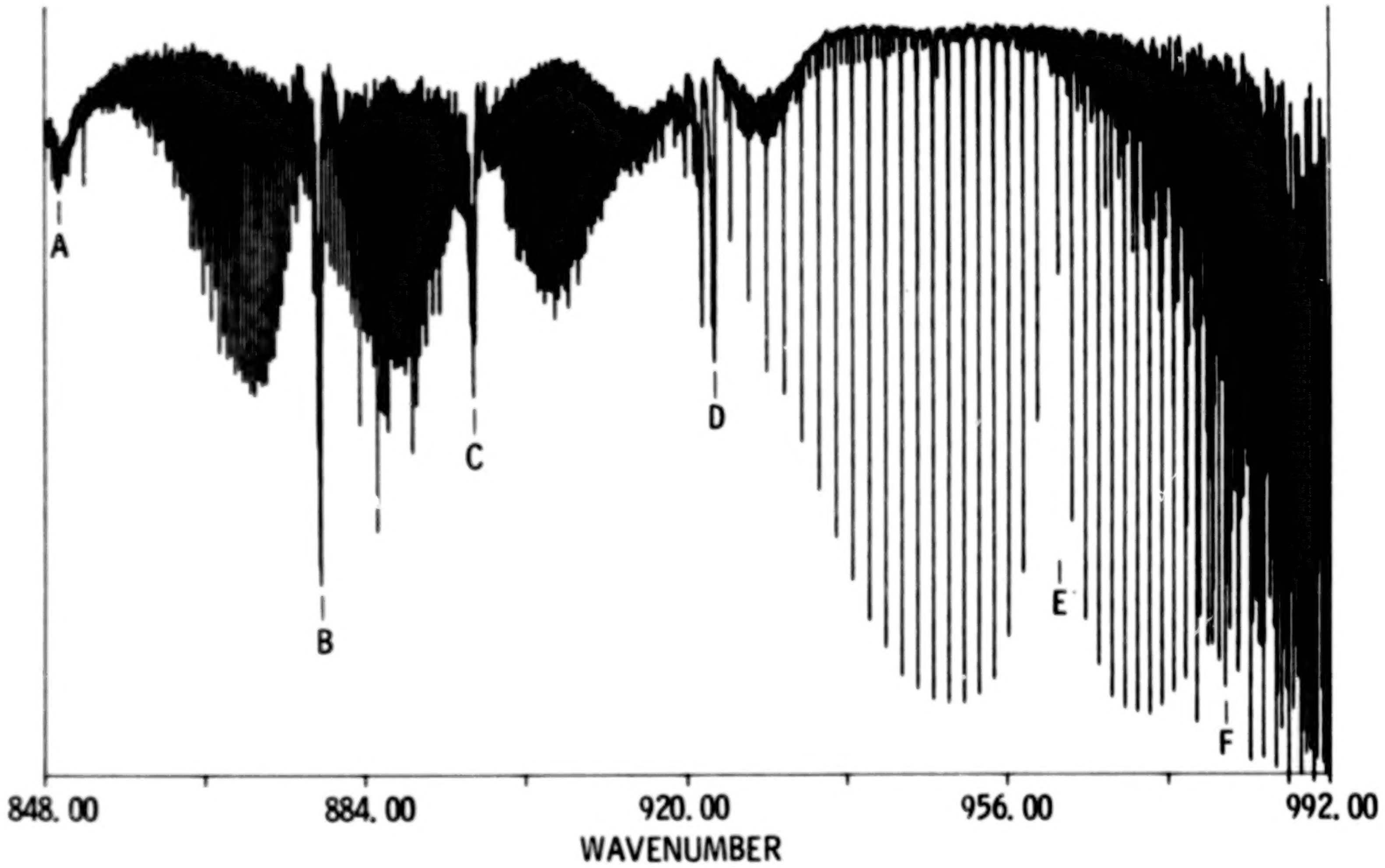

Figure 8. This figure demonstrates that dramatic asthetic effects in nature are not limited to the visible regions but rather occur throughout the electromagnetic spectrum. The feature marked by A in the figure is that of F-11 shown in Figure 6. The features whose Q branches are marked by B and C, respectively, are two transitions of HNO_3; the region between B and C is characterized by perturbations and blendings between the R branch lines of one feature and the P branch lines of the other. D marks the Q-branch of an F-12 absorption feature whose rotational lines are so densely packed they are completely unresolved at the ATMOS resolution, resulting in P and R branches which appear only as depressions in the continuum. E marks the center of a CO_2 absorption characterized by deep, relatively widely spaced rotational lines. Beyond F, tightly packed, seemingly chaotic lines of ozone begin to dominate the spectrum.

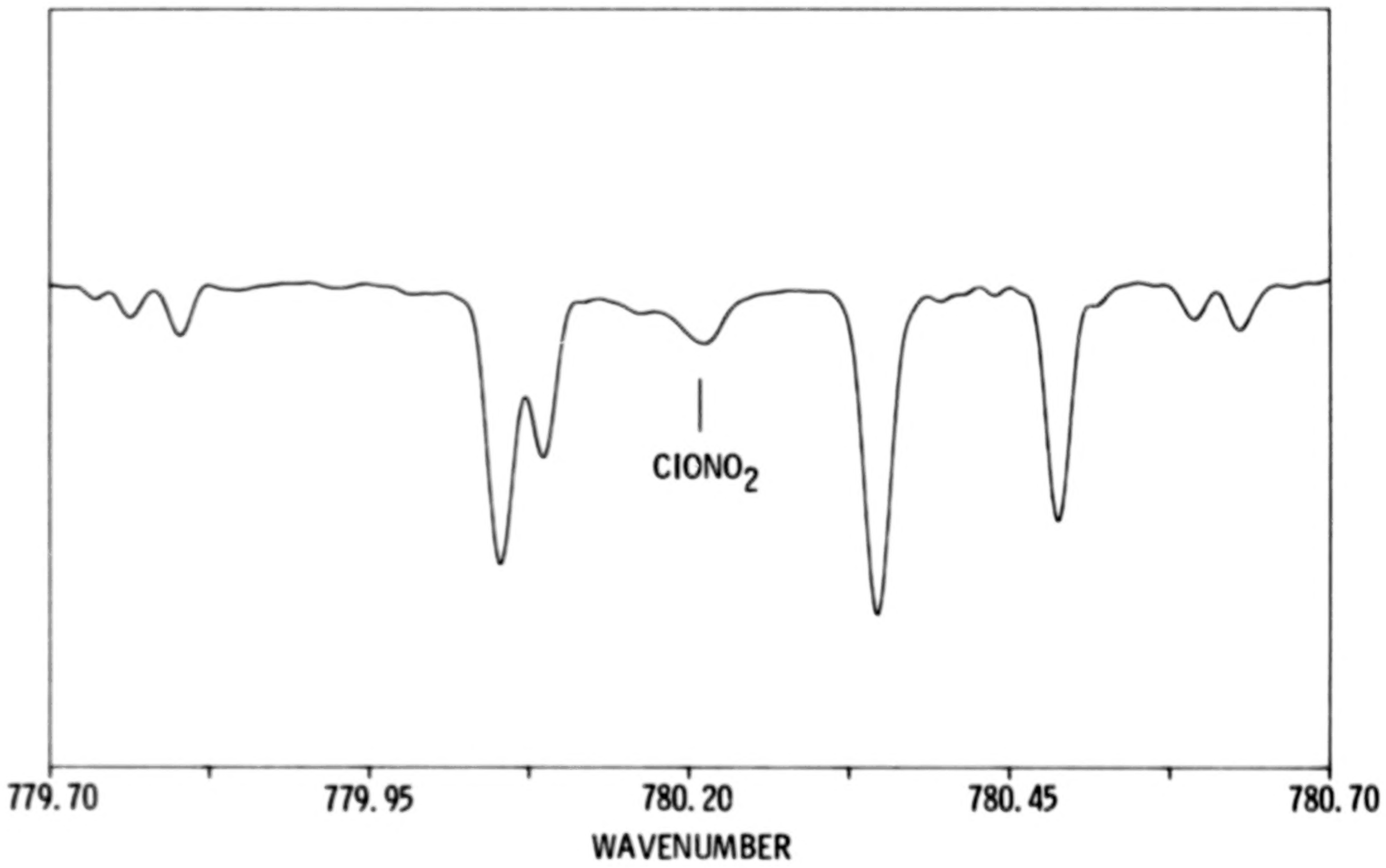

Figure 9. A portion of an ATMOS spectrum showing the feature of $ClONO_2$ at 780.22 cm^{-1}. This figure illustrates one of the marked advantages of acquiring spectra in large sets such as that returned from Spacelab 3. The spectrum shown, as well as the others used in retrieving the $ClONO_2$ profile, are zonal averages of several spectra from occultations in the same latitudinal regions using the same optical filter andcovering the same altitude range. Such averaging can enhance the signal-to-noise characteristics, causing otherwise marginal features to stand out in the data and permit profiles of concentration to be obtained at only minimum costs in spatial resolution.

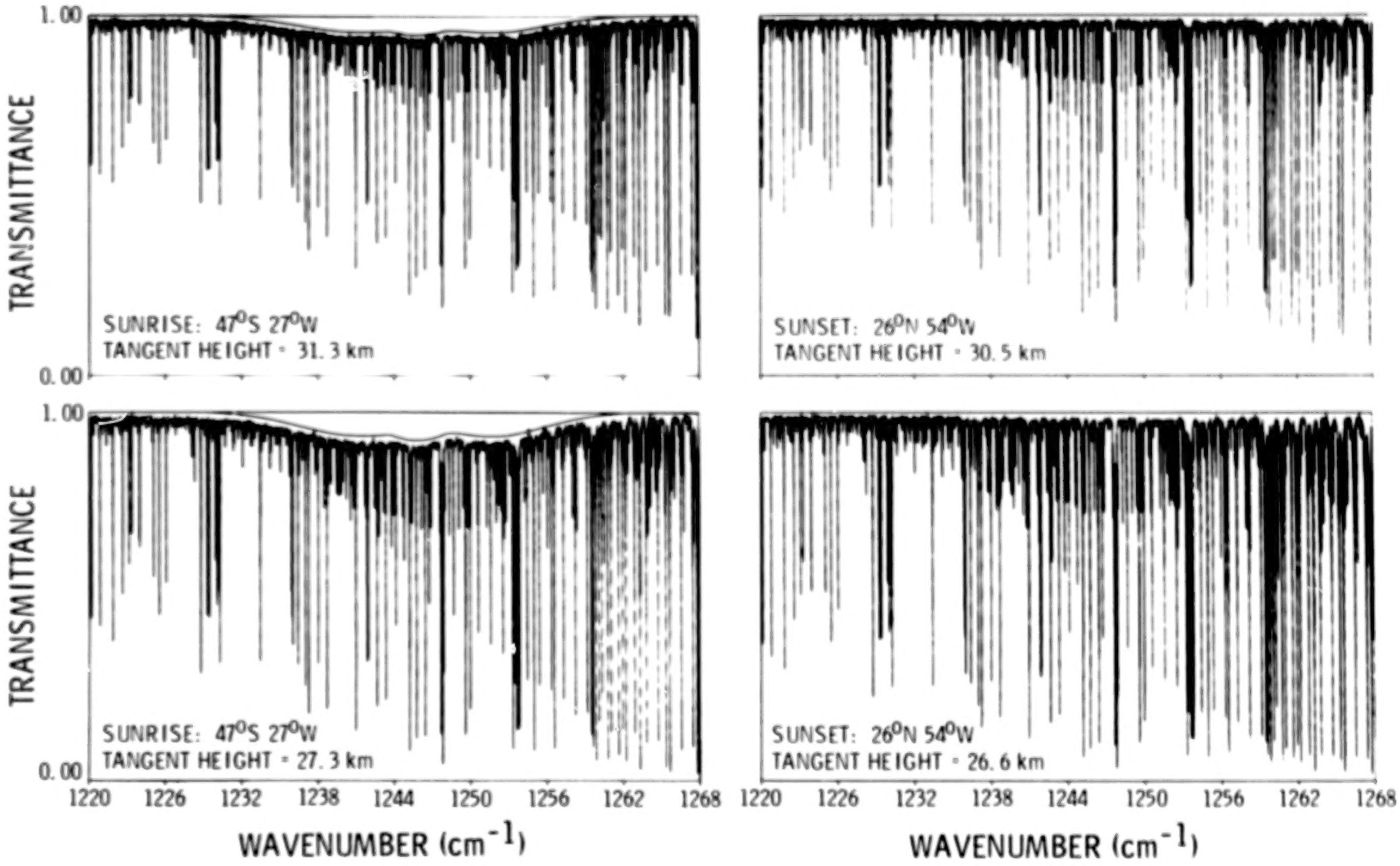

Figure 10. This figure, reprinted from Toon, C. G., et al., (1986) shows the $\nu 12$ band of N_2O_5 in the ATMOS spectra. The solid lines above the sunrise spectra in the figure represent a spectroscopic model of the $\nu 12$ feature, the lines of which are completely unresolved at the ATMOS resolution. The figure clearly illustrates the sunrise-sunset difference in the N_2O_5 profiles as predicted by the photochemical models.

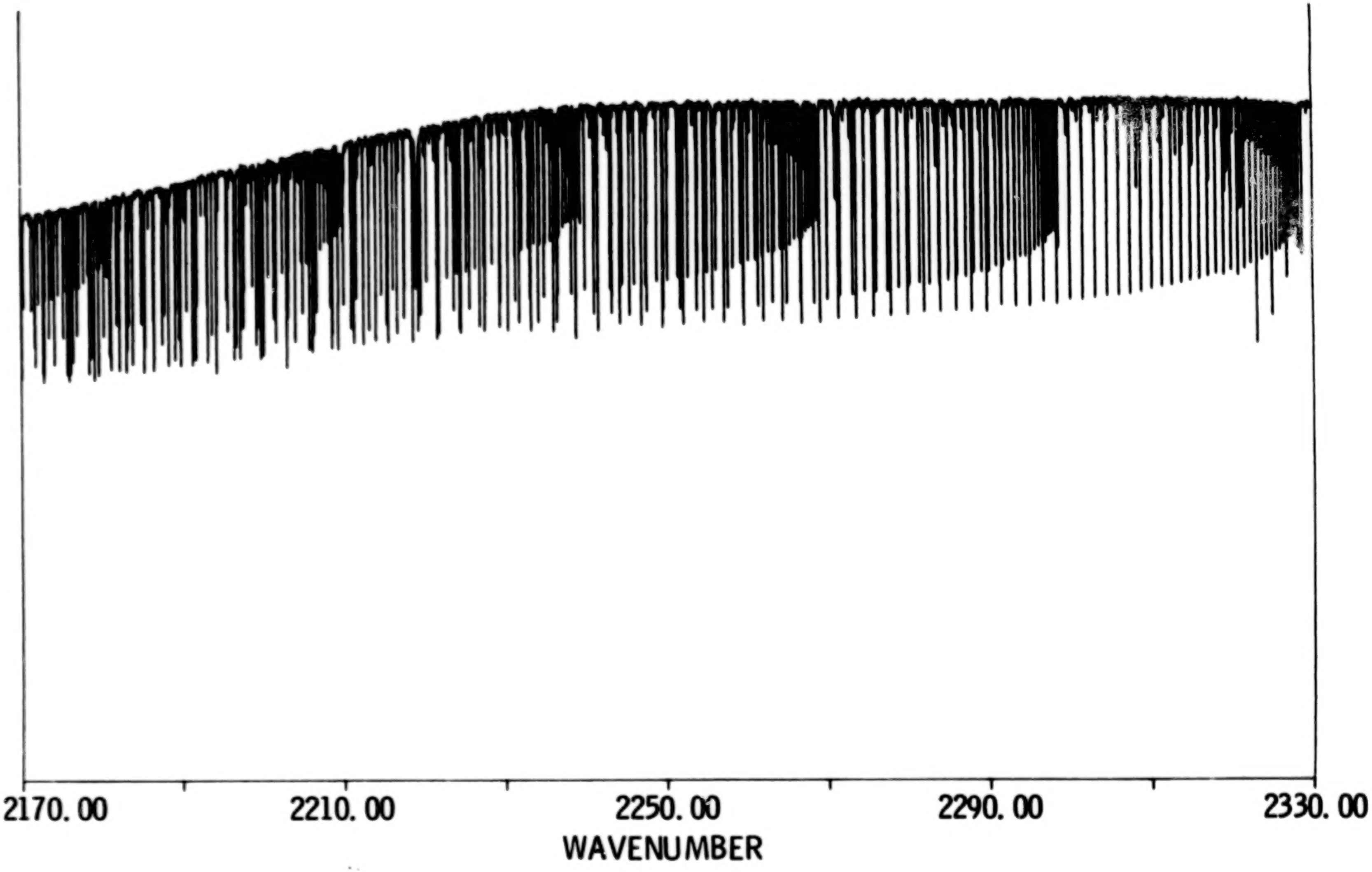

Figure 11. The outstanding features in this figure are the band heads resulting from transitions between the higher vibrational states of CO with $\nu = 1$. These features are not seen in telluric spectra, but are solar in nature and occur in the photosphere of the Sun as a result of the high temperatures present in the region. Note the classical folding back of the lines in the band heads at the higher values of J.

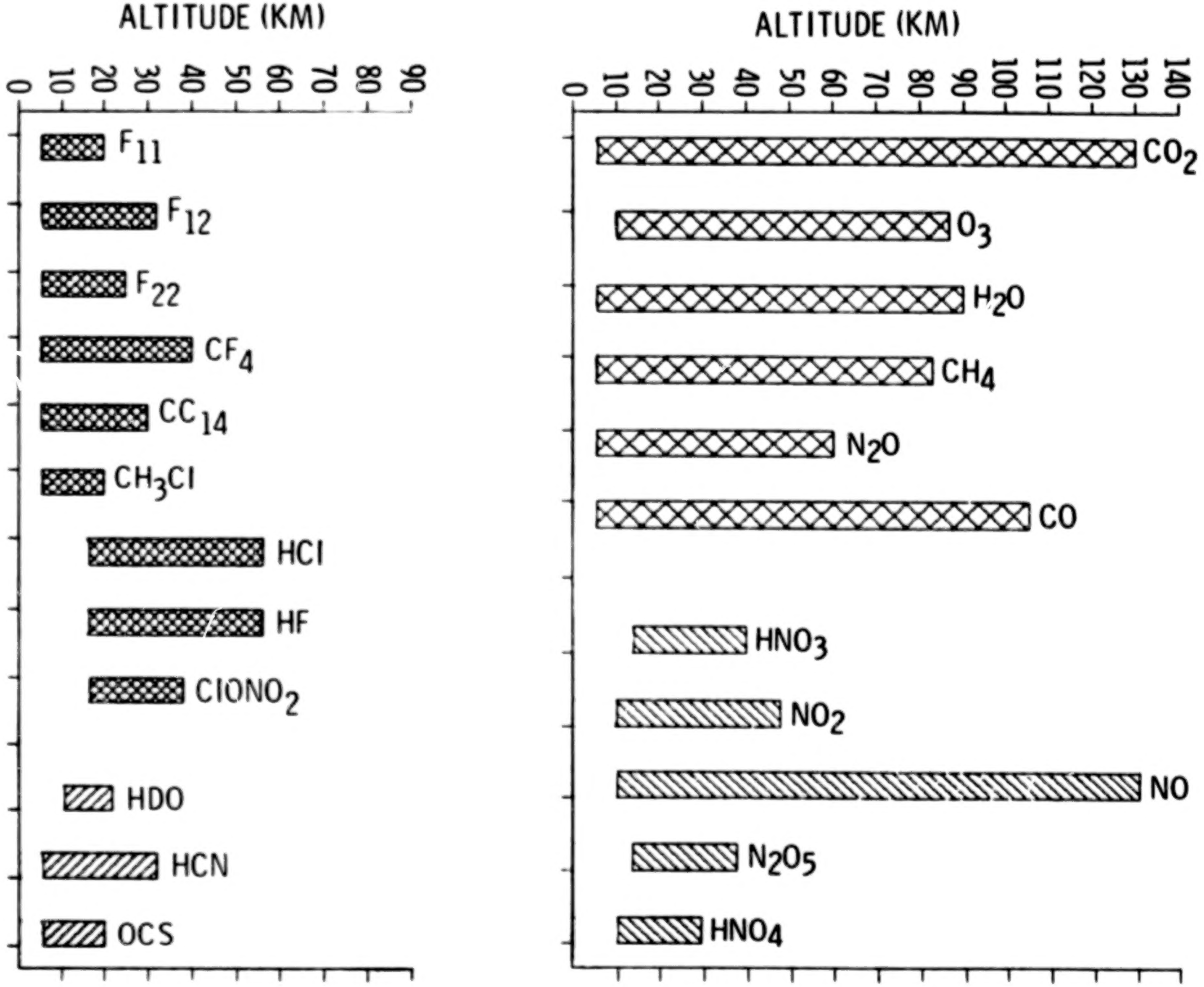

Figure 12. Diagrammatic summary of species detected in the ATMOS spectra, separated into the minor gases and chemical families of trace species; the bars indicate the altitude ranges over which profiles of concentration can be retrieved from the data.

N87-22110

ORIGINAL PAGE IS
OF POOR QUALITY

AURORAL IMAGES FROM SPACE 3

Thomas J. Hallinan
Geophysical Institute University of Alaska, Fairbanks, AK 99775-0800

Don Lind
NASA Johnson Space Center, Houston, TX

The Spacelab 3 space shuttle mission of April 29-May 6, 1985, provided an excellent opportunity to survey the Aurora Australis from near-Earth orbit. The orbital inclination and Beta angle were such that the orbit penetrated the average auroral oval in darkness. (Some aspects of the observations were compromised by scattering of moonlight from the clouds below.) Since this was a manned mission, it was practical to use imaging detectors that required aiming and high-bandwidth recording. We obtained 274 color photographs of the aurora and approximately 5 hr of black and white video recordings. The data cover 22 separate passes from seven days. On several occasions the Orbiter passed above the auroral forms. By using the orbital motion to provide the parallax, we have been able to view both the color photographs and the video recordings stereoscopically.

The data provide the first views from outside the atmosphere of thin horizontal layers of "enhanced aurora" (Fig. 1). The layers, once thought to be rare, were recorded on two out of three passes. This first observation of enhanced aurora from space eliminates concerns that the ground-based observations might have been an optical illusion caused by atmospheric refraction. Also, for the first time, vertically thin layers were observed in diffuse aurora. This is a measurement that is possible only from space ideally in nearth-Earth orbit.

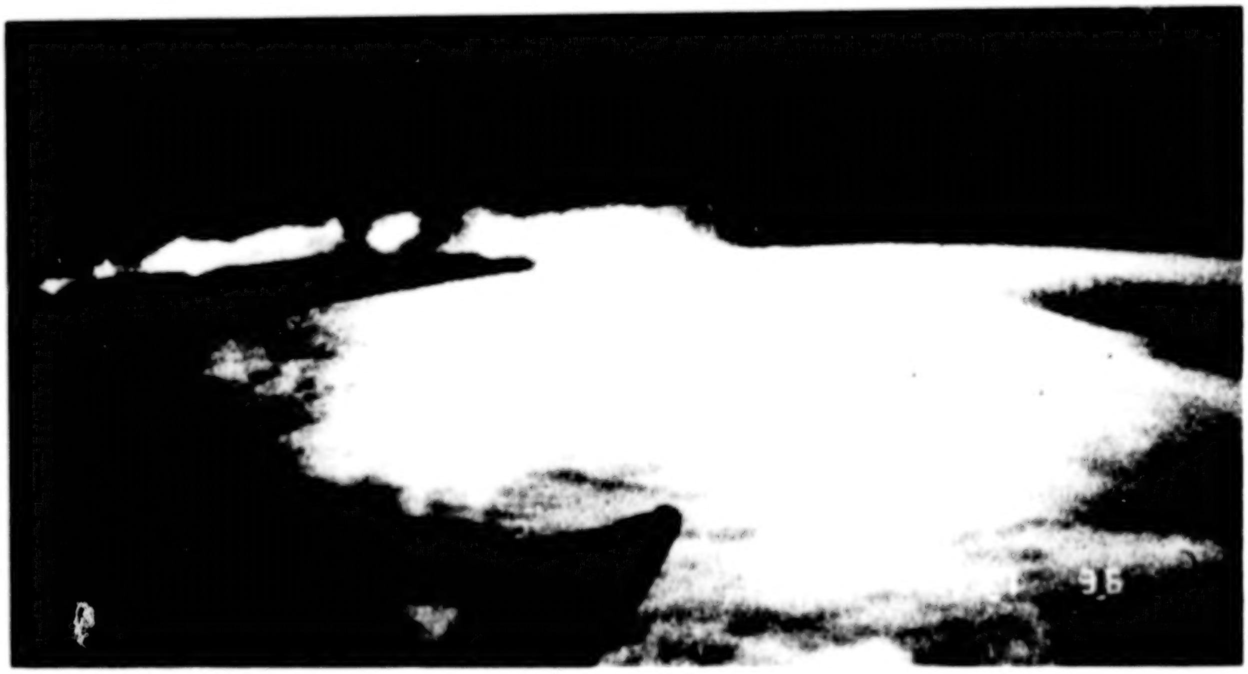

Figure 1. The Aurora Australis seen from Spacelab 3. The thin uniform band parallel to the Earth's curved line is an edge-on view of the airglow layer at ~95 km altitude. A rayed auroral arc is seen just above the airglow layer and bending equatorward to pass under Challenger seen in the foreground. The rays in the arc have vertical extents of ~60 to 200 km, but there is a very thin (<2 km) band of enhanced auroral emission running through the aurora near the base of the rays. In the color photographs this is easily distinguished from the airglow layer beneath it.

N87-22111

IONS (ANURADHA): IONIZATION STATES OF LOW ENERGY COSMIC RAYS

S. Biswas, R. Chakraborti, R. Cowsik, N. Durgaprasad, P. J. Kajarekar,
R. K. Singh, M. N. Vahia, and J. S. Yadav
Tata Institute of Fundamental Research, Bombay 400005, India

N. Dutt, J. N. Goswami, D. Lal, H. S. Mazumdar, and D. V. Subhedar
Physical Research Laboratory, Ahmedabad 380009, India

M. K. Padmanabhan
ISRO Satellite Centre, Bangalore 560 017, India

ABSTRACT

IONS (ANURADHA) (1), the experimental payload designed specifically to determine the ionization states, flux, composition, energy spectra and arrival directions of low energy (10 to 100 MeV/amu) anomalous cosmic ray ions of helium to iron in near-Earth space, had a highly successful flight and operation in Spacelab-3 mission. The experiment combines the accuracy of a highly sensitive CR-39 nuclear track detector with active components included in the payload to achieve the experimental objectives. Post-flight analysis of detector calibration pieces placed within the payload indicated no measurable changes in detector response due to its exposure in spacelab environment. Nuclear tracks produced by α-particles, oxygen group and Fe ions in low energy anomalous cosmic rays have been identified. It is calculated that the main detector has recorded high quality events of about 10,000 α-particles and similar number of oxygen group and heavier ions of low energy cosmic rays.

DISCUSSION

The low energy (5 to 100 MeV/amu) anomalous component of cosmic rays discovered in the early seventies has been studied in great detail over the last decade. Comprehensive information on composition, energy spectra, radial gradient and time variation of the anomalous cosmic rays (ACR) in the interplanetary medium have been obtained using instruments on board the IMP, Pioneer and Voyager spacecrafts [2,3]. The near-Earth component of the ACR was first identified in a Skylab experiment [4]; this has, however, not been studied in detail. The spacelab mission offered a unique opportunity for such a study and the Indian experiment "IONS" (or Anuradha) on board Spacelab-3 was primarily intended for this purpose.

Several suggestions have so far been made about the origin of the anomalous cosmic rays [5]. The major distinguishing features of these models are the predicted charge states of ACR and its radial gradient and time variation. Further, the models of Fisk et al. [5] and Fowler et al. [5] suggest production of the anomalous component within the solar system, whereas Biswas et al. [5] suggested a stellar origin for these low energy particles. Extensive studies of the interplanetary ACR component [3,6] have yielded valuable information on their radial gradient and time variation for the period 1973-1984 which indicate an extra solar system origin for these particles. However, no direct measurement of ionization states of ACR is presently available. The primary objective of the IONS experiment was to obtain this crucial information for the near-Earth component of ACR. Additional information on composition and intensity of this component will also be obtained from this experiment. In this report we present the salient features of the IONS payload, the experimental approach, flight operations and performance of the instrument and also preliminary results on anomalous particle fluences based on analysis of auxiliary detector elements placed inside the payload. The processing and analysis of the main detector stacks are currently in progress.

Instrument and Experimental Approach

The IONS payload flown in Spacelab-3 is shown in Figure 1. It is 48 cm in diameter, has a height of 53 cm, and weighs 45 kg. The payload houses two detector modules, the main detector module (bottom stack) being about 40 cm in diameter and 4.5 cm thick. It is composed of 174 sheets, mostly of CR-39, All Diglycol Carbonate (DOP), nuclear track detectors along with a few sheets of Lexan Polycarbonate each of thickness of 250 μm. On the top of this stack, separated by a gap of 500 μm is a single sheet of CR-39 of thickness 250 μm which is held rigidly to the instrument frame by a stainless steel ring structure. During experiment operation the main stack is rotated using a high resolution stepper motor and a gear assembly in discrete steps of 40 sec of arc once every 10 sec., so as to make one complete revolution in 90 hrs. The movement of the stack is monitored by a 15 bit absolute shaft encoder coupled to it. A thin 75 μm aluminum alloy dome acts as the top enclosure of the sealed payload which is maintained at a pressure of 0.1 atmosphere during its space exposure. The payload was mounted directly on a cold plate fixed to a specially prepared experimental support structure to maintain the instrument temperature at a nominal value of 25°-40°C. The IONS instrument is mounted on spacelab with its Z-axis tilted by 25 deg so as to reduce the Earth shadow on the viewing cone during the flight. The gravity gradient stabilized attitude of the shuttle provided very favourable celestial viewing of IONS with a viewing cone of about 110 deg. Inside the payload a temperature sensor was placed close to the detector module to monitor its temperature during the duration of the exposure. Small samples of test CR-39 detector elements, irradiated to energetic heavy ion beams from accelerators, are also included in the payload for monitoring any possible changes in the detector response due to its exposure in pressure and temperature conditions within the payload. The entire operation of the IONS instrument was controlled by onboard computer and the relevant data regarding instrument functions (e.g. BMT, stack movement, temperature, etc.) are telemetered down link once every second for record and monitoring by experimenters. The instrument operation could be initiated and interrupted, if required, by crew interface or via ground command.

The experimental approach for obtaining ionization states of ACR involves several major steps. The atomic number, energy and arrival direction of each energetic particle incident on the detector modules are determined from an analysis of the track records left by the ions in the two CR-39 detector stacks. The revelation of latent tracks for optical viewing in these detectors is achieved by etching the detector sheets in a 6.25 N NaOH solution at 70°C for suitable durations of several hours. Track parameters like length, diameter, and residual range are measured and used in conjunction with energetic accelerator ion calibration data, for the same CR-39 detector samples to determine atomic number and energy of the tracks forming ions using standard procedures [7]. The arrival time information will be obtained from the angular displacement of each track in the bottom detector stack compared to its location on the top CR-39 sheet. This information will be coupled with space shuttle's trajectory data. Thus, the arrival direction of each ion in space is determined. The threshold magnetic rigidities (i.e., momentum/charge) of ions are then derived from the computation of charged particle trajectories in geomagnetic field for the known latitude, longitude, altitude, and arrival directions. By combining the data of magnetic rigidities with momentum of ions measured in the main detector, the ionization states of the heavy ions are determined.

Flight Performance

The Spacelab-3 with IONS on board was successfully launched on day 119 at 16:02:18 GMT from Kennedy Space Center, Florida. Several factors contributed to make the Spacelab-3 mission ideally suited for the study of low energy cosmic rays. First, the flight period was characterized by very low level of solar activity free from any flare events. This is illustrated in Figure 2, where we show two specific parameters characterizing the solar activity during the flight period and also their levels during solar minimum and maximum. Second, the instrument operation period was also free from any significant geomagnetic activity. Further, recent studies of anomalous cosmic rays in interplanetary space [3] have indicated that during the last solar magnetic field reversal in 1980-81 the intensity of ACR was at its minimum value, and the ACR flux for 10 MeV/N oxygen ions showed a steady rise from its 1981 value by a factor of about 10 during early 1985.

The IONS instrument was activated on the third day into the mission via ground command. Following the activation, a snag was noticed as the payload was not responding to some of the commands sent by the onboard computer. The cause was finally traced to a faulty cable connecting the computer to the remote acquisition unit through which commands were fed to the instrument. The fault was rectified by the crew following procedures drawn up by NASA ground support personnel, and IONS started operation from day 123, 12:44:08 GMT. The performance of the instrument was excellent during the entire period of operation of 64 hours, which was 71 percent of the planned operation duration. The thermal control system also worked perfectly and the temperature within the instrument was maintained in the range of 22°-40°C during the entire period of operation. We show in Figures 3(a) a sample of encoder readings showing the actual and commanded positions of the rotating bottom detector stack versus GMT. Each encoder step corresponds to about 40 sec of arc once every 10 sec. An offset of 10 divisions in commanded position is introduced for the sake of clarity. Figure 3(b) shows the instrument temperature for the same time slice, monitored by the temperature sensor kept inside the payload close to the detector module. Following the successful completion of the mission, the IONS payload was examined and all sub-systems including the two detector modules were found to be in perfect condition, with no sign of any physical stress or strain suffered during its space exposure.

Detector Response and Preliminary Results

The CR-39 (DOP) (Allyl Diglycol Carbonate) plastic used in the present experiment is an extremely sensitive nuclear track detector, and was specially manufactured by Pershore Co. (UK) adopting a long curing cycle and doping treatment with 1 percent dioctyl phthalate. Prior to the flight, sample pieces of this CR-39 (DOP) plastics were exposed to accelerator beams of low energy, upto 10 MeV/N α-particles, ^{12}C, ^{16}O, ^{20,22}Ne, ^{28}Si, ^{52}Cr, ^{58}Ni and high energy, 1.88 GeV/N ^{56}Fe and 200 MeV/N ^{238}U ions to determine its nuclear track recording characteristics. The results obtained from measurement of track parameters in these calibration samples are shown in Figure 4, where we plot the ratio of track etch rate to bulk etch rate, V_t/V_b, as a function of energy loss, dE/dx, for different ions. It can be seen that in the low energy loss region the etch rate ratio is a linear function of energy loss, whereas at higher energy loss region it can be approximated as a power function of energy loss. A least square fit to the data yielded the following response function for the detector over the energy loss region of interest.

$$V_t/V_b = 1 + 5.67 \times 10^{-4} (dE/dx) + 1.22 \times 10^{-10} (dE/Dx)^{2.7} \qquad (1)$$

The results of the calibration studies also showed that the CR-39 (DOP) detector used in this experiment efficiently records tracks of all energetic particles with $Z/\beta \geqslant 8$, where Z is the nuclear charge and βc is the velocity of the ions and it should be possible to achieve a charge resolution of 0.2 charge unit. Sample pieces of CR-39 exposed to alpha particles, neon, iron, and uranium beams were also kept inside the IONS payload to monitor any change in its response function due to the ambient pressure (0.1 atm) and temperature (25-40°C) within the payload. Post flight analysis of these calibration pieces indicates that response characteristics of these CR-39 detectors remained the same during its exposure in spacelab environment. This can be clearly visualized from Figure 4 where we have plotted the track etch ratio for neon and uranium ion tracks obtained from measurements made in calibration detector pieces flown in the payload. Hence the response curve [equation (1)] is adequate for identifying atomic number of the track forming nuclei in the IONS detector stack.

For zero time marking of the fixed top detector and the moving bottom detector module, the detector assembly was exposed to a narrow collimated beam of 50 MeV alpha particles in the Variable Energy Cyclotron, Calcutta. We first completed the analysis of a set of small area auxiliary detectors of CR-39 flown in the IONS detector module in order to obtain initial information on the types of low energy cosmic ray particles and their fluxes. These CR-39 samples were etched in 6.25 N NaOH at 70°C for 6 hrs. Figure 5 shows photomicrographs of some samples of tracks produced by low energy cosmic ray alpha particles, oxygen group ($Z = 6\text{-}10$) and Fe nuclei recorded during the flight. The sharp definition of the tracks is clearly evident in these photomicrographs. Based on the measured number of tracks of different ions the fluxes of low energy cosmic ray alpha particles, oxygen group and iron nuclei were determined. The time-average differential flux of alpha particles at 8 MeV/N is obtained as $(1.3 \pm 0.23) \times 10^{-5}$ particles $\mathrm{cm^{-2}\ sr^{-1}\ sec^{-1}\ (MeV/N)^{-1}}$. Assuming that the energy spectrum of alpha particles is flat in the region 8-50 MeV/N as in interplanetary space. We expect to obtain about 10,000 times annotated alpha particles in 8-40 MeV/N energy interval in the main detector. The time-average differential flux of oxygen group particles at 17 MeV/N is obtained as $(1.7 \pm 0.5) \times 10^{-6}$ particles $\mathrm{cm^{-2}\ sr^{-1}\ sec^{-1}\ (MeV/N)^{-1}}$. This value is in the range expected from the interplanetary flux measured in early 1985 in Voyager-2, which is about 1×10^{-6} p/(cm^2.sr.sec.MeV/N) at 15 MeV/N, considering the radial gradient of ACR and the transmission factor in the geomagnetic field. At 26 MeV/N, the time average oxygen group flux is obtained as $(5.8 \pm 2.0) \times 10^{-8}$ p/(cm^2.sr.sec.MeV/N). This shows the steady recovery of ACR since solar maximum in 1980-81, and by April-May 1985 it has increased by a large factor and has reached a level, being only 5-10 times lower from maximum flux of 1974 level. The expected number of anomalous cosmic rays of the oxygen group in the IONS detector in the energy interval of 15-30 MeV/N with arrival time information is estimated to be about 8000 events. The expected number of other components of anomalous cosmic rays can be estimated from the above number of events. In addition to anomalous cosmic rays we expect to obtain more than 10,000 galactic cosmic ray nuclei of oxygen and heavier nuclei in the IONS detector. Several important types of measurements such as isotopic composition of iron group nuclei can be carried out with high degree of reliability. The top CR-39 sheet and several upper sheets of the bottom stack of the main detector of the IONS have been processed and the measurements and analysis of tracks in these are currently in progress. The results obtained from these data will provide us the information on the ionization states and also on the composition, intensity and energy spectra of low energy anomalous cosmic rays in near-Earth space which will provide new clues to the origin of this enigmatic component of energetic particles in our solar system.

REFERENCES AND NOTES

1. "ANURADHA" is the sanskrit name of the star δ-Scorpii or a part of the constallation Scorpius. As cosmic rays originate from some type of stars in some phase of their evolution, the stellar name is given to the experiment.

2. Hovestadt, D., Vollmer, O., Gloeckler, G., and Fan, C. Y.: Phys. Rev. Lett., Vol. 31, 1973, p. 65. Garcia-Munoz, M., Mason, G. M., and Simpson, J. A.: Ap. J. (Letters), Vol. 182, 1973, p. L81: Apl. J., Vol. 202, 1975, p. 265. McDonald, F. B., Teegarden, B. J., Trainor, J. H., and Webber, W. R.: Ap. J., Vol. 187, 1974, p. L105. Klecker, B., Hovestadt, D., Gloeckler, G., and Fan, C. Y.: Ap. J., Vol. 212, 1977, p. 290, and references therein.

3. Cummings, A. C., Stone, E. C., and Webber, W. R.: Proc. 19th Int. Cosmic Ray Conf., Vol. 5, 1985, p. 163. Mewaldt, R. E. and Stone, E. C.: Ibid, Vol. 5, 1985, p. 167. Mason, G. A., Klecker, B., Galvin, A. B., Hovestadt, D., and Ipavich, F. M.: Ibid, Vol. 5, 1985, p. 168.
Webber, W. R., Cummings, A. C., and Stone, E. C.: Ibid, Vol. 5, 1985, p. 172. McKibben, R. B., Pyle, K. R., and Simpson, J. A.: Ibid, Vol. 5, 1985, p. 198.

4. Biswas, S., Durgaprasad, N., Nevatia, J., Venkatavaradan, V. S., Goswami, J. N., Jayanthi, U. B., Lal, D., and Mattoo, S. K.: Astrophys. Sp. Sci., Vol. 35, 1975, p. 337.

5. Biswas, S. and Durgaprasad, N.: Sp. Sci. Rev., Vol. 25, 1980, p. 285. Biswas, S., Durgaprasad, N., and Trivedi, S.: Proc. Ind. Acad. Sci., Vol. 90, 1981, p. 337. Fisk, L. A., Kozlovosky, B., and Ramaty, R.: Ap. J. (Letters), Vol. 190, 1974, p. L35. Fowler, P. H., Redfern, R. M., and Swordy, S. P.: Nature, Vol. 279, 1979, p. 622.

6, McKibben, R. B., Pyle, K. R., and Simpson, J. A.: Ap. J., Vol. 227, 1979, p. L147. Hovestadt, D., Klecker, B., Gloeckler, G., Ipavich, F. M., Fan, C. Y., and Fisk, L. A.: Proc. 16th Int. Cosmic Ray Conf., Kyoto, Vol. 3, 1979, p. 255.

7. Fleischer, R. L., Price, P. B., and Walker, R. M.: Nuclear Tracks in Solids: Principles and Applications. Univ. of California Press, 1975. Henke, R. P., and Benton, E. V.: Nuclear Inst. and Methods, Vol. 97, 1971, p. 483.

ACKNOWLEDGMENTS

We are extremely thankful to Indian Space Research Organization Satellite Centre (ISAC), Bangalore, for their excellent support in conducting various integrations and testings of IONS; to Bhabha Atomic Research Centre (BARC), Bombay, for fabrication of the flight and flight spare IONS structure; Laser Laboratory of BARC for providing laser operations; and Variable Energy Cyclotron Centre (VEC), Calcutta, for providing support for the alpha beam exposures. We are grateful to NASA for providing us with the Spacelab-3 flight aboard the Shuttle Challenger and the Mission Specialists, Dr. Don Lind and Dr. Norman Thaggard, for inflight replacement of a faulty cable, as well as NASA ground engineers for ground support and help in reactivation of IONS during the flight.

ORIGINAL PAGE IS
OF POOR QUALITY

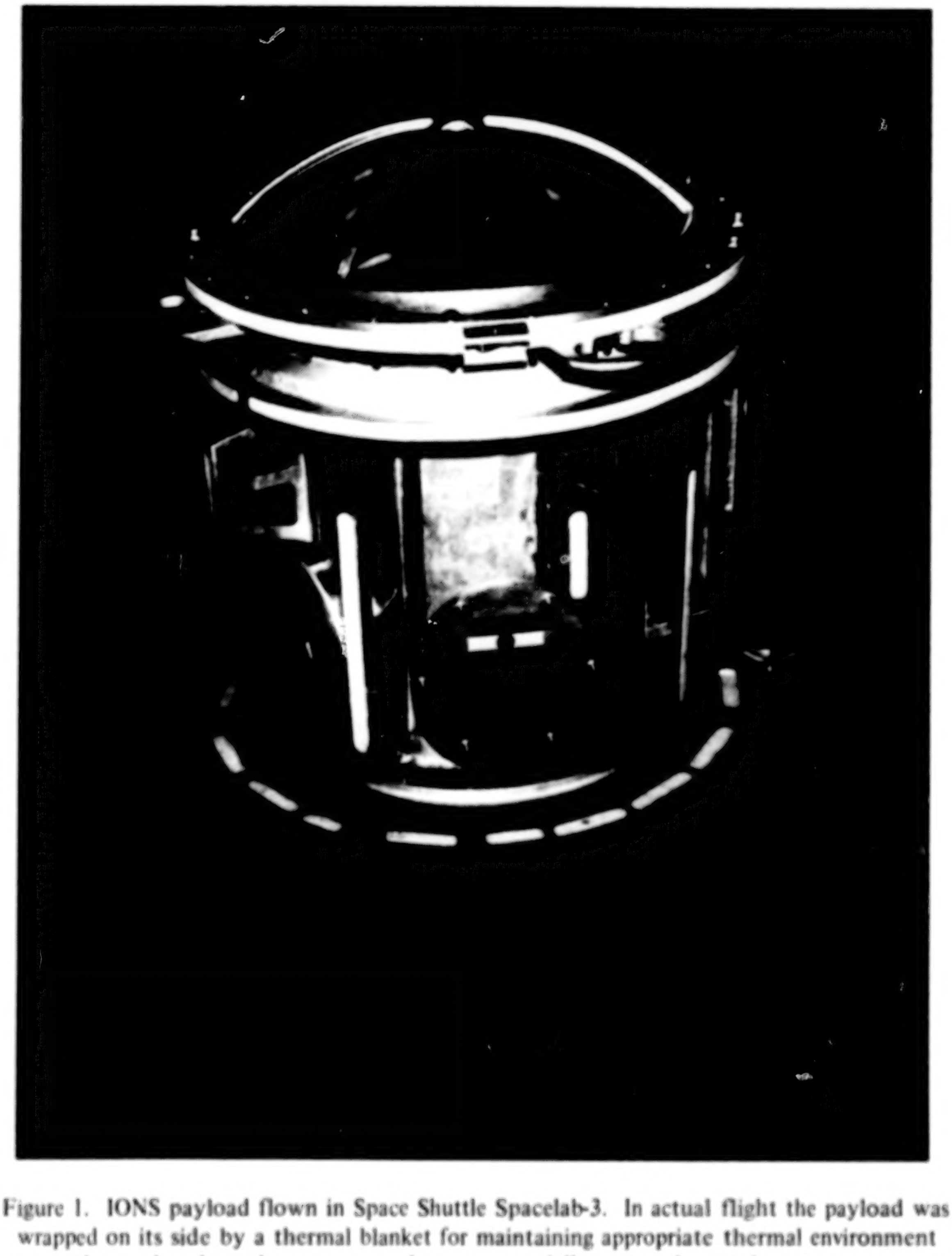

Figure 1. IONS payload flown in Space Shuttle Spacelab-3. In actual flight the payload was wrapped on its side by a thermal blanket for maintaining appropriate thermal environment and was placed on the open cargo bay on a specially mounted experiment support structure. The pressure inside the payload was maintained at 0.1 atm. during the flight with the help of pressure senitive venting valves fixed on the wall of the payload.

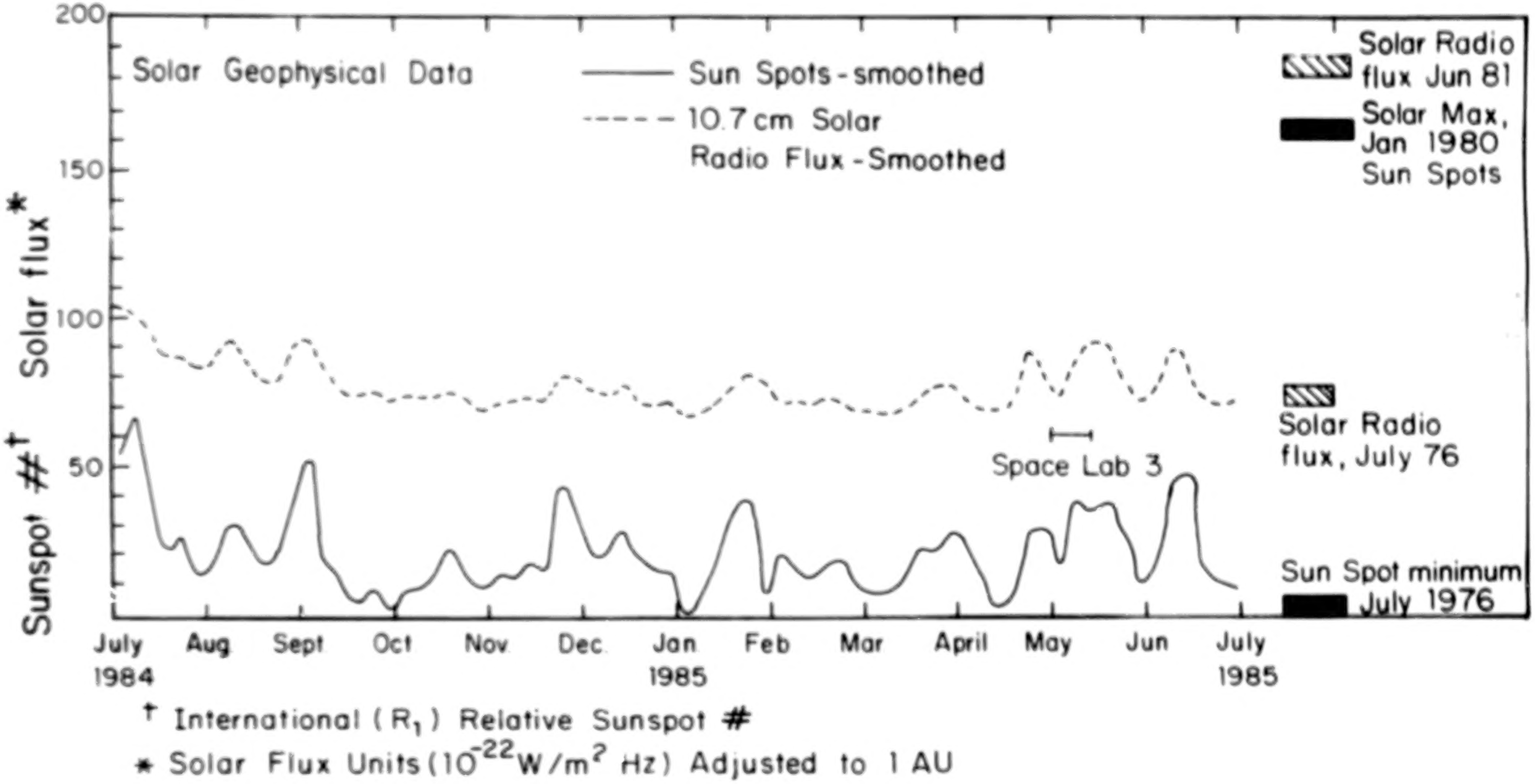

Figure 2. The level of solar activity during and close to the Spacelab-3 flight period is shown in terms of the two indices of solar activity: the sunspot number and 10.7 cm solar radio flux. The level of solar activity during the last solar minimum (1976) and maximum (1981) are also shown. The low level of solar activity during Spacelab-3 flight duration is clearly seen. The data are from solar geophysical data No. 491, Part I, July 1985 (Publ. American Geophysical Union).

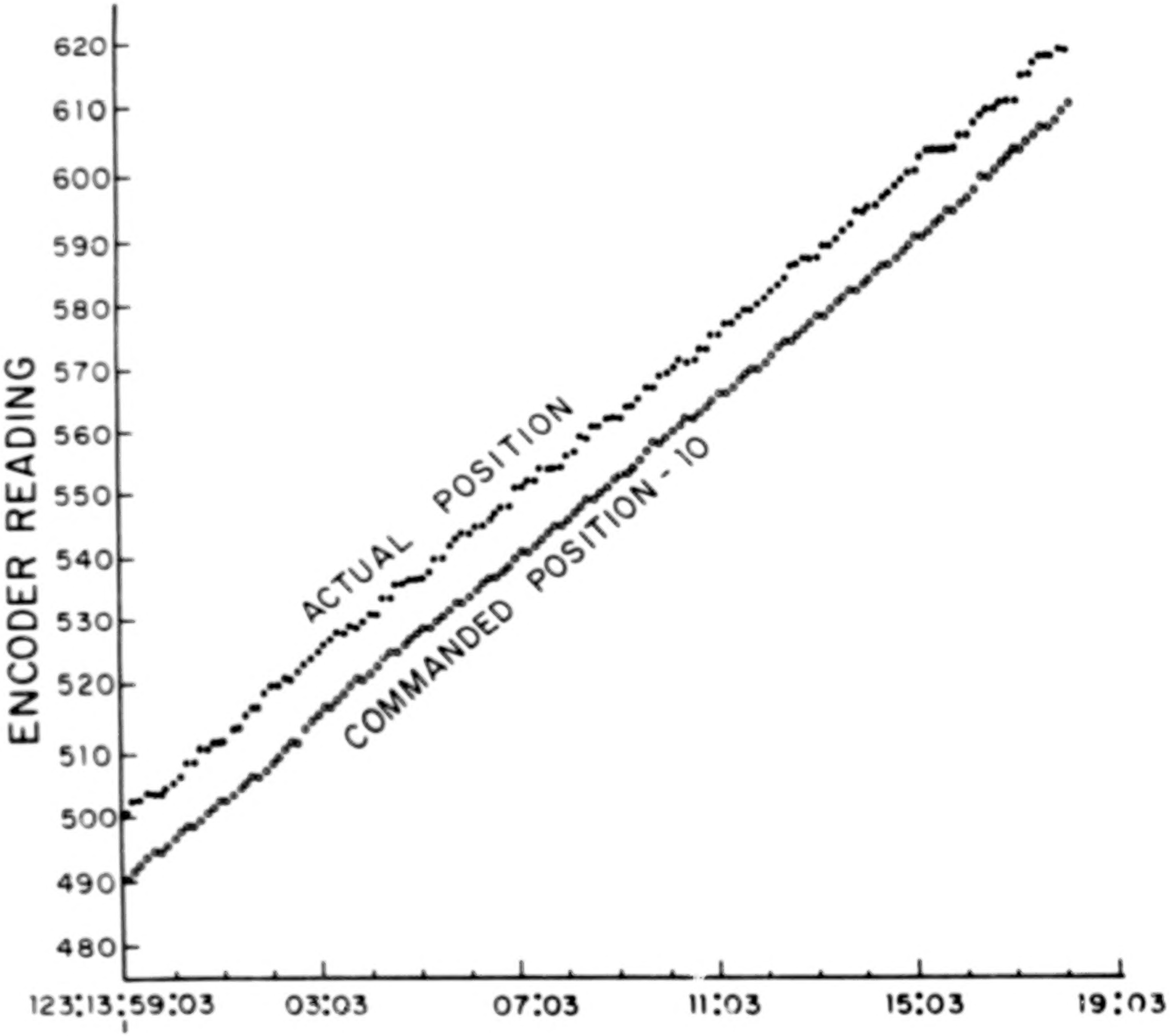

Figure 3(a). Sample data of encoder readings indicating positions of the rotating bottom detector stack following about an hour of instrument activation. Both commanded and actual encoder readings are shown as a function of GMT (day-hr-min-sec). An offset of 10 steps has been introduced in the commanded position for the sake of clarity. Each step-rotation is equivalent to 40 arc sec and takes place every 10 secs.

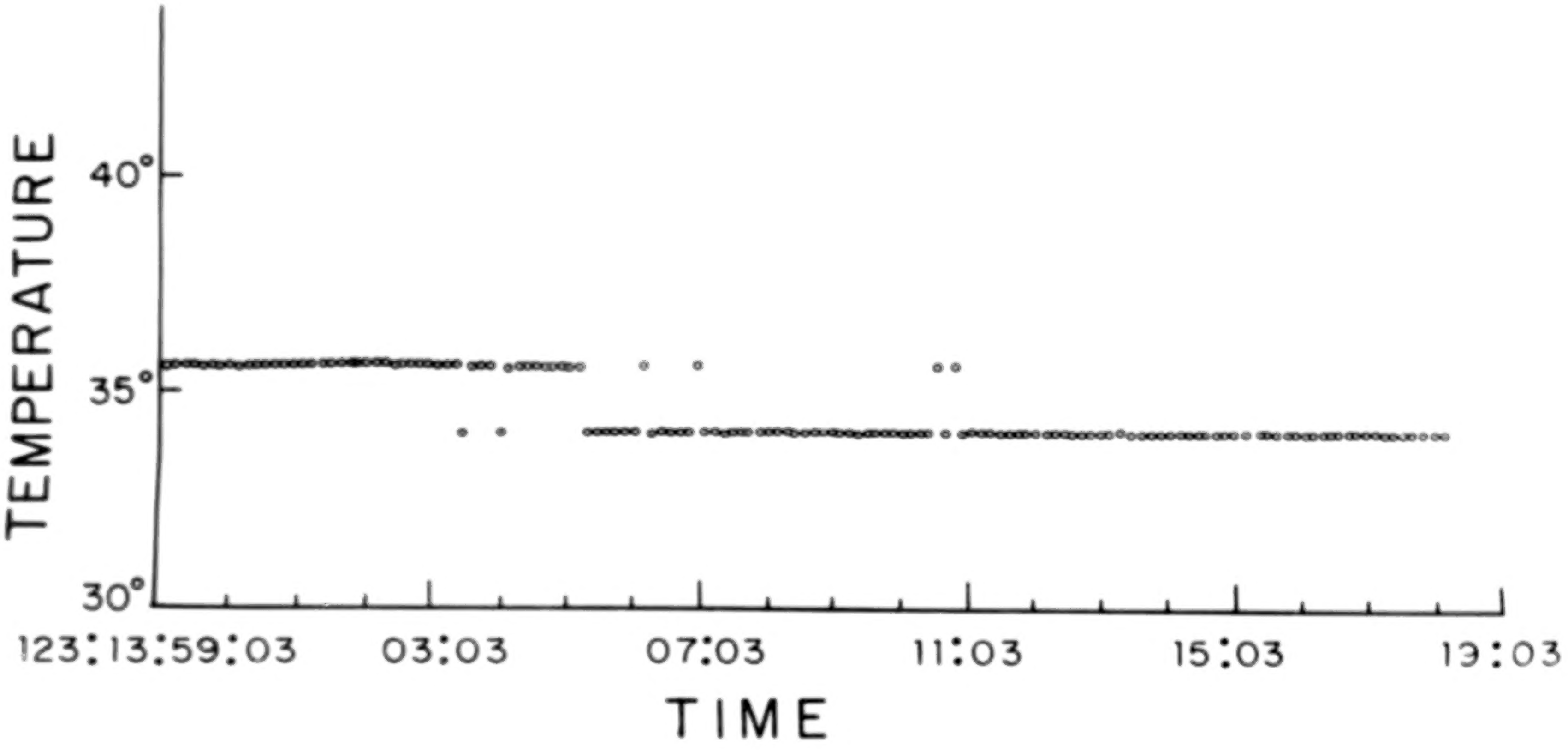

Figure 3(b). Temperature of the instrument, as monitored by a sensor placed close to the bottom detector stack, for the same time-slice as in Figure 3(a).

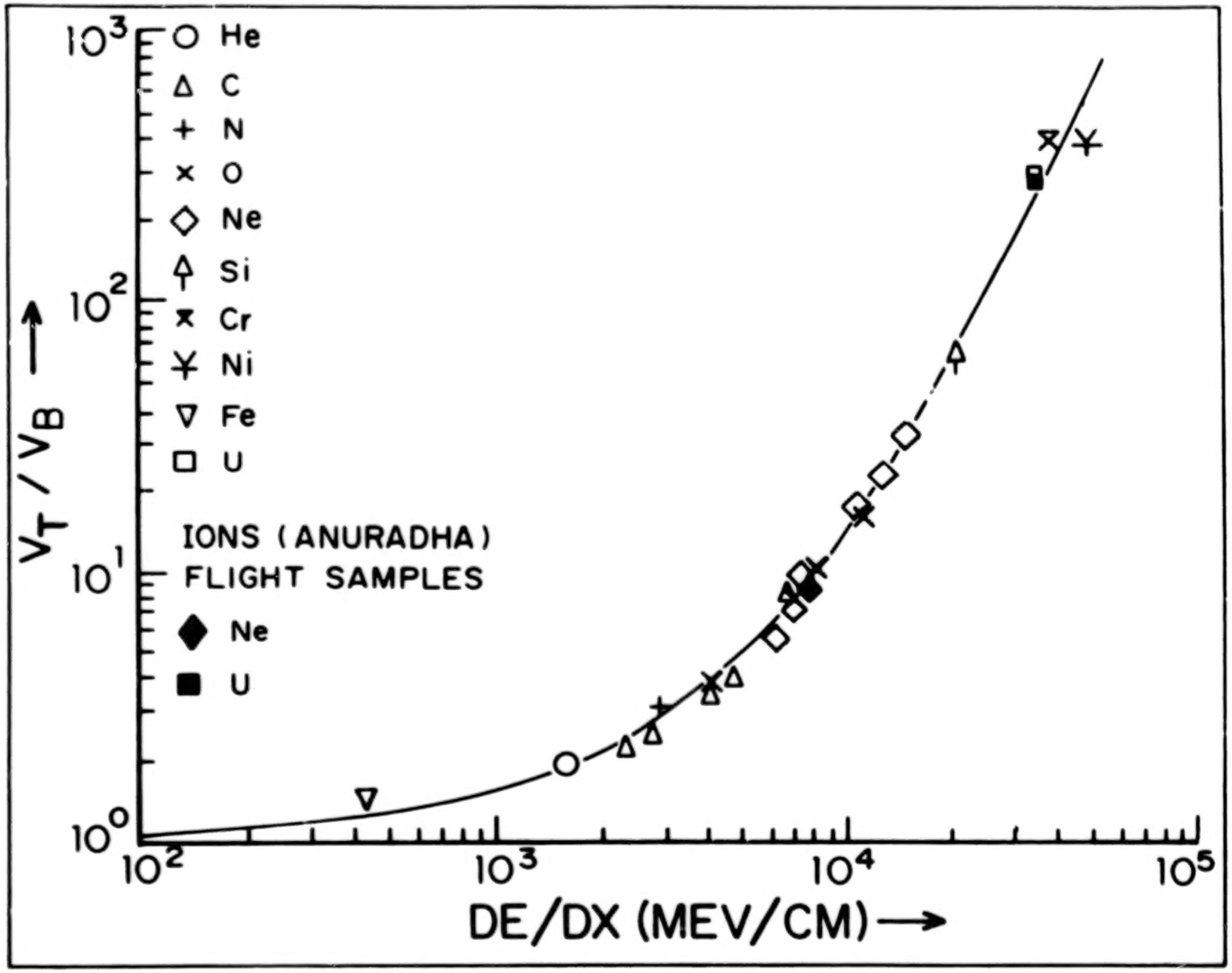

Figure 4. A plot of the ratio of the track etch rate, V_t, to the bulk etch rate, V_b, for the CR-39 plastic detector used in the IONS payload, as a function of energy loss (dE/dx) for various energetic ions. The alpha particle beam was obtained from the VEC, Calcutta (India), the ^{56}Fe and ^{238}U beams from Berkeley (USA) and the other ion beams from Dubna (USSR). Results from studies of neon and uranium ion tracks in the calibration samples were flown on Spacelab-3 (solid symbols) and they clearly indicate that the detector response remained the same during its exposure in space in the Spacelab-3 environment.

ORIGINAL PAGE IS
OF POOR QUALITY

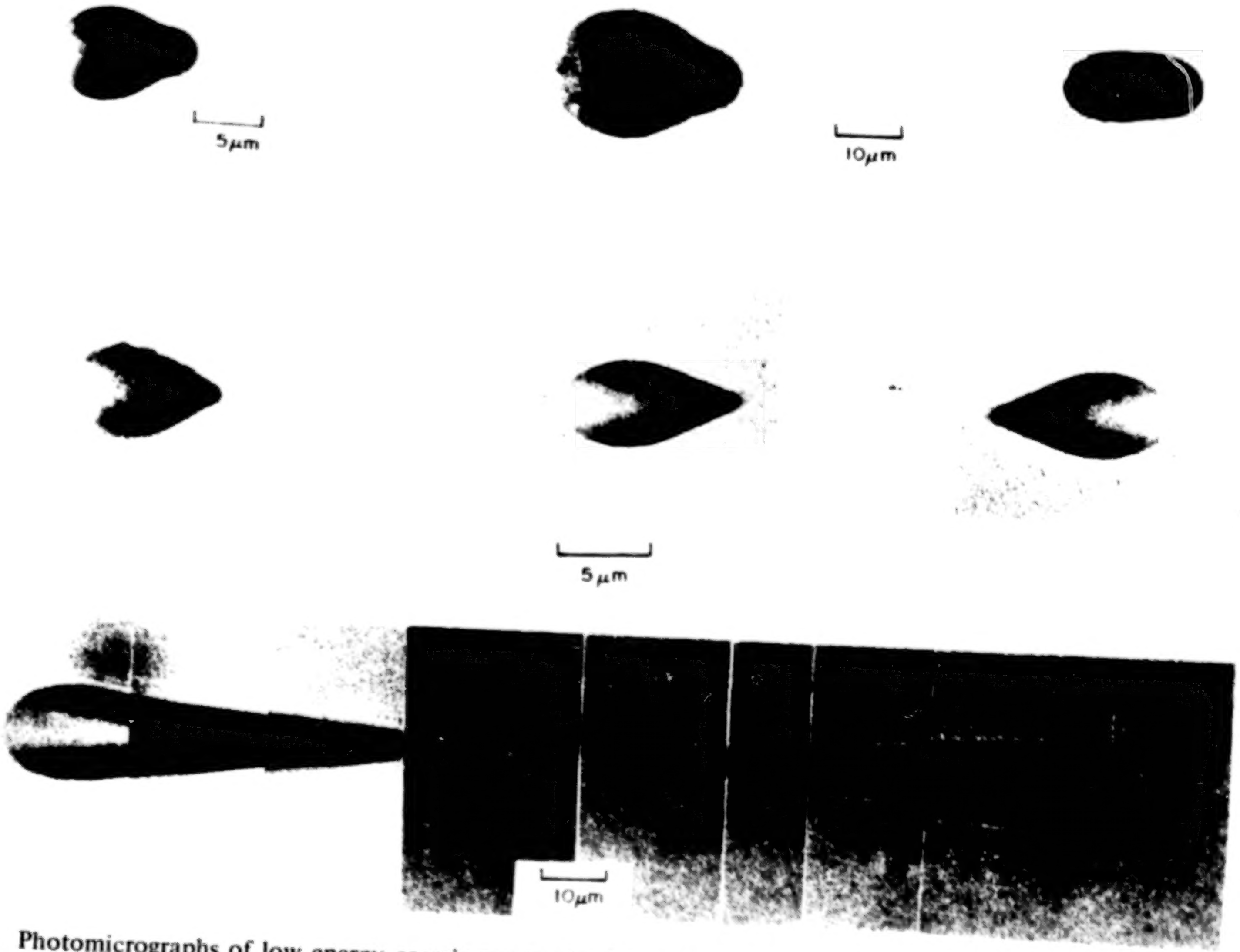

Figure 5. Photomicrographs of low energy cosmic ray tracks due to two stopping alpha particles (top) and a stopping oxygen group particle (from left to right, top row), oxygen group ions (middle), and a Fe ion (bottom) seen in auxiliary detector stack flown in IONS payload.

N87-22112

ANIMAL STUDIES ON SPACELAB-3

C. Schatte, R. Grindeland, P. Callahan, and W. Berry
NASA Ames Research Center, Moffett Field, California 94035

G. Funk and W. Lencki
MATSCO, Valley Forge, Pennsylvania

ABSTRACT

The flight of the two squirrel monkeys and 24 rats on Spacelab-3 was the first mission to provide "hands-on" maintenance of animals in a laboratory environment. With few exceptions, the animals grew and behaved normally, were free of chronic stress, and differed from ground controls only for gravity-dependent parameters. One of the monkeys exhibited symptoms of space sickness similar to those observed in humans, which suggests squirrel monkeys may be good models for studying the space-adaptation syndrome. Among the wide variety of parameters measured in the rats, most notable was the dramatic loss of muscle mass and increased fragility of long bones. Other interesting rat findings were those of suppressed interferom production by spleen cells, defective release of growth normone by somatrophs, possible dissociation of circadian pacemakers, changes in hepatic lipid and carbohydrate metabolism, and hypersensitivity of marrow cells to erythropoietin. These results portend a strong role for animals in identifying and elucidating the physiological and anatomical responses of mammals to microgravity.

INTRODUCTION

With the flight of two squirrel monkeys and 24 rats on Spacelab-3 (SL-3), NASA undertook the first of several missions using animals in a role for which they have long been used in research on Earth – as a model mammalian system with which to delineate the fundamental mechanisms of physiological response to an environment; i.e., microgravity. The primary objective of SL-3 was to evaluate the ability of the Research Animal Holding Facility (RAHF) to maintain animals in a normal, laboratory environment in space. It is important to use an animal that grows normally, behaves normally, and is free from chronic stress because most of the experimental measurements of interest in space are compromised by a subject which does not meet these requirements. Once these criteria are met, a high-quality experimental animal can then be provided for doing high-quality experiments on future missions. Beyond this primary objective, SL-3 did provide the opportunity to obtain preliminary data on animal health and well being in flight as well as to sample selected physiological parameters which might be the focus of future flight experiments.

FLIGHT OPERATIONS

The RAHF is a controlled-environment animal-housing facility, the physical specification and operation of which has been previously described [1]. The RAHF has two interchangeable modules of separate cages that can house up to four squirrel monkeys or 24 rats. Food and water consumption, activity, and intermittent photographic records are obtained automatically. Temperature, humidity, and light cycles can be controlled or varied as desired.

Two adult male squirrel monkeys, free of antibodies to Herpes saimiri, were flown unrestrained. The rats comprised two groups of 12 males each. One group was adults about 12 weeks old; these "large" rats represented the more mature, slower-growing organism. The other group was juveniles about 8 weeks old; these "small" rats represented the younger, faster-growing organism. Four of the large rats were implanted with a transmitter which permitted the continuous monitoring of heat rate and deep-body temperature. Both monkeys and rats were free of several specific pathogens, but were not gnotobiotic or axenic.

The flight animals spent 1 day in the Spacelab prior to launch and 7 days in microgravity and, because of an altered landing site, 6 hours in a jet flight during the return to Kennedy Space Center. Apart from a brief physical examination at 3 hours postflight, data collection could not begin until about 12 hours after landing. The squirrel monkeys were not tested postflight, whereas the rats were sacrificed for a thorough examination. Ground-control rats in cages similar to those in the RAHF (simulation controls) and ground controls in standard vivarium cages were also processed postflight. The ground-control groups could not be subjected to the postlanding jet flight, but were otherwise handled in exactly the same manner as were the flight rats.

RESULTS

Upon completion of the examination of the animals, the following results were recorded.

Squirrel Monkeys

Both squirrel monkeys ate less food, and were less active in space than on the ground (Table 1). Weight loss during the flight was within normal limits ($\leq$10 percent). The pattern of food intake indicated that, while one animal maintained relatively normal eating behavior throughout the mission, the other showed abnormally low food consumption for the first 4 days followed by substantial recovery during the last 3 days. Direct measurement of possible sickness episodes was not made. However, there was similarity between the responses of the two flight monkeys with those of monkeys centrifuged at 1.5 g [2]. In the latter case, the centrifuged animals showed frank evidence of sickness during the period of anorexia. Because the food-consumption pattern of one flight monkey was similar to that of centrifuged animals which were observed to be sick, we concluded that the one flight monkey probably experienced symptoms of space-adaptation syndrome during the early days of the flight while the other did not. Videotape records of behavior throughout the flight were consistent with this evaluation. Both monkeys were in good medical condition immediately postflight and no abnormal sequalae were noted thereafter.

Rats

More extensive studies were performed on the rats in the areas of growth, hematology, immunology, blood chemistry, heart rate, body temperature, muscle and bone growth, growth hormone, and liver metabolism. The following findings were recorded.

Growth

As shown in Table 2, the small flight rats grew at the same rate as their control counterparts that were similarly housed on the ground, whereas the larger flight rats grew at a lesser rate than controls. The flight-cage configuration reduced growth rate in both groups, as indicated by the higher body weights of vivarium control animals at the end of the mission. The weights of various organs (brain, heart, kidney, liver, adrenals, pituitary, spleen, prostate, thymus, parotid, and testes) in flight animals were either not different from simulation-cage control animals or within normal limitts of variation [3]. In particular, indications of chronic stress (adrenal hypertrophy, thymic involution, parotid hyperplasia, and liver atrophy) were not observed in eithr group (data not shown). We concluded that the flight animals grew at a normal rate and that growth-related symptoms of chronic stress were not evident.

Hematology, Immunology, and Blood Chemistry

Hematological indices (Table 3) showed increased hematocrit, red-cell count, and hemoglobin in both groups. Because plasma volume could not be measured, it is unclear whether these changes resulted from increased erythropoiesis or hemoconcentration. However, postflight studies with cultured bone-marrow cells showed that marrow sensitivity to erythropoietin was heightened in the flight animals (Table 4). Production of interferon-γ by spleen cells cultured postflight was dramatically reduced in flight animals (Table 4). Among several plasma-hormones and blood-cell parameters measured postflight, only plasma concentrations of osteocalcin were significantly lower in flight rats (Table 5). However, it is likely that measurement of these relatively labile parameters was compromised by the 12-hour hiatus between landing and sample acquisition. We believe that these measurements, more than the others, are less reflective of any changes which might have occurred during flight.

Heart Rate and Body Temperature

The composite 24-hr heart rate for four rats over the 7-day flight was compared to their heart rate for a similar preflight period. Heart rate was lower in flight at all times of the day, and in particular did not show the increase normally observed during the active period [9]. The period of the rhythm in flight was unchanged from that of preflight (23.9 ± 0.02 hours).

Mean body temperature was not affected by the flight, but the period of its rhythm was increased to 24.4 ± 0.3 hours. The finding suggests the possibility that microgravity might cause the body-temperature rhythm to become free-running. If so, it might then dissociate from that of heart rate, which did not show an indication of becoming free-running.

Muscle

Both large and small flight rats had reduced mass of selected hind-limb extensor and flexor muscles postflight (Table 6) when compared to similar control rats. The two groups differed in that the large control rats lost muscle mass from their preflight values, whereas most of the muscles in the small control animals showed some growth despite the obvious cage effect. In view of this, the muscle mass loss in flight was more pronounced for the small, faster-growing rats than for the more mature, slower-growing ones. The antigravity soleus muscle was the most sensitive to microgravity, with the less-gravity-dependent tibialis anterior the least.

Histochemical and morphological analyses [10] showed that loss of mass was apparently due to cell shrinkage rather than necrosis. However, about 1 percent of flight fibers were necrotic and up to 70 percent of solei fibers had core lesions. Diaminopeptidase activity was unchanged, but both tri-aminopeptidase and Ca-activated protease activity were substantially increased in flight muscles. A decrease in mitochondrial NADH dehydrogenase activity, a marker of aerobic metabolism, coupled with increased glycerophosphate dehydrogenase, a marker of glycolysis, suggested a shift from aerobic to glycolytic metabolism in flight muscles. Fast fiber types appeared more numerous in flight than in control solei and fast myofibrilliar ATPase activity was elevated in flight muscles.

Biochemical analyses of muscles (Table 7) from small animals showed that loss of protein, probably from myofibrils, corresponded to loss of muscle mass. Tyrosine content, an indicator of protein catabolism, was elevated only in small solei while the ratio of glutamine to glutamate, another such indicator was increased in most of the flight muscles. Glycogen deposition was observed in all flight muscles, suggesting a systemic effect apart from differences in muscle mass changes or metabolic changes specific to the individual muscles.

Bone

Growth of tibial plates from small rats was reduced in flight (Table 8) and the effect was consistent in all three zones of the plates. Using two injections of calcein as a marker, the rate of periosteal bone formation in the tibial diaphyses of large rats was 66 percent of preflight values for flight rats when compared to simulation cage control rats [14]. There were no differences between flight and control proximal humerus of large rats for the following parameters: percent trabecular bone volume, percent osteoclast surface, percent osteoblast surface, number of osteoblasts for osteoclasts per millimeter, and longitudinal bone growth [14]. There was a substantial increase in fragility based on biomechanical measurements (Table 9). This increased fragility occurred despite the fact that there were no differences in calcium, phosphorus, or hydroxyproline content of either trabecular or cortical bone [8, 15]. But in the absence of gross demineralization of long bones, gradient-density analysis showed that there was a shift in mineral concentration from lower specific-gravity fractions (1.3-1.7, 1.8-1.9) toward higher-density fractions (2.0-2.1, 2.2-2.9) in the flight bones [15]. Histochemical analyses of osteoblasts and osteoclasts showed no difference between flight and control animals for the following parameters: alkaline and acid phosphatases, golgi activity, secretory granule size, dipeptidal peptidase, and lysosomal activities [16].

Vertebral bone differed somewhat from long bones in that mass was decreased in the absence of demineralization (Table 10). Of particular interest was the fact that bone osteocalcin concentration was lower in flight animals. There was no difference between flight and control vertebrae of small or large rats for the following parameters: percent trabecular bone volume, percent osteoblast or osteoclast surface, osteoblasts or osteoclasts per millimeter of bone, and longitudinal bone growth.

Growth Hormone

Culture of pituitary somatotrophs [17] showed that the number of somatotrophs was increased and that their growth hormone content was higher in flight rats (Table 11). However, when growth hormones are implanted into hypophysectomized rats, release of hormone from flight cells was decreased as indicated by tibial growth. This apparent defect in the release of growth hormone thus caused total synthesis by somatotrophs from flight rats to be substantially lower than that in control rats. There was no difference in hormone species between flight and control animals. If growth hormone release was reduced during flight, it might have caused some of the changes in muscle and bone previously observed.

Liver Metabolism

Flight animals apparently had an increase in carbohydrate-based metabolism, suggested by the 20-fold increase in glycogen content, and a decrease in lipid-based metabolism, as suggested by the decreased cholesterol content (Table 12). The latter may have resulted from the decrease in activity of HMG-CoA reductase, which is the rate-limiting step in cholesterol synthesis. While sphingomyelin content was not different, the rate-limiting enzyme for sphingolipid synthesis, serine palmitoyl transferase, was lower in flight animals. The absence of any differences for the amino transferases suggests that the absence of whole-body catabolic activity and that protein catabolism which occurred in specific organs (e.g., muscle) was isolated to those organs. Tyrosine aminotransferase is particularly sensitive to circulating glycocorticoids. The lack of an increase in its activity is a further indication of mininal chronic stress in the flight animals.

Other Observations

Electron microscopic analysis of otoconia showed no degeneration of macular cells or demineralization of otoconial masses in flight rats [20]. Neurohistochemistry indicated no increase in cytochrome oxidase activity in the paraventricular nucleus, the site of control of fluid balance [21]. An extensive analysis of receptor binding in various parts of the brain (hippocampus, prefrontal cortex, lateral frontal cortex, posterior cortex, amygdala, pons-medulla, and cerebellum) showed only an increase in hippocampal binding for 5-hydroxytryptamine (5HT) [22]. However, membrane Mg-dependent NA-K ATPase activity was lower in flight rats.

There was no change in kidney receptor affinity for 1, 25-OH)$_2$ Vitamin D$_3$, suggesting that the kidney was not the site of control of any changes in calcium excretion [23]. Histomorphological analysis of cardiac muscle showed increased glycogen and lipid deposition in flight rats and loss of microtubules as compared to controls [24]. Histochemical and morphological analyses of parotid salivary gland showed no hyperplasia or major enzyme changes indicative of chronic discharge of the sympathetic nervous system [25].

CONCLUSIONS

The data presented in the previous sections indicate that the RAHF was able to maintain both rats and monkeys in a relatively normal condition suitable for their use as experimental animals. Growth parameters and several indices of chronic stress suggested that changes in bone and muscle were a result of exposure to microgravity per se and not an artifact resulting from adverse housing conditions. For the most part, changes in hematology, muscle, and bone were qualitatively similar to those reported in humans and in animals from the Kosmos flights of the Soviet Union. However, it is apparent that microgravity induces a wide range of physiological changes, some of which have not been measured heretofore. Further evaluation of these parameters will require more flight experiments, including collection of samples in flight to eliminate the complications resulting from delayed postflight sampling.

REFERENCES

1. Callahan, P. X., et al.,: Ames Research Center Life Sciences Payload Project for Spacelab Mission 3, SAE Technical Paper No. 831094, 1983.

2. Fuller, C. A.: Early Adaptation to Altered Gravitational Environments in the Squirrel Monkey. Physiologist, Vol. 28, No. 6, in press, 1985.

3. Grindeland, R. E., et al.: Rodent Body, Organ and Muscle Weight Responses to Seven Days of Microgravity. Physiologist, Vol. 28, No. 6, in press, 1985.

4. Lange, R. D., et al.: Hematologic Parameters of Astrorats Flown on SL-3. Physiologist, Vol. 28, No. 6, in press, 1985.

5. Gould, C. L., et al.: Effect of Flight in Mission SL-3 on Interferon-Gamma Production by Rats. Physiologist, Vol. 28, No. 6, in press, 1985.

6. Inge, W. H. and Hartle, D. K.: Atriopeptin (AP-3) in Atria and Plasma of Rats Orbited Aboard NASA Spacelab (SL-3) for Seven Days. Physiologist, Vol. 28, No. 6, in press, 1985.

7. Hartle, D. K. and Inge, W. H.: Plasma Renin Concentrations (PRC) of Rats Orbited for Seven Days Aboard NASA Spacelab 8. Physiologist, Vol. 28, No. 6, in press, 1985.

8. Patterson-Buckendahl, R. E., et al.: Osteocalcin as an Indicator of Bone Metabolism During Spaceflight. Physiologist, Vol. 28, No. 6, in press, 1985.

9. Fuller, C. A.: Homeostasis and Biological Rhythms in the Rat During Spaceflight. Physiologist, Vol. 28, No. 6, in press, 1985.

10. Riley, D. A., et al.: Morphological and Biochemical Changes in Soleus and Extensor Digitorum Longus Muscles of Rats Orbited in Spacelab 3. Physiologist, Vol. 28, No. 6, in press, 1985.

11. Tischler, M. E., et al.: Responses of Amino Acids in Hindlimb Muscles to Recovery from Hypogravity and Unloading by Tail-Cast Suspension. Physiologist, Vol. 28, No. 6, in press, 1985.

12. Henriksen, E. J., et al.: Muscle Protein and Glycogen Responses to Recovery from Hypogravity and Unloading by Tail-Cast Suspension. Physiologist, Vol. 28, No. 6, in press, 1985.

13. Duke, J., et al.: Microprobe Analysis of Epiphyseal Plates from Spacelab 3 Rats. Physiologist, Vol. 28, No. 6, in press, 1985.

14. Wronski, T. J., et al.: Histomorphometric Analysis of the Rat Skeleton. Physiologist, Vol. 28, No. 6, in press, 1985.

15. Russell, J. E. and Simmons, D. J.: Bone Maturation in Rats Flown on the Spacelab 3 Mission. Physiologist, Vol. 28, No. 6, in press, 1985.

16. Doty, S. B.: Morphologic and Histochemical Studies of Bone Cells from SL-3 Rats. Physiologist, Vol. 28, No. 6, in press, 1985.

17. Hymer, W. C., et al.: Microgravity Associated Changes in Pituitary Growth Hormone (GH) Cells Prepared from Rats Flown on Spacelab 3. Physiologist, Vol. 28, No. 6, in press, 1985.

18. Hargrove, J. L. and Jones, D. P.: Hepatic Enzyme Adaptation in Rats After Spaceflight. Physiologist, Vol. 28, No. 6, in press, 1985.

19. Merrill, A. H., et al.: Hepatic Enzymes of Sphingolipid and Glycerolipid Biosynthesis in Rats from Spacelab 3. Physiologist, Vol. 28, No. 6, in press, 1985.

20. Ross, M. D., et al.: Otoconial Morphology in Space-Flown Rats. Physiologist, Vol. 28, No. 6, in press, 1985.

21. Murakami, D. M., et al.: Changes in Functional Metabolism in the Rat Central Nervous System Following Spaceflight. Physiologist, Vol. 28, No. 6, in press, 1985.

22. Miller, J. D., et al.: Effects of Weightlessness in Neurotransmitter Receptors in Selected Brain Areas. Physiologist, Vol. 28, No. 6, in press, 1985.

23. Manglesdorf, D. J., et al.: 1,25-dihydroxy-vitamin D_3 Receptors in Space-Flown Versus Grounded Control Rat Kidneys. Physiologist, Vol. 28, No. 6, in press, 1985.

24. Philpott, D. E., et al.: Microgravity Changes in Heart Structure and Cyclic-AMP Metabolism. Physiologist, Vol. 28, No. 6, in press, 1985.

25. Mednieks, M. I. and Hand, A. R.: Biochemical and Morphological Evaluation of the Effects of Spaceflight on Rat Salivary Glands. Physiologist, Vol. 28, No. 6, in press, 1985.

Table 1. Food consumption and weight change of squirrel monkeys.

	WEIGHT (G)	% WT. LOSS	FOOD CONSUMPTION (% PRE-FLIGHT)	ACTIVITY (% PRE-FLIGHT)
M1	442	5	67	44
M2	442	4	20	11

Table 2. Weight change of rats (Ref. 3).

	RATS	
	"SMALL"	"LARGE"
PREFLIGHT	200.1 ± 1.5^a	362.3 ± 6.5
FLIGHT	242.9 ± 3.1	383.9 ± 4.6^b
CONTROL (SIMULATION CAGE)	258.2 ± 4.1	400.8 ± 7.8
CONTROL (VIVARIUM CAGE)	301.8 ± 5.0^b	433.0 ± 5.0^b

[a] X̄ ± S.E.M., N = 12

[b] DIFFERENT FROM CONTROL (SIMULATION CAGE), P < .05 OR LESS

Table 3. Hematology of rats (Ref. 4).

	CONTROL	FLIGHT
HEMATOCRIT, %	40.7 ± 1.50^a	45.6 ± 1.90^b
RBC, 10^{12}/L	5.85 ± .28	6.66 ± .40^b
HB, G/DL	13.5 ± .5	14.7 ± .60^b
MCV, FL	69.70 ± 2.20	67.80 ± 3.50
MCH, PG	23.10 ± 1.02	22.8 ± 1.22
MCHC, G/DL	33.10 ± .95	33.6 ± 1.51
WBC, 10^9/L	7.89 ± 2.0	7.88 ± 1.8
DIFFERENTIAL, %		
LYMPHOCYTES	89.5 ± 2.0	77.8 ± 8.4^b
MONOCYTES	1.2 ± 0.9	1.6 ± 1.1
EOSINOPHILS	0.9 ± 0.7	0.9 ± 1.0
NEUTROPHILS	8.2 ± 4.3	19.7 ± 7.9^b

NO DIFFERENCE FOR SPLEEN CELL OR BONE MARROW DIFFERENTIAL COUNTS

[a] X̄ ± S.E.M., N = 12

[b] P < .001

Table 4. Interferon-gamma production by cultured spleen cells (Ref. 5) and sensitivity of bone-marrow cultures to erythropoietin (Ref. 4) in rats.

	CONTROL	FLIGHT
NO. SPLEENS PRODUCING INTERFERON-γ / NO. SAMPLES	7/11	1/10^a
BONE ERYTHROID COLONIES/10^5 CELLS		
DAY 5, .02 U EP/ML	2.67 ± 2.19^b	22.7 ± 2.54^c
1.0 U EP/ML	7.67 ± 2.06	52.8 ± 7.52^c
DAY 6, .02 U EP/ML	.483 ± .510	4.26 ± 1.68^c
1.0 U EP/ML	1.83 ± .45	8.67 ± 3.04^c

[a] NEARLY UNDETECTABLE PRODUCTION OF INTERFERON

[b] X̄ ± S.E.M., N = 6

[c] P < .001 OR LESS

Table 5. Plasma measurements in rats (Ref. 3, 4, and 6-8).

	N	SIM CONTROL	FLIGHT
CALCIUM, MG/DL	12	9.98 ± .64^a	9.00 ± .26
PHOSPHORUS, MG/DL	12	10.4 ± .44	10.1 ± .26
CREATININE, MG/DL	12	1.12 ± .16	1.02 ± .04
ALKALINE PHOSPHATASE, IU/L	12	198 ± 12	212 ± 19
OSTEOCALCIN, NG/ML	6	347 ± 12	271 ± 29^b
1, 25- DIHYDROXY VIT. D3, PG/ML	6	64 ± 6.2	94 ± 17
CORTICOSTERONE, UG/DL	6	17.0 ± 5.0	17.7 ± 4.4
THYROXIN, UG/DL	12	4.4 ± 0.9	4.1 ± 1.0
TRIIODOTHYRONINE, NG/DL	12	79.1 ± 8.8	72.6 ± 6.1
GROWTH HORMONE, NG/ML	12	7.5 ± 2.9	7.2 ± 5.1
PROLACTIN, NG/ML	12	2.8 ± 0.9	5.5 ± 6.1
ERYTHROPOIETIN, MU/ML	6	19.0 ± 3.7	16.5 ± 4.6
ATRIOPEPTIN, NG/ML	6	2.80 ± .48	2.00 ± .67
RENIN, NG/ML	6	44.2 ± 7.3	35.6 ± 6.6

[a] X̄ ± S.E.M.

[b] P< .01 OR LESS

Table 6. Muscle weights (G/100 G body weight) of rats expressed as percentage of preflight values (Ref. 3).

	CONTROL	FLIGHT
SMALL		
SOLEUS	0.0^a	-32.5^b
GASTROCNEMIUS	+7.9	-4.7
PLANTARIS	+8.7	-10.6^b
TIBIALIS ANTERIOR	+1.0	-4.6
EXTENSOR DIGITORUM LONGUS	+4.5	-6.8^b
ADDUCTOR LONGUS	-4.3	-6.0^b
LARGE		
SOLEUS	2.2	-20.0^b
GASTROCNEMIUS	-4.4	-13.9^b
PLANTARIS	-6.0	-12.0^b
TIBIALIS ANTERIOR	-6.0	-11.0
EXTENSOR DIGITORUM LONGUS	-4.2	-10.6^b
ADDUCTOR LONGUS^c	-15.3	-15.3

[a] MEAN WEIGHT/100 G BODY WEIGHT EXPRESSED AS PERCENTAGE CHANGE FROM PREFLIGHT. N=12

[b] P < .05 OR LESS

[c] PREFLIGHT VALUES UNUSUALLY HIGH

ORIGINAL PAGE IS
OF POOR QUALITY

Table 7. Biochemical measurements in muscles of small rats expressed as percentage of control (Refs. 11 and 12).

	SOLEUS	GASTROC.	PLANTARIS	EX. DIG. LONGUS	TIBIALIS ANTERIOR
PROTEIN	- 54ᵃ	- 18	- 17	- 17	- 6
GLYCOGEN	+144	+ 89	+ 61	+ 63	+ 53
TYROSINE	+ 57	NSᵇ	NS	NS	NS
GLUTAMINE	- 26	- 20	- 24	- 21	NS
GLUTAMATE	- 56	- 46	- 42	- 28	- 42
RATIO GLN/GLU	+ 79	+ 48	+ 29	NS	+ 39
ASPARTATE & ASPARAGINE	- 77	NS	- 11	NS	NS
MALATE	- 60	54	NS	NS	NS
ALANINE	- 21	NS	NS	NS	NS

ᵃ NUMERICAL VALUES SIGNIFICANT AT P < .05 OR LESS

ᵇ NOT SIGNIFICANT

Table 8. Height in millimeters of tibial-growth plates of small rats (magnification in parentheses) (Ref. 13).

	TOTAL (X111)	RESTING (X200)	PROLIFERATIVE (X200)	HYPERTROPHIC/CALCIFYING (X200)
CONTROL	99.15ᵃ	10.08	36.76	53.19
	± 1.50	± .67	± .82	± 1.22
FLIGHT	56.59ᵇ	4.04ᵇ	25.42ᵇ	25.82ᵇ
	± 1.55	± .60	± .78	± 1.47

ᵃ x̄ ± S.E.M., N = 5

ᵇ P < .001 OR LESS

Table 9. Biomechanical measurements on humeri of small rats (Ref. 8).

	LIM CONTROL	FLIGHT
ULTIMATE LOAD, NEWTONS	41.5 ± 1.94ᵃ	28.8 ± 1.76ᵇ
ULTIMATE DEFORMATION, MM	.677 ± .017	.575 ± .039
WORK TO ULTIMATE LOAD, N/MM	16.1 ± .81	8.86 ± 1.18ᵇ
INITIAL STIFFNESS, N/MM	95.4 ± 3.57	70.5 ± 4.08ᵇ

ᵃ x̄ ± S.E.M., N = 5

ᵇ FLIGHT DIFFERENT FROM CONTROL AT P < .001 OR LESS

Table 10. Analyses on vertebra L3 of small rats (Ref. 8).

	CONTROL	FLIGHT
DRY WEIGHT, MG/G BODY WEIGHT	.954 ± .009ᵃ	.518 ± .026ᵇ
CALCIUM, UG/MG BONE	180 ± 13	179 ± 3.7
OSTEOCALCIN, UG/MG BONE	2.49 ± .11	2.19 ± .22ᵇ

ᵃ x̄ ± S.E.M., N = 5

ᵇ P < .01

Table 11. Analyses of cultured pituitary somatotrophs (Ref. 17).

	CONTROL	FLIGHT
SMALL		
% SOMATOTROPHS/PITUITARY	42.5	44.0
% PRL CELLS/PITUITARY	35.5	31.8
NG STH/10^3 SOMATOTROPHS	21.6	33.3ᵇ
NG STH RELEASED/10^3 SOMATOTROPHS	108.6	60.7ᵇ
NET SYNTHESIS/6 DAYS, NG/STH/10^3 SOMATOTROPHS	90.0	55.3ᵇ
LARGE		
% SOMATOTROPHS/PITUITARY	56.7	43.7ᵇ
% PRL CELLS/PITUITARY	37.6	33.4
NG STH/10^3 SOMATOTROPHS	56.9	67.1ᵇ
NG STH RELEASED/10^3 SOMATOTROPHS	128.4	94.5ᵇ
NET SYNTHESIS/6 DAYS, NG/10^3 SOMATOTROPHS	94.6	41.9ᵇ

ᵃ x̄ ONLY, N = 8

ᵇ P < .05 OR LESS

Table 12. Biochemical analyses of liver from small rats (Refs. 18 and 19).

	CONTROL	FLIGHT
LIVER WEIGHT, G	11.1 ± 0.8ᵃ	9.9 ± 0.5
MICROSOMAL PROTEIN, MG/G LIVER	5.6 ± 0.9	4.2 ± 0.5ᵇ
GLYCOGEN, MG/G LIVER	1.24 ± .08	24.5 ± 3.4ᵇ
CHOLESTEROL, UMOL/G LIVER	4.1 ± 1.0	6.9 ± 0.4ᵇ
PHOSPHOLIPIDS, UMOL/G LIVER	35.8 ± 1.5	32.9 ± 1.7
SPHINGOLIPIDS, UMOL/G LIVER	2.6 ± 0.2	2.3 ± 0.2
P450, NMOL/MG PROTEIN	3.30 ± 1.23	1.71 ± 0.35ᵇ
B5	0.71 ± .10	0.62 ± .12
ENZYMES		
LIPASE, NMOL/MIN/MG PROTEIN	56.9 ± 2.4	54.5 ± 4.00
SERINE PALMITOYL TRANSFERASE, PMOL/MIN/MG PROTEIN	29.0 ± 2.7	17.4 ± 2.1ᵇ
GLYCEROL 3-PHOSPHATE ACYLTRANSFERASE, NMOL/MIN/MG PROTEIN	1.36 ± .14	1.00 ± .24
HMG [illegible] DUCTASE, PMOL/MIN/MG PROTEIN	8.6 ± 1.3	1.7 ± 0.3ᵇ
TYROSINE AMINO TRANSFERASE, UMOL/MIN/MG PROTEIN	.021 ± .007	.026 ± .005
ASPARTATE AMINOTRANSFERASE, UMOL/MIN/MG PROTEIN	1.50 ± .26	1.44 ± .19
GLUTATHIONE-S-TRANSFERASE, UMOL/MIN/MG PROTEIN	11.5 ± 0.8	11.1 ± 2.8

ᵃ x̄ ± S.E.M., N = 5

ᵇ P < .05 OR LESS

ORIGINAL PAGE IS OF POOR QUALITY

N87-22113

AUTOGENIC-FEEDBACK TRAINING: A PREVENTIVE METHOD FOR SPACE ADAPTATION SYNDROME

Patricia S. Cowings and Joseph C. Sharp
NASA Ames Research Center

William B. Toscano and Joe Kamiya
University of California at San Francisco

Neal E. Mill
Yale University

This is a report on the progress made to date on the reduction of data for Spacelab 3 Shuttle experiment, No. 3AFT23. Four astronauts participated as subjects in this experiment. Crewmen A and B served as treatment subjects (i.e., received preflight training for control of their own motion sickness symptoms) and Crewmen C and D served as controls (i.e., did not receive training). A preliminary evaluation of Autogenic Feedback Training (AFT) was made from visual inspections of graphs that were generated from the preflight and inflight physiological data which included:

a) Baseline rotating chair tests for all crewmen.

b) Posttraining rotating chair tests of treatment groups subjects.

c) Preflight data from Joint Integrated Simulations for all crewmen.

d) Flight data for all crewmen during mission days 0 through 4, and mission day 6 for treatment subjects only.

Skin temperature and acceleration data collected during the JIS and the SL-3 mission have not yet been reduced and will be included in a later report.

A summary of the findings suggested by these data is outlined below: The preflight training schedule given to treatment group subjects was, on average, 90 days longer than planned because of delays in the launch date. This change in the schedule and its effect on training performance was discussed in two earlier reports (SL-3 Flight Readiness Review, dated April 25, 1985 and the SL-3 30-day Report, dated June 12, 1985). The investigators have concluded that the generally poorer performance of crewmembers in this study was primarily due to the change in the schedule, although motivation may have been a secondary factor. The data of crewmen A and B was compared to the data of 40 test subjects who were given AFT using a more optimal schedule in the laboratory. The increase in the number of rotations tolerated from the pre- to post-training rotating chair tests was computed for all subjects and their scores were ranked from the largest to smallest increase. Crewman A shows an increase of 398 rotations and his score among the sample of 42 subjects was about average, at the 54th percentile. Crewman B, however, showed much less improvement in motion sickness tolerance after training, with an increase of only 102 rotations. His score among the larger sample of subjects was at the 18th percentile.

Each crewman's initial susceptibility to motion sickness (i.e., number of rotations tolerated before reaching severe malaise), was recorded during their baseline rotating chair test. The physiological responses of treatment subjects which changed the most during motion sickness stimulation from their resting baseline levels were selected as training measures for subsequent AFT sessions.

Both Crewmen A and B were each given 12 preflight AFT sessions without rotation in which they were taught to increase and decrease, on alternate trials, their heart rte (HR), skin conductance (SC), and finger pulse volume (FPV) with the aid of visual and auditory feedback (Fig. 1). These subjects were also instructed to use the feedback from the three different responses to change a pattern (i.e., HR and SC up, FPV down or HR and SC down, FPV up) without changing respiration rate or muscle activity. An example of physiological data from one training session is included in this report.

The physiological data of Crewman A collected during his pretraining rotating chair test was compared to the data from his posttraining rotating chair test (Fig. 2). A visual inspection of the data for this subject showed a reductio in sympathetic tone (i.e., decreased stress) for all three physiological responses in his posttraining test. Further, while this crewman maintained lower physiological levels, he was able to tolerate much higher rotational velocities than during his pretraining test. When the pre- and post-training rotating chair tests of Crewman B were compared there was some reduction in heart rate, while skin conductance and finger pulse volume showed more of a stress response, and only a moderate increase in motion sickness tolerance was observed after training.

On the basis of their preflight training and motion sickness test data, the investigators predicted (documented in the SL-3 Flight Readiness Review, dated April 25, 1985) that Crewman A (Fig. 3) would have a higher probability of success at preventing or controlling his symptoms in space than Crewman B (Fig. 4).

The inflight symptom reports revealed that crewman A did not experience any severe symptom episodes during the mission, while Crewman B reported one severe symptom episode. Both control group subjects, C and D (who took anti-motion sickness medication), reported multiple symptom episodes on mission day 0. When the inflight physiological data of Crewman A was compared to that of the other crewmen participating in this study, he showed reduced sympathetic tone for all physiological variables measured (Fig. 5).

The following recommendations were made by the investigators for future flights: First, use a more optimal preflight training schedule for treatment subjects that would begin at 10 months to one year prior to launch with "follow-up" AFT sessions at launch-3 months. Second, reduce inflight requirements for physiological monitoring to the first three mission days only. Third, modify flight hardware to facilitate crew mobility and comfort.

The preliminary results from this Spacelab-3 experiment are encouraging. The measurements and inflight procedures used should eventually enable the investigators to evaluate the efficacy of AFT as a countermeasure for SAS, and to objectively document human psychophysiological responses to the microgravity environment. However, it is clear that additional data must be obtained inflight (i.e., 8 treatment group subjects and 8 controls) before these goals can be achieved.

Acknowledgment. The science team expresses their appreciation to Mr. Jen-Lin Chen, University of California, San Francisco, for his programming support for data reduction and graphics.

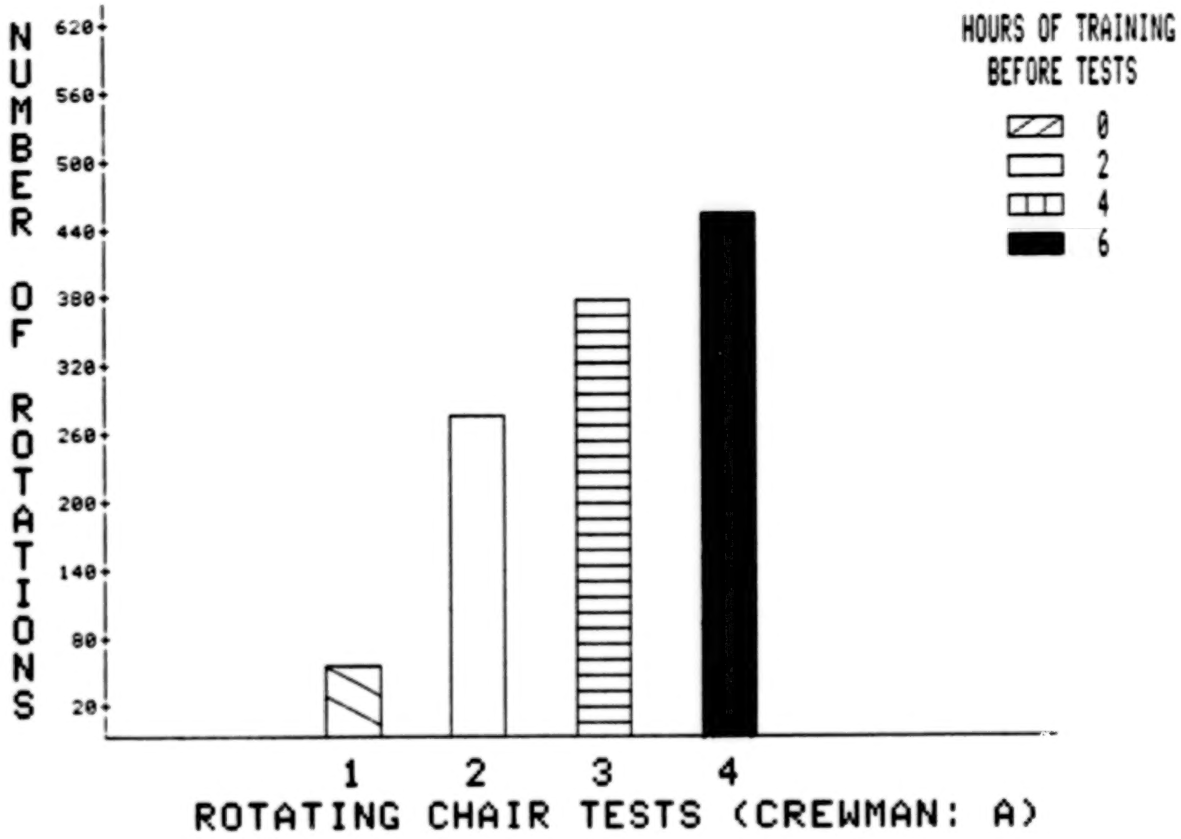

Figure 1. Motion sickness tolerance before, during, and after training.

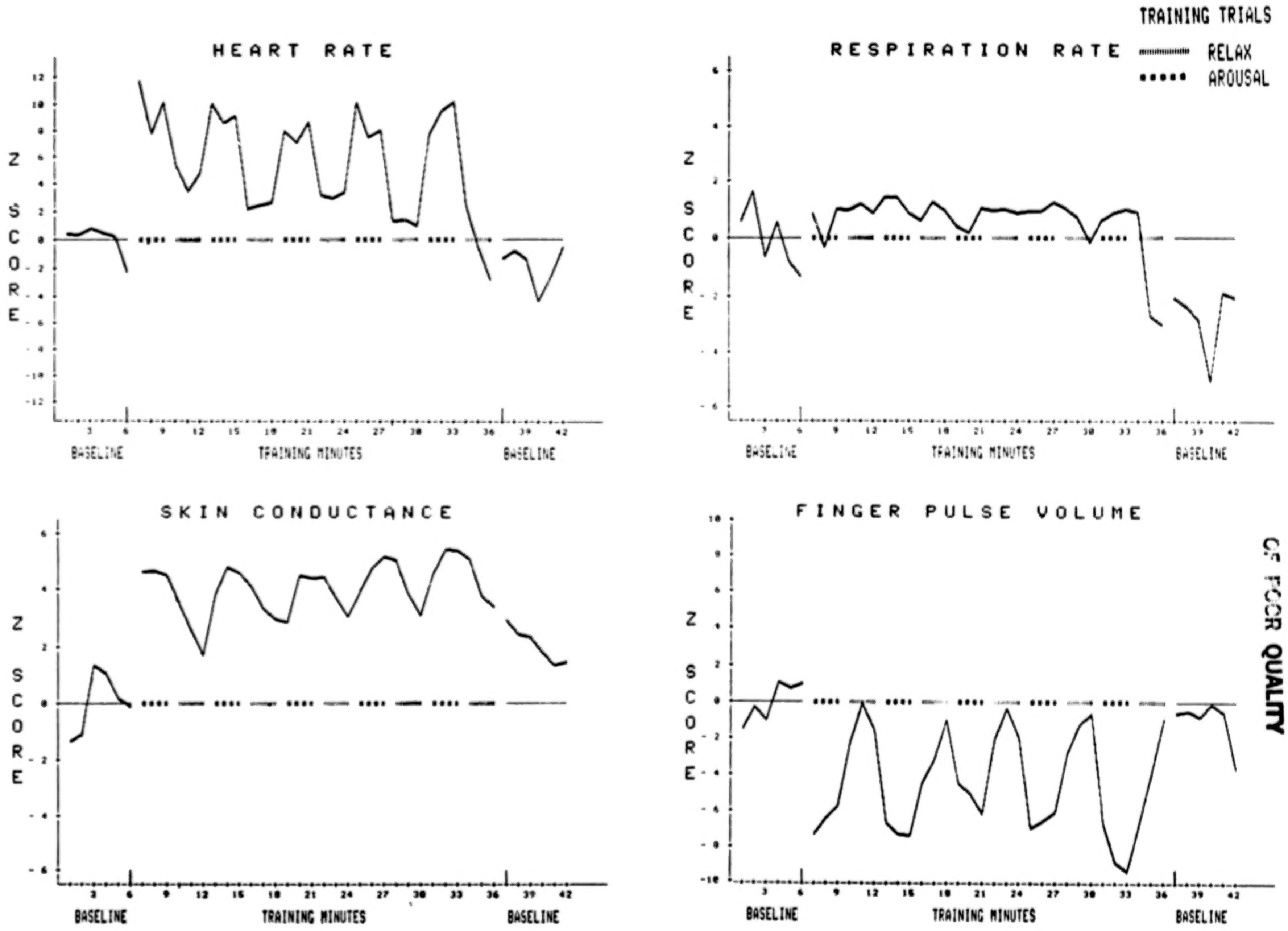

Figure 2. Sample AFT session.

ORIGINAL PAGE IS
OF POOR QUALITY

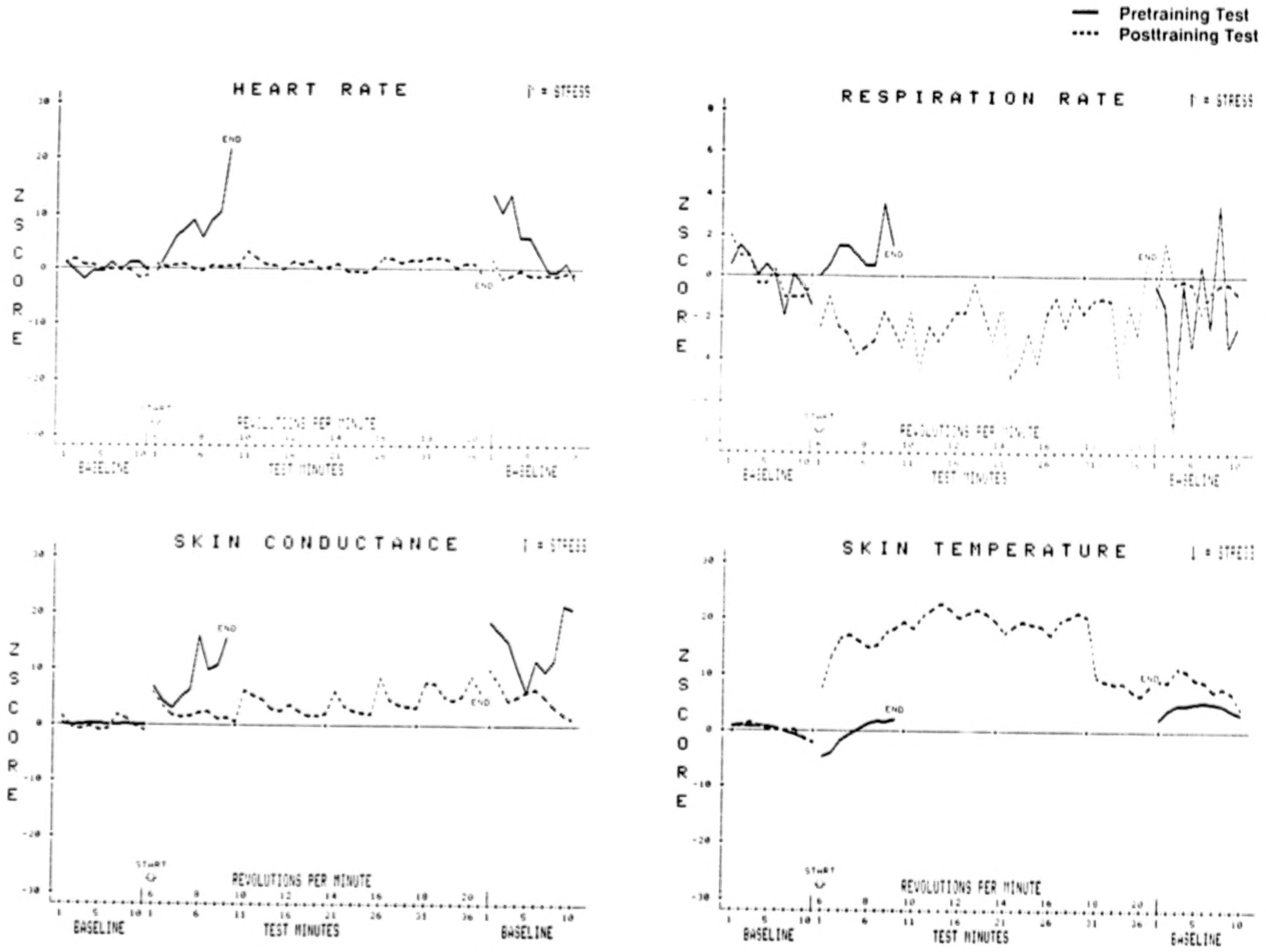

Figure 3. Physiological data during rotating chair tests, Crewman A.

ORIGINAL PAGE IS
OF POOR QUALITY

ORIGINAL PAGE IS
OF POOR QUALITY

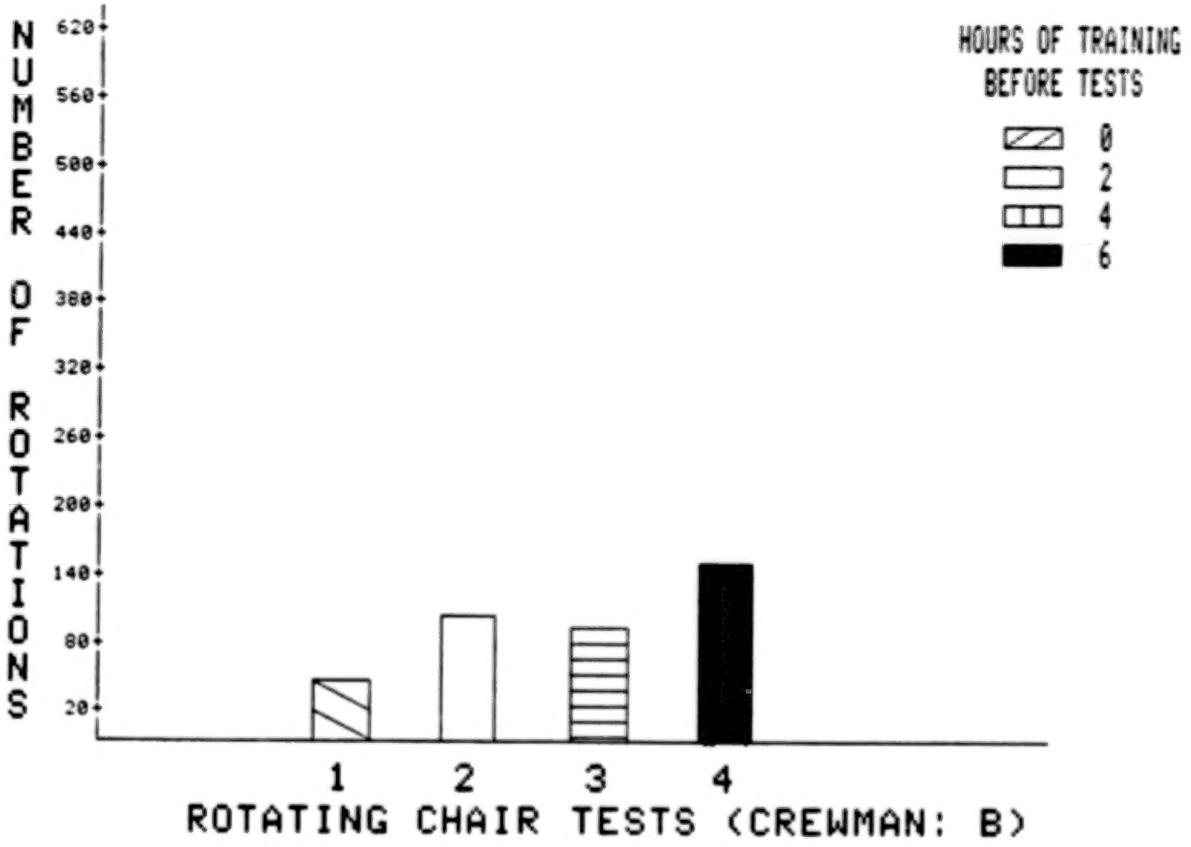

Figure 4. Motion sickness tolerance before, during, and after training.

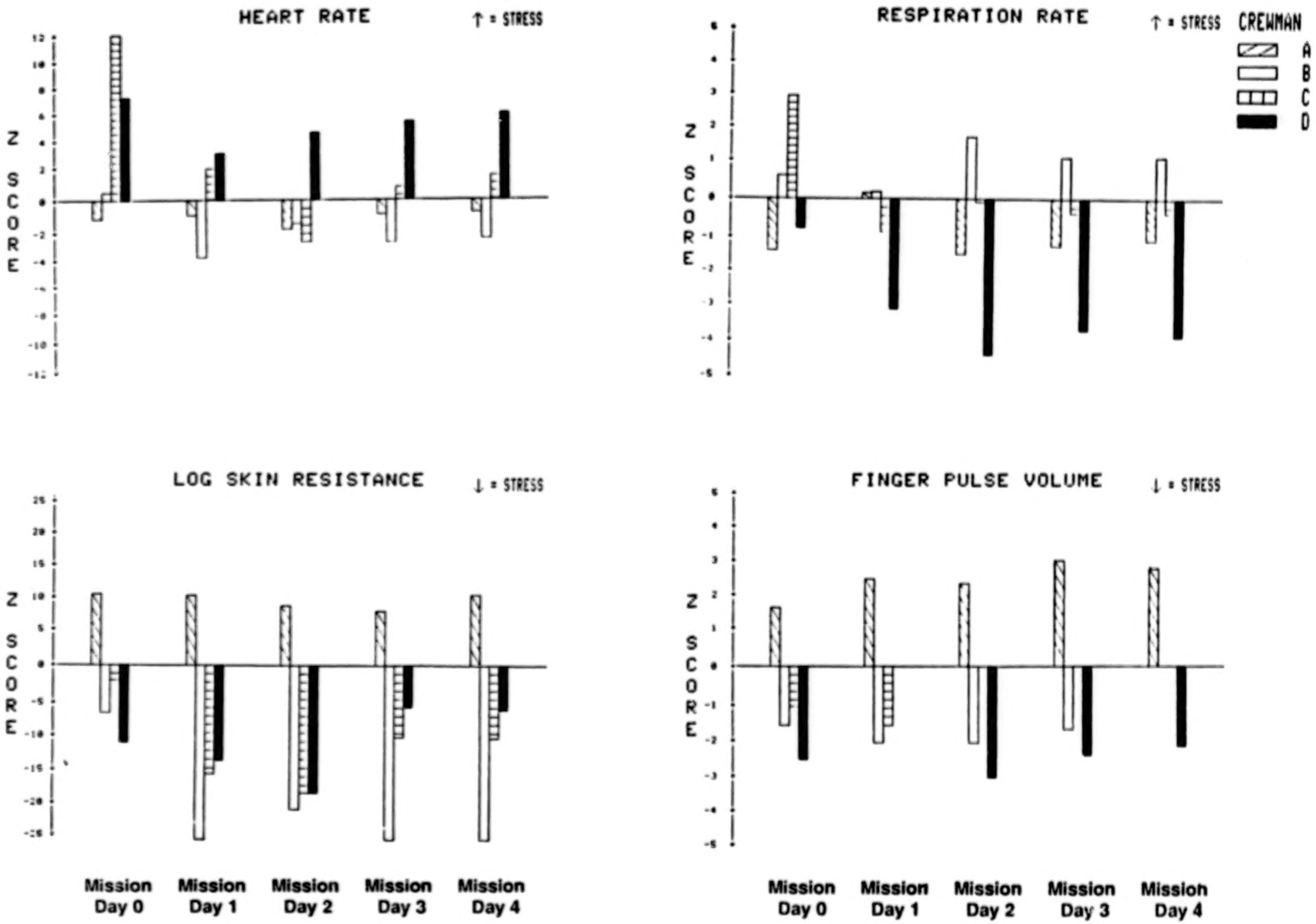

Figure 5. Daily Zscore averages of physiological data inflight.

ORIGINAL PAGE IS
OF POOR QUALITY

SL-3 URINE MONITORING INVESTIGATION

Howard J. Schneider and Carolyn S. Leach
Medical Sciences Division, NASA JSC, Houston, TX 77058

L. Daniel Inners
Technology Inc., 17625 El Camino Real, Houston, TX 77058

The purpose of the SL-3 Urine Monitoring Investigation was twofold: to conduct an inflight function test of the Urine Monitoring System (UMS), and to add information to our existing urinary electrolyte/endocrine data base.

The Urine Monitoring System is part of the Life Sciences Laboratory Equipment inventory. It was designed to be compatible with existing spacecraft systems and to provide life sciences investigators with a convenient means for estimating single-void urine volumes while collecting urine samples in an easily stowed, secure container.

In addition to an evaluation of the instrument from the operational standpoint, the inflight functional testing of the UMS consisted of the following specific tests related to precision and accuracy of measurement:

(1) Calibration with known masses of water injected into the instrument.

(2) Determination of residual volume, i.e., the amount of fluid (primarily flush water) left in the instrument at the end of a cycle.

Twenty-four usable data points were obtained from the inflight calibration protocol. These points were used to establish a calibration curve which could be used to convert UMS readout to mass for an unknown quantity of fluid introduced into the device. The confidence limits on the masses estimated by this procedure of inverse prediction can be established by standard statistical methods. The 50 percent confidence interval averages about +2 percent of the estimated mass. The mean residual volume estimated from eight determinations was 25.9 ml, with a standard error of 1.8 ml.

With regard to the second objective, we wished to take advantage of the capabilities of the UMS to collect samples and volume data throughout the mission, including the preflight and postflight periods, and particularly during the first 12 hours following launch. Inflight operational difficulties, due primarily to insufficient air flow through the UMS, precluded our meeting this objective.

Samples were collected on a void-by-void basis for three days preflight and for four days postflight, however, inflight samples were limited to a single crewmember and primarily to a 25-hour period spanning MET Days 4 and 5. All samples were subjected to analysis. Biochemical and endocrine measurements included creatinine content, sodium, potassium, and chloride ion concentrations, osmolality, and levels of aldosterone and cortisol. Except for probable dilution of samples because of the residual volume mentioned above, there was no indication in any of these measurements that samples collected with the UMS would not provide valid physiological data.

1. REPORT NO. NASA CP-2429	2. GOVERNMENT ACCESSION NO.	3. RECIPIENT'S CATALOG NO.
4. TITLE AND SUBTITLE Spacelab 3 Mission Science Review		5. REPORT DATE February 1987
		6. PERFORMING ORGANIZATION CODE
7. AUTHOR(S) Edited by George H. Fichtl, John S. Theon, Charles K. Hill, and Otha H. Vaughan		8. PERFORMING ORGANIZATION REPORT #
9. PERFORMING ORGANIZATION NAME AND ADDRESS George C. Marshall Space Flight Center Marshall Space Flight Center, Alabama 35812		10. WORK UNIT NO. M-547
		11. CONTRACT OR GRANT NO.
		13. TYPE OF REPORT & PERIOD COVERED Conference Publication
12. SPONSORING AGENCY NAME AND ADDRESS National Aeronautics and Space Administration Washington, D.C. 20546		14. SPONSORING AGENCY CODE

15. SUPPLEMENTARY NOTES

George H. Fichtl, Charles K. Hill, and Otha H. Vaughan: George C. Marshall Space Flight Center, Marshall Space Flight Center, Alabama.

John S. Theon: National Aeronautics and Space Administration, Washington, D.C.

16. ABSTRACT

A symposium on Spacelab 3 mission preliminary scientific results was held at the Marshall Space Flight Center on December 4, 1985. This document provides papers and abstracts of the presentations made at the symposium and constitutes the scientific report for the Spacelab 3 mission. Spacelab 3, the second flight of the National Aeronautics and Space Administration's (NASA) orbital laboratory, signified a new era of research in space. The primary objective of the mission was to conduct applications, science, and technology experiments requiring the low-gravity environment of Earth orbit and stable vehicle attitude over an extended period (e.g. 6 days) with emphasis on materials processing. The mission was launched on April 29, 1985, aboard the Space Shuttle Challenger which landed a week later on May 6. The multidisciplinary payload included 15 investigations in five scientific fields: materials science, fluid dynamics, life sciences, astrophysics, and atmospheric science.

17. KEY WORDS Spacelab 3, Science Results, Experiments, Challenger, Astrophysics, Fluid Dynamics, Life Sciences, Atmospheric Science, Astrophysics, Materials Science	18. DISTRIBUTION STATEMENT Subject Category: 34 Unclassified/Unlimited

19. SECURITY CLASSIF. (of this report) Unclassified	20. SECURITY CLASSIF. (of this page) Unclassified	21. NO. OF PAGES 94	22. PRICE A05

For sale by National Technical Information Service, Springfield, Virginia 22161

NASA-Langley, 1987